

# MedVersa: A Generalist Foundation Model for Medical Image Interpretation

Hong-Yu Zhou PhD<sup>★</sup>, Julián Nicolás Acosta MD<sup>\*,★</sup>, Subathra Adithan MD<sup>\*,†</sup>, Suvrankar Datta MD<sup>‡</sup>, Eric J. Topol MD<sup>△</sup> and Pranav Rajpurkar PhD<sup>★</sup>

<sup>\*</sup>Equal contributions, <sup>★</sup>Department of Biomedical Informatics, Harvard Medical School, Boston, USA, <sup>†</sup>Jawaharlal Institute of Postgraduate Medical Education and Research, Puducherry, IN, <sup>‡</sup>Department of Radiodiagnosis and Interventional Radiology, All India Institute of Medical Sciences (AIIMS), New Delhi, IN, <sup>△</sup>Scripps Research Translational Institute, Scripps Research, La Jolla, CA, USA.

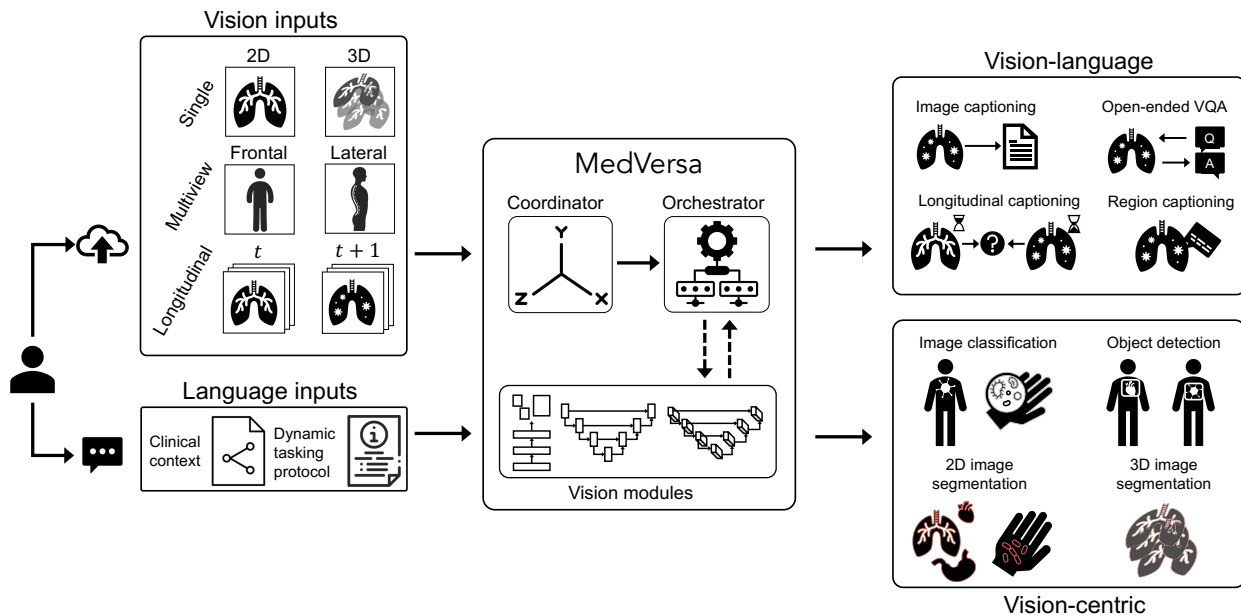


Figure 1 | **MedVersa** is capable of performing both vision-language and vision-centric medical imaging tasks. It can accept a wide range of inputs, including images of various types (e.g., multimodal, multiview, or longitudinal) and language requests (clinical context and dynamic tasking protocol). The model’s optimizable orchestrator, powered by a large language model, evaluates whether to perform the task independently or to incorporate visual modeling components. Combining language models and vision modules, MedVersa leverages both visual and linguistic supervision for training, as well as generates multimodal outputs, showcasing its versatility and potential for real-world applications in medical image interpretation.

Current medical AI systems are often limited to narrow applications, hindering widespread adoption. We present MedVersa, a generalist foundation model trained on tens of millions of compiled medical instances. MedVersa unlocks generalist learning from multimodal inputs and outputs, representing the first example of a generalist model reaching competitive performance with leading specialized solutions across a variety of medical imaging scenarios. MedVersa achieves state-of-the-art performance in nine tasks, sometimes outperforming counterparts by over 10%. Radiologist evaluation shows MedVersa-generated reports get superior performance in 95% of normal studies, while matching or exceeding human reports in 71% of cases overall. User studies showed notable reductions in report writing time and discrepancies with the use of MedVersa. Our findings underscore the value of flexible, multimodal AI systems in advancing medical image interpretation and supporting clinical expertise.

## Introduction

The field of medical artificial intelligence (AI) has been advancing at a rapid pace, ushering in a new era of diagnostic accuracy and patient care. Within this dynamic landscape, researchers have been focusing their efforts on developing solutions for specific tasks, such as identifying chest pathologies [1–5] and classifying skin diseases [6–8]. Similarly, the majority of medical AI products approved by the US Food and Drug Administration for clinical use have been designed to address one or two specific tasks [9]. However, this task-specific approach may limit the real-world clinical applications of these AI systems, as they may not be able to adapt to the diverse and complex needs of healthcare settings [10, 11].

Addressing this concern, generalist medical artificial intelligence (GMAI) was proposed to utilize recent advances in foundation models [12] for more flexible problem solving [13]. However, contemporary GMAI models have been designed to learn from natural language supervision [13–17]. Although these models work well in vision-language tasks, it does not readily apply to a majority of vision-centric problems, such as detection and segmentation, which are indispensable to medical image interpretation [18–20].

By functioning a large language model as an optimizable orchestrator, MedVersa unlocks generalist learning from multimodal inputs and outputs (Fig. 1), distinguishing it from traditional approaches [13–17]. To develop and validate MedVersa, we proposed a three-stage pipeline for capability development, model validation, and impact study, integrating dataset compilation, multimodal architecture design, efficient training, multicohort validation, expert-blinded report comparisons, and workflow analysis to enhance clinical AI applications and report efficiency (Fig. 2). To develop MedVersa, we compiled 29 million instances for multifaceted medical image interpretation (Fig. 3a). MedVersa is the first foundation model that reaches highly competitive performance with leading task-specific solutions across various medical tasks, often outperforming counterparts by large, significant margins (Fig. 3b). It is also the first demonstration that generalist learning across vision and language tasks yields mutual benefits (Fig. 3c). In practice, MedVersa surpasses MAIRA [21] and Med-PaLM M [14] in radiology report generation, and excels in visual localization, outperforming the established object detector [22]. Additionally, it outperforms specialized solutions in longitudinal studies captioning, region describing, open-ended VQA, and chest pathology classification, with performance validated on 6 external cohorts, proving its robustness and generalizability.

## Results

### 2.1. Enhancing medical image understanding with generalist learning

Generalist learning across all tasks outperforms training with task-specific data, as demonstrated by Fig. 3a, highlighting the performance gains achieved through the integration of generalist learning, particularly in the context of medical image interpretation. Chest radiographs were chosen as the representative imaging modality due to their inherent complexity and the wide variety of analytical tasks they encompass. This modality provides a multifaceted challenge, making it an ideal platform for assessing the robustness and versatility of the generalist learning paradigm.

The results show that generalist learning led to a mean performance improvement of 6.4% compared to models trained exclusively on vision-language data. This indicates that vision-centric training within the generalist learning framework enhances the model's ability to process visual information comprehensively, enabling better interpretation and utilization of visual cues across diverse contexts. Additionally, combining vision-centric and vision-language tasks during generalist learning

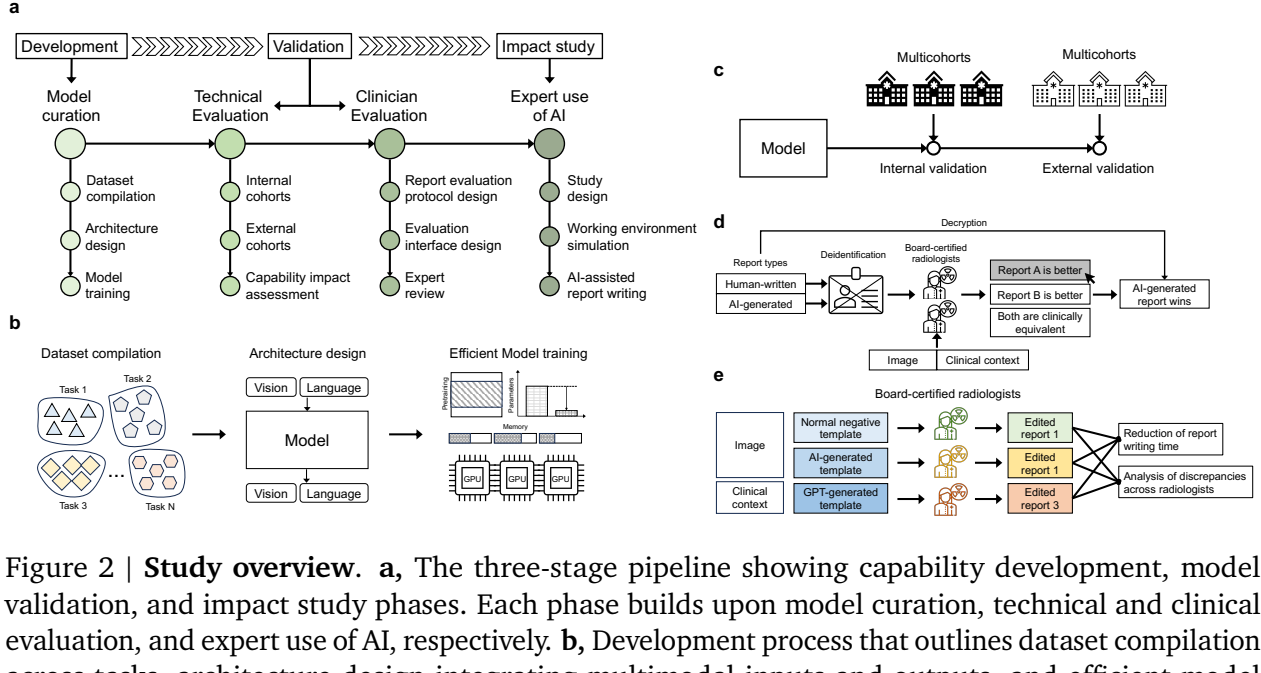


**Figure 2 | Study overview.** **a**, The three-stage pipeline showing capability development, model validation, and impact study phases. Each phase builds upon model curation, technical and clinical evaluation, and expert use of AI, respectively. **b**, Development process that outlines dataset compilation across tasks, architecture design integrating multimodal inputs and outputs, and efficient model training strategies. **c**, Validation framework demonstrating internal and external validation across multicohorts, with emphasis on task improvements through generalist learning and clinical relevance assessment. **d**, Protocols for comparing human-written and AI-generated reports through blinded assessment by board-certified radiologists to ensure unbiased evaluation. **e**, Impact study workflow showing the comparative analysis of normal negative template, AI-generated template, and GPT-generated template to assess reduction in report writing time and discrepancies across radiologists.

resulted in a mean performance improvement of 5.3% over models trained solely on vision-centric tasks. This finding highlights the importance of linguistic supervision in improving the model's capacity for visual comprehension and reasoning. By integrating both language and structured supervision into the training process, MedVersa develops more generalized and comprehensive representations, capturing a broader range of features, relationships, and semantic meanings. These results underscore the significance of developing generalist medical AI models capable of supporting multimodal outputs and effectively learning from multimodal supervision to achieve optimal performance and generalization across a wide spectrum of medical image interpretation tasks.

## 2.2. Report generation

Table 1 presents the evaluation results on three sections: findings, impression, and all (concatenation of findings and impression) using five evaluation metrics: BLEU-4 [23], BertScore [24], CheXbert [25], RadGraph [26], and RadCliQ [27]. For the findings section, among the baselines, MAIRA [21] achieves a higher BLEU-4 score of 14.2, while Med-PaLM M [14] produces a better RadGraph score of 26.7, both of which are the current state-of-the-art. Since MAIRA and Med-PaLM M are not publicly accessible, we additionally included two extra baselines, ClsGen [28] and BiomedGPT [29], for consistent comparisons across different sections. Both ClsGen and BiomedGPT achieve higher BLEU-4 scores than Med-PaLM M.

The proposed MedVersa was evaluated across all sections and metrics. It outperforms all baselines in the findings section with a BLEU-4 score of 17.8 (vs. 14.2 of MAIRA), a CheXbert score of 46.4

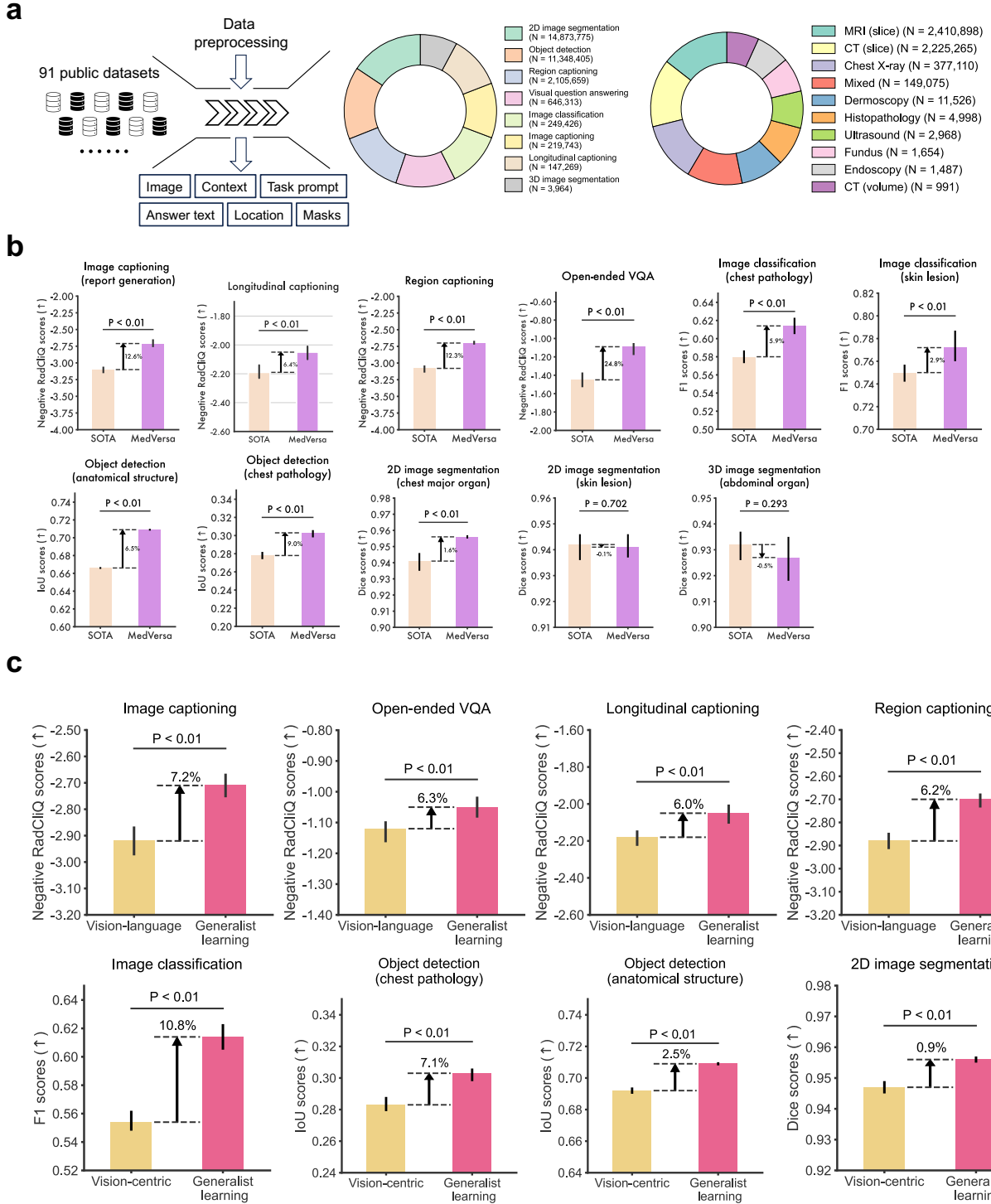


**Figure 3 | Dataset and model performance.** **a**, Data preprocessing pipeline showing the integration of public datasets and their transformation into varied components including image, context, task prompt, answer text, location, and masks, with a circular chart (values are log-transformed) showing the distribution of different tasks in the dataset. **b**, Comparisons to state-of-the-art specialized solutions. Relative improvements and p-values are also displayed. **c**, Performance gains brought by doing generalist learning over using vision-language or vision-centric data for model training. Chest radiographs were chosen for their diverse analytical tasks.

**Table 1 | Experimental results of 4 vision-language tasks: image captioning (report generation), longitudinal captioning, open-ended visual question answering, and region captioning.** Specifically, the evaluation of radiology reports was conducted on three different sections: findings, impression, and all (concatenation). Results of MAIRA and Med-PaLM M are cited from their papers as their models have not been released. Numbers in brackets are the 95% confidence intervals. ↓ indicates that the lower results are better. VQA stands for visual question answering. P-values are calculated between the best and second best RadCliQ scores.

Tasks	Models	Eval. section	BLEU-4	BertScore	CheXbert	RadGraph	RadCliQ (↓)	P-value
Image Captioning (report generation)	ClsGen	Findings	11.9 [11.4, 12.3]	40.5 [39.8, 41.1]	42.6 [41.9, 43.4]	23.5 [22.8, 24.2]	3.28 [3.24, 3.33]	
	BiomedGPT	Findings	12.0 [11.5, 12.4]	40.8 [40.2, 41.5]	43.3 [42.8, 43.7]	23.4 [22.7, 24.0]	3.25 [3.21, 3.29]	
	GPT-4	Findings	6.3 [5.7, 7.0]	25.4 [24.5, 26.4]	37.9 [37.0, 38.7]	11.3 [10.7, 12.1]	3.95 [3.91, 4.00]	< 0.01
	MAIRA	Findings	14.2 [13.7, 14.7]	-	44.0 [43.1, 44.9]	24.3 [23.7, 24.8]	3.10 [3.07, 3.14]	
	Med-PaLM M (85B)	Findings	11.5 [-, -]	-	-	26.7 [-, -]		
	MedVersa	Findings	17.8 [17.2, 18.4]	49.7 [49.0, 50.4]	46.4 [45.5, 47.4]	28.0 [27.3, 28.7]	2.71 [2.66, 2.75]	
	ClsGen	Impression	8.5 [7.6, 9.3]	38.0 [37.3, 38.6]	48.7 [48.0, 49.5]	18.8 [18.0, 19.7]	3.25 [3.18, 3.33]	
	BiomedGPT	Impression	10.2 [9.4, 11.0]	37.4 [36.7, 38.2]	49.2 [48.4, 49.9]	20.0 [19.2, 20.7]	3.09 [3.01, 3.16]	
	GPT-4	Impression	5.5 [4.8, 6.2]	17.2 [16.6, 17.9]	22.5 [21.6, 23.4]	6.4 [5.7, 7.2]	5.39 [5.31, 5.48]	< 0.01
	MedVersa	Impression	13.7 [12.7, 14.7]	48.9 [48.0, 49.8]	52.4 [51.3, 53.5]	25.7 [24.6, 26.9]	2.66 [2.60, 2.71]	
Longitudinal captioning	ClsGen	All	13.7 [13.0, 14.3]	42.4 [41.6, 43.1]	44.3 [43.2, 45.4]	25.2 [24.4, 26.0]	3.20 [3.14, 3.25]	
	BiomedGPT	All	14.2 [13.5, 14.8]	42.0 [41.4, 42.6]	44.6 [44.1, 45.2]	25.8 [25.1, 26.5]	3.07 [3.01, 3.14]	< 0.01
	GPT-4	All	6.7 [6.0, 7.3]	19.7 [19.2, 20.3]	25.5 [24.8, 26.3]	8.7 [8.1, 9.5]	4.99 [4.95, 5.03]	
	MedVersa	All	16.0 [15.3, 16.7]	47.4 [46.6, 48.2]	46.6 [45.3, 47.8]	30.0 [29.1, 30.8]	2.74 [2.69, 2.79]	
Open-ended VQA	EKAID	All	40.4 [39.9, 41.0]	69.1 [68.7, 69.5]	49.1 [48.7, 49.4]	20.4 [19.9, 20.9]	2.19 [2.14, 2.23]	
	GPT-4	All	9.2 [8.6, 9.7]	21.8 [21.2, 22.5]	27.6 [27.0, 28.3]	10.3 [9.6, 11.0]	4.04 [3.99, 4.10]	< 0.01
	MedVersa	All	44.7 [43.7, 45.6]	71.4 [70.6, 72.2]	50.0 [49.5, 50.6]	23.7 [22.6, 24.9]	2.05 [2.01, 2.10]	
	PTLM	All	25.2 [24.4, 26.0]	64.7 [64.1, 65.5]	78.3 [77.3, 79.2]	30.4 [29.7, 31.0]	1.64 [1.57, 1.71]	
Region captioning	BiomedGPT	All	27.1 [26.5, 27.7]	67.2 [66.5, 67.9]	80.6 [79.8, 81.3]	31.6 [31.0, 32.1]	1.45 [1.37, 1.52]	
	GPT-4	All	11.3 [10.9, 11.8]	31.3 [30.8, 31.9]	41.5 [40.9, 42.1]	19.8 [19.3, 20.4]	3.51 [3.44, 3.57]	
	MedVersa	All	31.2 [30.7, 31.8]	76.5 [75.9, 77.1]	85.1 [84.6, 85.6]	33.4 [32.7, 34.2]	1.09 [1.06, 1.12]	
	MinIGPT	All	5.1 [4.6, 5.5]	36.6 [36.3, 37.0]	55.3 [54.9, 55.8]	18.3 [17.9, 18.6]	3.08 [3.05, 3.13]	
Region captioning	BiomedGPT	All	4.5 [4.1, 5.0]	32.3 [32.9, 32.6]	48.4 [48.0, 48.9]	13.4 [13.1, 13.7]	3.62 [3.57, 3.67]	
	GPT-4	All	3.2 [2.9, 3.5]	21.5 [21.0, 22.1]	19.8 [19.2, 20.4]	5.6 [5.1, 6.2]	5.38 [5.33, 5.42]	< 0.01
	MedVersa	All	8.4 [8.2, 8.7]	43.8 [43.6, 44.1]	60.7 [60.4, 61.1]	22.8 [22.5, 23.1]	2.70 [2.68, 2.71]	

(vs. 44.0 of MAIRA), and a RadGraph score of 28.0 (vs. 26.7 of Med-PaLM M), establishing its superiority and setting the new state-of-the-art in capturing both the linguistic and clinical aspects of radiology reporting. Particularly noteworthy is that the results of Med-PaLM M were obtained from a significantly larger model, with ten times more parameters than those of MedVersa. This implies that the latter model is more advantageous in terms of training and inference efficiency. For the impression section, MedVersa surpasses BiomedGPT in all evaluation metrics, and the same superiority is maintained when all sections are combined. We performed external validation on the IUX-ray dataset [30] (Table 2), where MedVersa keeps maintaining a notable advantage over BiomedGPT.

### 2.3. Clinician evaluation

The evaluation pipeline was designed to ensure objective and unbiased assessment of radiological reports (Fig. 4a). Board-certified radiologists received medical images along with essential clinical information, including patient demographics, comparative data, and study indications. This clinical context helped guide their interpretations while reflecting real-world scenarios, ensuring that evaluations remained grounded in practical clinical applications. The same imaging and clinical data were processed through the AI model to generate automated reports, maintaining consistency in the input data across both human and AI assessments. To maintain objectivity, the human-written and AI-generated reports underwent a random shuffling process, becoming “Report A” and “Report B”. This blinding mechanism prevented radiologists from identifying report origins or being influenced by recognizable patterns, thereby eliminating potential biases that could skew the evaluation results. Fig. 4b presented the interface design that radiologists used during the evaluation process, featuring an intuitive layout that facilitated efficient and systematic review of the reports. During each

**Table 2 | External validation results.** We evaluated six capabilities (i.e., image captioning, image classification, object detection, 2D image segmentation, open-ended visual question answering, and region captioning) on unseen external cohorts. For each capability, we compared MedVersa with its best performing baseline from Table 1. For classification, detection, and segmentation tasks, we used the mean F1 score, mean IoU (Intersection over Union), and mean DICE score as the evaluation metrics, respectively. For other tasks, we reported the results of RadCliQ. Numbers in brackets are the 95% confidence intervals. P-values are presented. ↓ indicates that the lower results are better.

Capabilities	Datasets	Models	Metrics	Results	95% CIs	P-values
Image captioning	IUX-ray	BiomedGPT MedVersa	RadCliQ (↓)	3.12 2.57	[3.04, 3.17] [2.54, 2.60]	P < 0.01
Image classification	CheXpert	DAM MedVersa	Mean F1 score	0.653 0.734	[0.633, 0.669] [0.712, 0.756]	P < 0.01
Object detection	NIH ChestX-ray	YOLO MedVersa	Mean IoU	0.223 0.239	[0.210, 0.235] [0.225, 0.254]	P = 0.082
2D image segmentation	CheXmask	nnSAM MedVersa	Mean DICE score	0.923 0.955	[0.917, 0.928] [0.952, 0.957]	P < 0.01
Open-ended VQA	IUX-ray	BiomedGPT MedVersa	RadCliQ (↓)	1.68 1.12	[1.62, 1.76] [1.07, 1.17]	P < 0.01
Region captioning	MS-CXR	MiniGPT MedVersa	RadCliQ (↓)	3.43 3.29	[3.38, 3.48] [3.23, 3.35]	P < 0.01

evaluation round, radiologists examined two reports alongside the corresponding image and clinical data, choosing whether Report A was superior, Report B was superior, or both reports were clinically equivalent. This three-choice system allowed for nuanced comparison while capturing the practical reality that reports might be equally suitable for clinical use.

The comparative analysis revealed that AI-generated reports demonstrated remarkable performance across various study types (Fig. 4c). In the overall assessment, where radiologists remained blinded to report origins, AI reports matched or exceeded human-generated reports in 71% of cases. This high percentage of equivalence or superiority suggested that AI systems had reached a significant milestone in medical report generation. For abnormal studies with more complex findings, AI maintained strong performance, with reports being equivalent to or preferred over human reports in 58% of cases. This performance in challenging cases demonstrated the AI's capability to handle intricate medical interpretations that traditionally required substantial human expertise. The AI system particularly excelled in normal studies, where 95% of its reports were either equivalent to or favored over human reports. This exceptional performance in routine cases suggested a potential role for AI in streamlining workflow for standard examinations, allowing radiologists to focus more attention on complex cases.

A structured scoring system was implemented to ensure consistent evaluation of report quality (Fig. 4d). Radiologists employed a numbered scoring system where 1 signified major findings with significant errors, 2 indicated minor findings and less critical errors, 4 represented significant positive aspects such as well-identified areas, and 5 denoted minor positive aspects including small improvements or clear regions. This systematic approach to scoring enabled quantitative analysis of report quality while capturing both critical errors and positive attributes. The evaluation process culminated in detailed case comparisons (Fig. 4e), which presented examples featuring medical images, patient context, report content, expert commentary, and final ratings for both human-written and AI-generated reports.

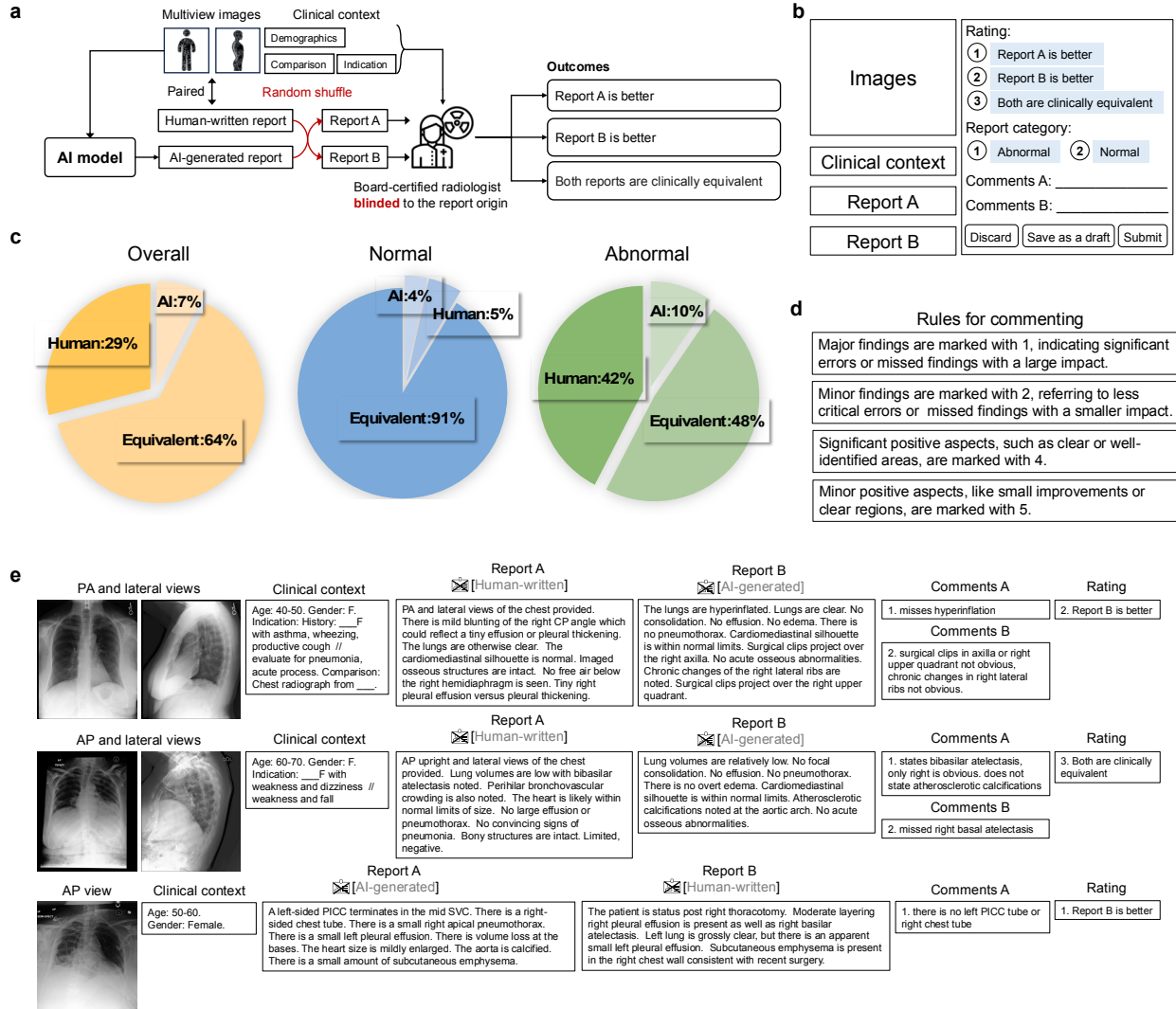


**Figure 4 | Clinical evaluation.** **a**, Evaluation pipeline showing the blinded assessment process where board-certified radiologists compare randomly shuffled, deidentified human-written and AI-generated reports based on multiview images and clinical context. **b**, Interface design for radiologist evaluation, including rating options and report categorization. **c**, Quantitative assessment results showing the distribution of preferences for human versus AI reports across overall, abnormal, and normal cases. **d**, Protocols for making comments on reports. **e**, Cases demonstrating the comparison between human-written and AI-generated reports, including image, clinical context, report content, radiologist comments, and ratings.

## 2.4. User study for MedVersa-assisted report writing

Our study established a comprehensive workflow for evaluating the clinical impact of AI-generated radiology reports through collaboration between radiologists and AI, as illustrated in Fig. 5a. We recruited ten board-certified radiologists through a specialized medical image annotation company in India. The study utilized randomly selected chest radiographs from the MIMIC-CXR dataset. We developed a custom evaluation platform (Fig. 5b) that integrated several key components: a DICOM viewer for image interpretation, a worklist interface, and a report editing interface where radiologists could modify and finalize their reports. The platform's integrated timer tracked time spent on each case. The preparation phase included providing participants with a detailed study task protocol and an instructional video, completing a standardized training phase of 25 cases to ensure platform familiarity, and conducting an interactive orientation meeting where we demonstrated platform functionality, reviewed task requirements, and addressed any remaining questions about the study procedures.

For the main evaluation, each radiologist interpreted 75 unique chest radiographs under three different reporting scenarios: (1) starting with a standard negative template (as per routine radiology workflow), (2) starting with a GPT-4o-generated report draft, or (3) starting with our AI-generated report draft. Cases were randomly and evenly distributed across these three scenarios, with each radiologist reading 25 cases per scenario. For each case, radiologists were tasked with reviewing the chest radiograph and modifying the provided template or draft to produce a clinically accurate final report that would meet the standards of clinical practice. To eliminate potential recall bias and need for washout periods, each radiologist interpreted a case only once, while the same case was interpreted under different scenarios across different radiologists, ensuring balanced distribution of case complexity. We evaluated two key dimensions of reporting performance: discrepancy and efficiency. For discrepancy, we compared the “findings” section of each final report against those of the other nine radiologists for the same case, using an adapted version of FineRadScore [31]. For each report, we calculated its FineRadScore against each of the other nine reports and averaged these scores to obtain an average discrepancy score (Fig. 5c), effectively penalizing reports that deviated from the consensus. Specifically, we focused on urgent and emergent discrepancies, as these most directly impact patient care, highlighting the critical importance of achieving consensus in high-stakes scenarios. We chose this peer-to-peer comparison over using the original ground truth reports because those reports often contain information not available to our readers or models—such as comparisons to prior imaging studies—which could introduce bias. By focusing on the radiologists' reports, all based on the same available data, we ensured that our assessment accurately reflected consistency within the group. Reporting efficiency was measured through the platform's integrated timer.

The analysis of urgent and emergent discrepancies in radiological reports reveals significant variations in performance across different AI systems and time intervals. As shown in Fig. 5d, we examine these discrepancies across two time intervals (5–10 and <5 minutes) for three different scenarios: our model, GPT-4o, and the normal template. Our model consistently achieves lower discrepancy rates across different writing time periods, indicating its effectiveness in managing discrepancies across varying writing durations. Specifically, in the 5–10 minute interval, our model demonstrates a notable advantage over GPT-4o and the normal template, achieving the lowest average number of urgent/emergent discrepancies. Our model maintains approximately 20% fewer discrepancies compared to the other systems, reflecting greater consistency and reliability in identifying urgent and emergent issues during report writing. GPT-4o and the normal template perform similarly during this interval, with neither showing a clear advantage in reducing discrepancies over time..

The impact of AI assistance on radiology reporting time varies significantly based on radiologists'

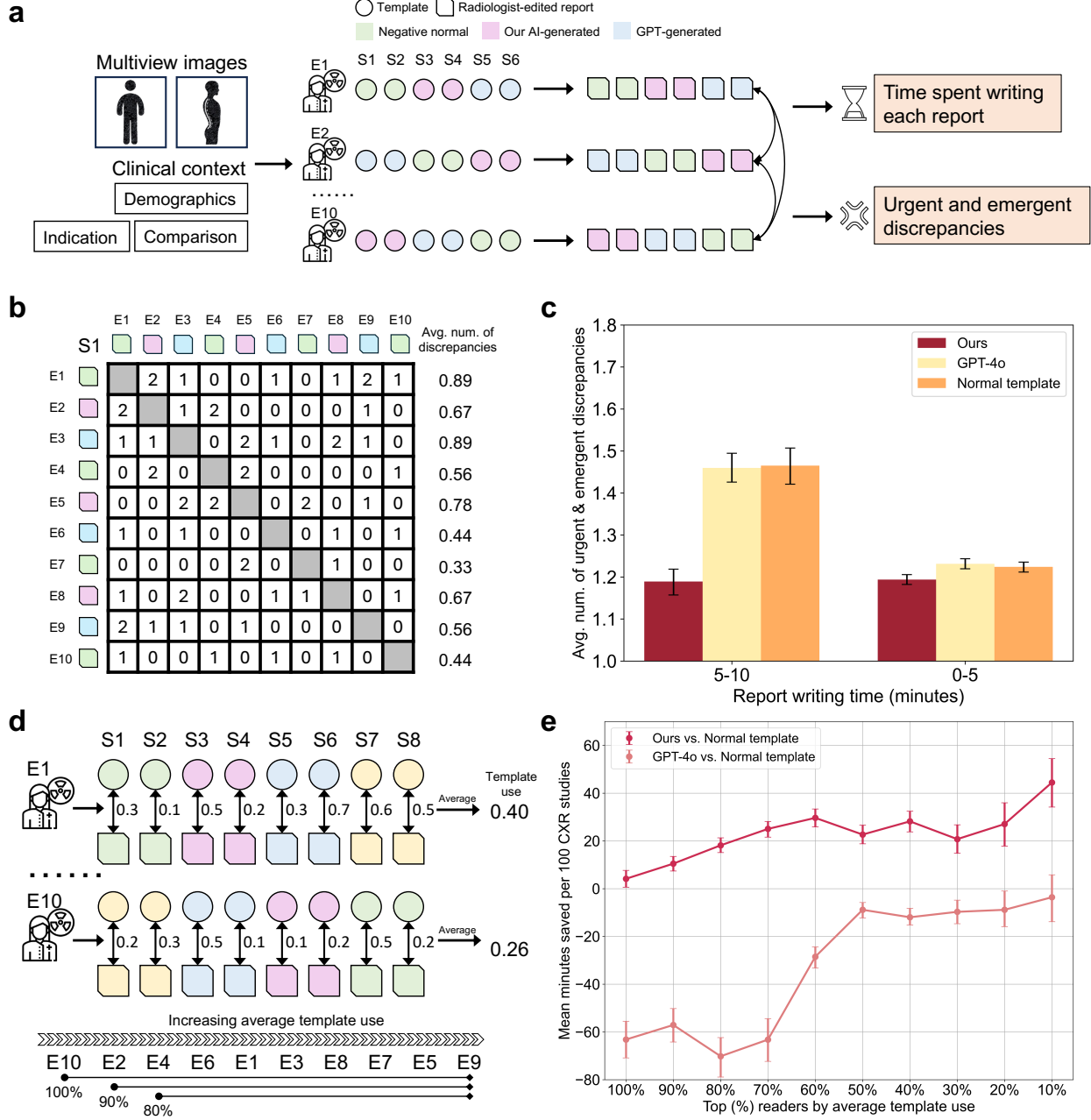


**Figure 5 | Clinical impact study.** **a**, Study design showing multiple board-certified radiologists (E1-E10) editing reports based on different templates (negative normal, our AI-generated, and GPT-generated) for multiple studies (S1-S6), measuring time spent and discrepancies. **b**, Matrix visualization of urgent and emergent discrepancies across experts and studies, with average number of discrepancies per expert. **c**, Comparison of average number of urgent and emergent discrepancies across different report writing time intervals for different template types. **d**, Detailed template usage patterns across different studies and experts, with average template utilization rates shown. **e**, Time saved in report writing compared to normal template usage, stratified by top percentage of readers based on average template use.

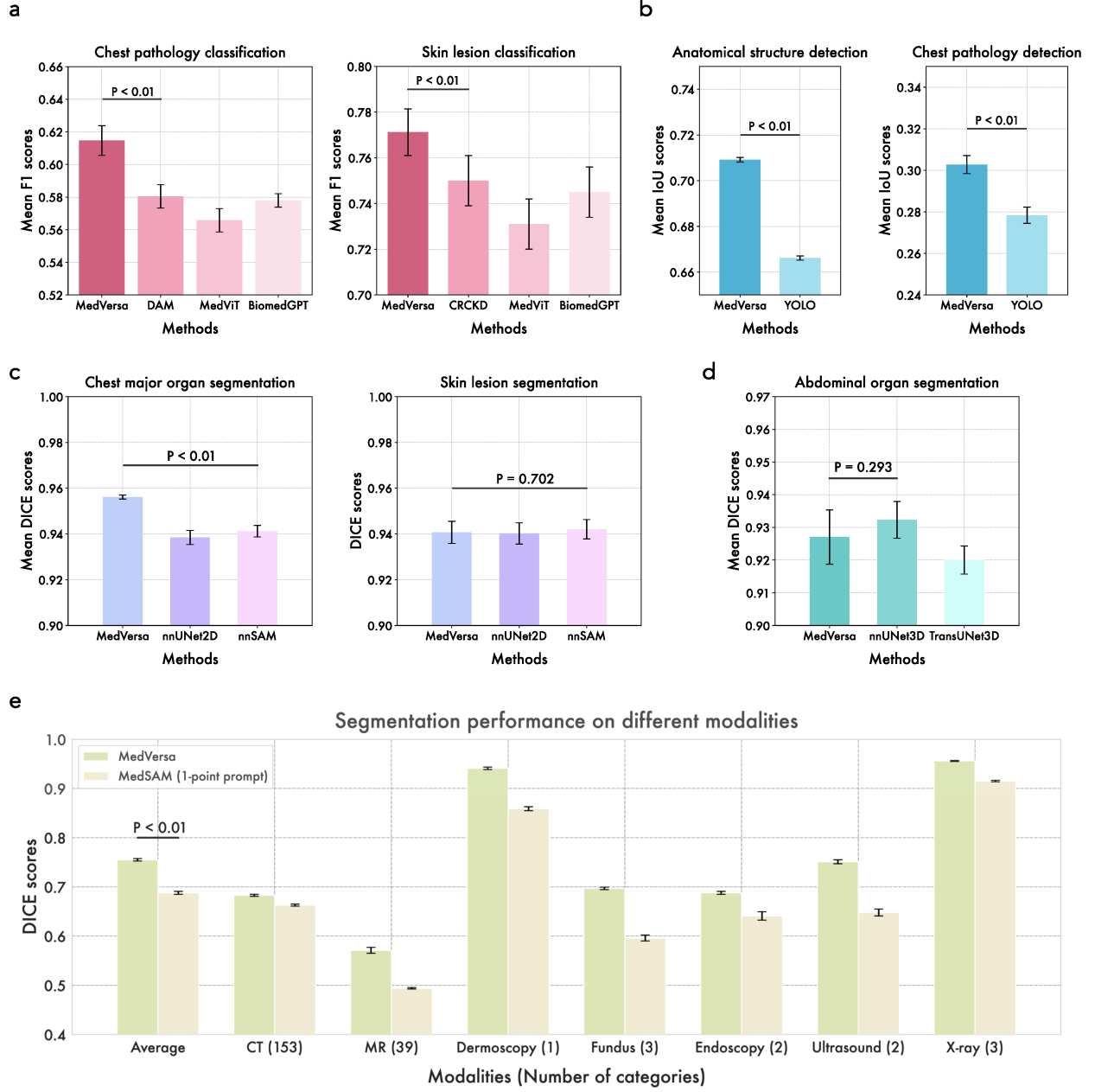
template usage patterns. Template use is measured by calculating the average semantic similarity between the template referred (our model, GPT-4o, or a standard negative template) and the corresponding final report (Fig. 5e) using the RaTEScore metric [32]. A higher similarity score indicates a stronger preference for using the template, which may be because the template meets their requirements for accuracy and/or aligns with their personal reporting style. In practice, this means that radiologists with high template use often make focused edits to ensure clinical accuracy while retaining much of the original template, whereas radiologists with low template use tend to discard templates or large parts of them entirely and rewrite the report from scratch. As shown in Fig. 5f, our model consistently reduces reporting time across radiologist groups, with efficiency gains becoming more pronounced as reliance on templates increases. This upward trend highlights our model’s adaptability, with time savings growing steadily and peaking at around 50 minutes saved per 100 studies. Our hypothesis is that the extent to which radiologists use templates may influence how AI impacts their work. In contrast, GPT-4o shows less favorable results, as demonstrated in Fig. 5f. For radiologists with low template use, GPT-4o leads to a notable increase in time required, with the mean time cost rising by approximately 60 minutes. Even as template use increases, GPT-4o only begins to show marginal time savings in the top 20% of radiologists, and its performance remains far below that of our model at all levels of template reliance. The comparison highlights our model’s ability to cater to a wide spectrum of radiologist preferences, offering consistent and increasing time savings as template reliance grows, whereas GPT-4o struggles to achieve similar levels of efficiency, particularly for radiologists less inclined to use templates.

## 2.5. Vision-centric tasks

Fig. 6a presents the experiment results of image classification. For chest pathology classification, MedVersa demonstrates superior performance over DAM [33], MedViT [34], and BiomedGPT [29] with an average F1 score of 0.615. This pattern of outperformance extends in 29 out 33 pathologies (see Fig. 9a), including both common (e.g., lung opacity, pulmonary edema, spinal fracture) and less common ones (e.g., hydropneumothorax, bronchiectasis), which indicates MedVersa’s strong diagnostic accuracy across various conditions. In skin lesion classification, the advantage of MedVersa is also noticeable. The average F1 score of MedVersa is 0.772, appreciably above the scores of CRCKD [35], MedViT, and BiomedGPT, underscoring MedVersa’s effectiveness in classifying skin conditions (Fig. 6a). It is worth noting that MedVersa outperforms CRCKD by significant margins in benign keratosis-like lesions (bkl), which has a diverse range of subtypes (see Fig. 9b). This further demonstrates the generalization ability of MedVersa. For external validation (Table 2), MedVersa again surpasses DAM by a large margin on CheXpert [3], which also exceeds the mean performance of radiologists (F1 score: 0.734 vs. 0.610) [14].

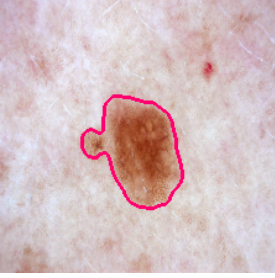
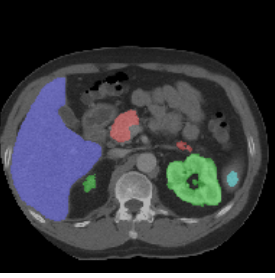
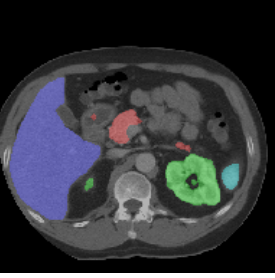
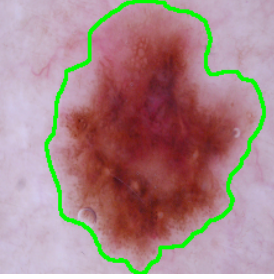
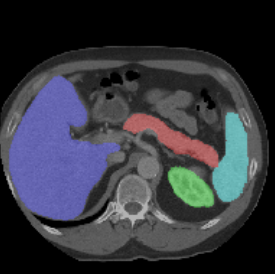
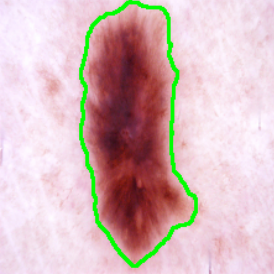
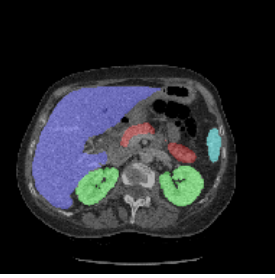
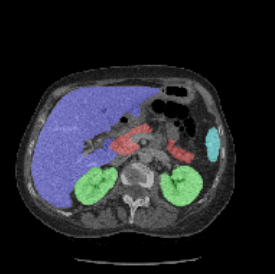
For object detection, MedVersa exhibits competitive performance, surpassing YOLO [22] by noticeable, consistent margins in the detection of a variety of anatomical structures (Fig. 5b), with most IoU scores on certain structures surpassing 0.6 (Fig. 10a). It shows particularly high effectiveness in the detection of lung zones. When identifying chest pathologies (Fig. 5b), MedVersa maintains a higher average performance compared to YOLO (0.303 vs. 0.278), and the superiority is also notable in the detection of 27 out of 33 conditions (Fig. 10b). On the external cohort NIH ChestXray, MedVersa also outperforms YOLO by an average of nearly two percent in detecting common chest pathologies (Table 2).

Regarding segmentation tasks, MedVersa demonstrates competitive results, performing competitively to nnUNet [36] and nnSAM [37]. All three approaches perform fairly well in segmenting major chest organs and skin lesions (Fig. 5c and Fig. 11a). Nonetheless, MedVersa outperforms nnUNet and nnSAM by significant margins in chest major organ segmentation. In the task of abdominal organ



**Figure 6 | Experimental results of vision-centric tasks.** **a**, MedVersa was compared to three baseline models: DAM (Deep AUC Maximization), MedViT, and BiomedGPT on chest pathology classification. For skin lesion classification, we replaced DAM with CRCKD (Categorical Relation-preserving Contrastive Knowledge Distillation), a model specifically designed for this task. **b**, We compared MedVersa against YOLO (version five) on two detection tasks: anatomical structure and chest pathology detection. **c**, For 2D image segmentation, we primarily compared MedVersa with nnUNet2D and nnSAM for segmenting major organs in the chest and skin lesions. **d**, For 3D image segmentation, MedVersa was compared with nnUNet3D and TransUNet3D for segmenting abdominal organs. **e**, We investigated the development of a versatile segmentation model for various imaging modalities, extending the functionality of MedVersa. The baseline approach, MedSAM, is a segment anything model finetuned specifically on medical segmentation data. The evaluation metrics of classification, detection, and segmentation tasks are F1, IoU (Intersection over Union), and DICE similarity scores, respectively.

**Table 3 | Segmentation results of skin lesions and abdominal organs.** For abdominal organ segmentation, the red, blue, green, and aqua colors represent the pancreas, liver, kidney, and spleen, respectively.

Skin lesion segmentation		Abdominal organ segmentation	
Ground truth	MedVersa	Ground truth	MedVersa
			
			
			

segmentation (Fig. 5d and Fig. 11b), MedVersa also shows competitive performance to nnUNet3D which uses more complex and time-consuming data augmentation techniques. Table 3 showcases the segmentation results of skin lesions and abdominal organs.

Fig. 5e presents a comparative analysis of the segmentation performance between MedVersa and MedSAM (1-point prompt) models across varied imaging modalities. MedVersa, based on its architecture, shows a consistently higher DICE score compared to MedSAM in different modalities, indicating its superior ability to accurately segment different types of medical images. The modalities examined include CT, MR, dermoscopy, fundus, endoscopy, ultrasound, and chest x-ray. On average, MedVersa achieves a DICE score of 0.755, significantly outperforming the baseline approach which is a SAM model [38] finetuned on the medical segmentation data. We believe that this performance advantage can be partly attributed to the features produced by the language model which may encode underlying relationships between different categories.

## 2.6. Longitudinal captioning, visual question answering, and region captioning

In longitudinal captioning, the model is typically tasked with drawing a comparative conclusion between two groups of images collected at different periods. This presents a significant challenge for image interpretation, as models must work with multiple images to analyze various anatomical structures, extracting features and identifying subtle disease-related changes. As shown in Table 1, the baseline method EKAID builds complex anatomical structure-aware graphs to encode anatomical and disease features for recognizing the differences between CXR studies. In contrast, MedVersa adopts a straightforward yet effective way to process longitudinal images (see. Fig. 7e). Moreover, MedVersa largely outperforms EKAID across different metrics (BLEU-4: 44.7 vs. 40.4, BertScore: 71.4 vs. 69.1, CheXbert: 50.0 vs. 49.1, RadGraph: 23.7 vs. 20.4, RadCliQ: 2.05 vs. 2.19). The same performance advantage is also present in the comparison with GPT-4.

As Table 1 displays, MedVersa outperforms PTLM [39], a leading model for open-ended medical VQA, by an average of six percent across BLEU-4, BertScore, CheXbert, and RadGraph metrics. Additionally, MedVersa achieves a 30% lower RadCliQ score compared to PTLM. The 95% confidence intervals suggest that MedVersa’s improvements are statistically significant. Results on the external cohort further confirm MedVersa’s advantages (Table 2). Notably, MedVersa also outperforms BiomedGPT and GPT-4 by substantial margins. To enhance MedVersa’s medical VQA capabilities, we also focused on its ability to process multimodal images. By fine-tuning the pretrained 2D vision encoder and adapter while keeping the language model frozen, we trained the model using the PMC-VQA dataset from PubMed Central Open Access (which includes multimodal medical images) and PathVQA (histopathology images), following the BiomedGPT training approach. Validation on the PathVQA and VQA-RAD test sets highlighted MedVersa’s superior performance. On PathVQA, MedVersa achieved superior accuracy of 64.6%, compared to BiomedGPT’s 58.0%. This included 46.5% accuracy on open-ended questions (versus BiomedGPT’s 28.0%) and 82.8% on closed-ended questions (versus BiomedGPT’s 88.0%). In zero-shot classification on VQA-RAD, MedVersa reached a mean accuracy of  $63.3\% \pm 2.5\%$ , outperforming BiomedGPT ( $54.7\% \pm 5.7\%$ ) and GPT-4 ( $53.0\% \pm 6.7\%$ ).

In the region captioning task, MedVersa demonstrates a clear advantage over MiniGPT across multiple metrics, even though MiniGPT can outperform GPT-4 and BiomedGPT. The RadCliQ score, which comprehensively evaluates the lexical and clinical significance of generated text, is substantially lower for MedVersa at 2.70 versus 3.08 for MiniGPT, suggesting captions of MedVersa are semantically more aligned with reference standards. The result from an external cohort further confirms the benefit of MedVersa, as shown in Table 2.

## Discussion

To the best of our knowledge, MedVersa is the first GMAI model that supports multimodal outputs, inputs, and on-the-fly task specification. Trained on MedInterp, a medical dataset encompassing 11 different tasks across seven imaging modalities, MedVersa sets the new state-of-the-art in report generation and outperforms highly competitive specialist models in both vision-language and vision-centric tasks. The development of MedVersa potentially unlocks new opportunities to build more versatile GMAI models. More detailed perspectives are provided in the following.

**MedVersa integrates visual and linguistic supervision through its multimodal-output design.** MedVersa distinguishes itself from previous endeavors by seamlessly incorporating both visual and textual guidance in its training process. This unique approach allows MedVersa to tackle a wide range of medical tasks, from generating radiology reports to segmenting medical images. The model’s

ability to assimilate knowledge from various input types and generate multimodal outputs results in the development of general and robust shared representations, which helps boost the model accuracy on the tasks and alleviate potential biases in the data. The incorporation of multimodal outputs in MedVersa's also aligns with the latest progress in generative AI, where the use of varied and all-encompassing training data has yielded promising results. By gaining insights from both visual and textual cues, MedVersa constructs a more comprehensive grasp of medical information, paving the way for more precise and dependable diagnoses. Its capacity to adapt to impromptu task specifications renders MedVersa a multifaceted and flexible instrument for diverse clinical applications, establishing its place as a useful resource in medical AI for thorough diagnostics.

**Large language models act as optimizable orchestrators.** Unlike previous endeavors that used large language models as standalone language predictors, the large language model in MedVersa transcends its traditional role by acting as an optimizable orchestrator capable of interpreting medical vision-language data and coordinating with vision modules. This design allows MedVersa to leverage the strengths of both the large language model and specialist components, resulting in a more comprehensive and effective system for medical image interpretation. The integration of vision modules within MedVersa enhances its capability in areas where language-based models traditionally falter, such as detailed image analysis required in chest abnormality detection and skin lesion segmentation. The comprehensive approach, combining the contextual decision-making of the large language model with the precision of vision modules, offers a more robust and versatile diagnostic tool. This new orchestration represents a new step beyond the limitations of previous medical foundation models, offering a new perspective of integrating large language models into generative multimodal medical AI.

**Impact of dataset composition.** The composition of our dataset significantly influences the scope and generalizability of our findings. While we have achieved comprehensive coverage for chest X-rays across various task types, including classification, detection, and report generation, the diversity of tasks for other imaging modalities is currently limited. Specifically, for modalities such as CT, MRI, endoscopy, dermoscopy, ultrasound, and fundus imaging, our annotations are predominantly segmentation masks. This imbalance in task representation across modalities potentially constrains the model's ability to generalize across a broader range of medical imaging tasks. To address this limitation, our future work will focus on expanding the diversity of tasks for non-chest X-ray modalities. We plan to incorporate a wider range of annotation types, such as classification labels, bounding boxes, and descriptive reports, for these other imaging modalities. Additionally, we recognize the importance of incorporating more text-only data to enhance the model's language understanding capabilities in medical contexts. These planned expansions aim to create a more balanced and comprehensive dataset, which should lead to more robust and versatile AI models for medical image interpretation across various specialties and task types.

**Balancing performance across modalities and tasks.** A key challenge in developing generalist medical AI models lies in maintaining consistent performance across different imaging modalities and tasks, given the inherent data imbalance in medical datasets. Our experiments demonstrate that MedVersa addresses this challenge through its domain-aware minibatch gradient descent approach. When extending to new domains like dermoscopy and CT volumes, the model maintained its chest X-ray interpretation capabilities. This stability stems from our localized gradient update mechanism, where task-specific minibatches primarily influence network parameters relevant to the current task-modality pair. The approach enables the model to develop shared representations that support transfer between tasks rather than interference. However, we recognize limitations in our current implementation, as random task selection within each modality may not fully account for differences in task complexity. Future work could explore adaptive sampling strategies that adjust based on model

performance and task difficulty, while incorporating continual learning techniques could enhance the model's ability to maintain balanced performance across an expanding set of medical imaging tasks and modalities.

**Extensible GMAI and beyond.** The system design features a notable level of extensibility, allowing for the practical integration of new vision modules into its existing framework. This aspect of MedVersa enables it to adapt and grow in response to evolving medical imaging techniques and diagnostic requirements. Differing from traditional medical AI models, MedVersa integrates the large language model in the way that provides a extensible platform for the addition of new specialist models as advancements in medical technology occur. This feature ensures that the overall system remains up-to-date and effective in a field characterized by rapid technological changes and emerging diagnostic challenges. As novel medical imaging methods are introduced, MedVersa can be updated to maintain its relevance in the dynamic landscape of medical diagnostics. This modular design not only prepares it for future advancements but also encourages ongoing improvement and innovation within the system. It highlights the potential of MedVersa as an extensible and adaptable solution in medical AI, equipped to address the varied and changing requirements of healthcare practitioners and patients in a continuously evolving medical environment.

**Potential to streamline clinical workflows.** The impact of our work is prominent in offering a unified solution that can help streamline the clinical workflows with medical AI products. In contrast, task-specific models, designed for individual tasks, may complicate or fragment workflows, necessitating the medical professionals to switch between multiple systems. For instance, in a busy metropolitan hospital, the radiology department faces challenges managing a high volume of diverse imaging tasks daily, from urgent chest X-ray interpretations to CT scans requiring detailed analysis. The introduction of MedVersa allows for a seamless transition between these tasks within a single, integrated platform. Previously, radiologists had to switch between multiple specialist AI modules, each with its own interface and diagnostic focus, leading to inefficiencies and delays in patient care. The comprehensive capability of MedVersa to interpret various types of medical images means that radiologists could efficiently work through their caseloads, significantly reducing the turnaround time for diagnostic reports. This streamlined process not only improves operational efficiency but also ensures that patients receive faster diagnoses, leading to quicker treatment decisions and better outcomes, finally increasing the adoption rate of AI products in real-world clinical settings.

**AI-Radiologist collaboration.** A critical consideration in understanding the impact of AI on radiologists' well-being is examining why and how AI may either alleviate or contribute to their challenges. The effectiveness of AI solutions extends beyond their accuracy; factors such as workflow integration, user experience, and the overall ease of the human-AI interaction play pivotal roles. Seamless integration into clinical workflows that enhances rather than disrupts processes, along with user-centered design principles, are essential to achieving meaningful benefits. Importantly, simply accelerating tasks without reducing the cognitive and physical demands on radiology staff may fail to address the underlying contributors to their workload and stress. These nuances underscore a key point: clinical accuracy and efficiency do not automatically translate to clinical utility in healthcare AI. The complexity of human-AI interaction requires a more nuanced approach to assessing AI's role in clinical practice.

**Road to full orchestration.** Recent research has delved into the role of LLMs as orchestrators and agents in multiagent systems [40]. Frameworks such as AutoGen [41] have enabled multiagent conversations, enhancing applications of LLMs. Multiagent debates [42] have been shown to improve factuality and reasoning, while setups that encourage divergent thinking lead to more creative outputs [43]. Additionally, dynamic LLM-agent networks have been proposed to optimize team performance [44], though challenges remain in retaining information and solving complex, multi-step problems

[45]. Emerging patterns in orchestration frameworks highlight evolving strategies for leveraging AI agents [46]. Achieving full orchestration of MedVersa involves several strategic advancements. First, broadening its dataset scope to encompass a wider array of medical data types, such as detailed electronic health records, comprehensive genetic information, and real-time patient monitoring data, is crucial. This diversification will enhance the diagnostic accuracy of MedVersa by providing a more holistic view of patient health. Second, incorporating cutting-edge AI and machine learning modules, particularly in evolving areas of natural language processing and computer vision, will refine its capability to interpret and analyze complex medical datasets accurately. The development and integration of advanced modules for effective data synthesis and nuanced interpretation are essential for providing comprehensive medical insights. This path also includes rigorous attention to ethical, privacy, and security issues, ensuring MedVersa's operation within a framework that prioritizes patient confidentiality and data integrity. Ultimately, the full orchestration of MedVersa aims to transform healthcare delivery through personalized, efficient, and broad-spectrum medical analyses, leading to superior patient care and optimized healthcare processes.

**Limitations.** Despite the advancements, there are inherent limitations that warrant consideration. One primary concern lies in the dependency of MedVersa on the quality and diversity of the data used for training the models. If the dataset is not sufficiently varied or representative of the global population, there is a risk of bias in the AI-generated diagnostics, potentially leading to less accurate outcomes for certain demographic groups. Additionally, the complexity of integrating various vision modules with the large language model poses challenges in ensuring seamless interoperability and maintaining the consistency of the system's overall performance. The dynamic nature of MedVersa, while advantageous for adaptability, also raises questions about the long-term manageability and scalability of the system, especially as it continuously evolves to include new modalities and network modules. Moreover, the interpretability and explainability of the decision-making process of MedVersa remains a critical area. The complex interactions between different AI models can obscure the reasoning behind specific diagnostic conclusions, making it challenging for medical professionals to fully understand and trust the recommendations. These limitations underscore the need for ongoing research and development in enhancing the robustness, transparency, and ethical considerations, ensuring it aligns with the highest standards of clinical practice and patient care.

## Methods

### 4.1. Datasets and data preprocessing

We curated MedInterp to train and evaluate medical FMs for multifaceted medical image interpretation. An overview of MedInterp was presented in Table 4. Specifically, MedInterp consists of 91 publicly available datasets, some of which are associated with more than one task. The details of datasets are listed below, with segmentation-related datasets described in Table 4. We followed the guideline in SAM-Med to preprocess the segmentation data [47].

**MIMIC-CXR.** This is a large, publicly accessible dataset comprising 377,110 chest X-rays (CXR) corresponding to 227,835 radiographic studies performed at the Beth Israel Deaconess Medical Center in Boston, MA [4, 48]. The dataset was fully deidentified, and the protected health information was also removed. We referred to the official split and combined studies with “train” and “validate” tags into the training set, while the rest were included in the test set (for internal validation). The free-text radiology report preprocessing followed the steps in CXR-RePair [49]. Specifically, we extracted sections of indication, comparison, findings, and impression from free-text radiology reports via keywords matching. Then, we filtered out studies with empty findings and impression sections. After

these steps, we can obtain 149,711 (2,144) findings sections and 189,411 (2,212) impression sections. Numbers in parentheses denote the sample size of the test set. Besides, we also extracted complete radiology reports, i.e., reports that have findings and impression sections. This resulted in 122,702 (1,437) complete reports, which were also involved in training and internal validation stages along with sections of findings and impressions. Note that some studies may have more than one CXR, and images of MIMIC-CXR were also used in other tasks.

**Chest ImaGenome.** This dataset augmented the free-text reports of MIMIC-CXR with local annotations derived from both rule-based natural language processing (NLP) and atlas-based bounding box detection [50]. These annotations are intricately linked through CXR ontologies developed by radiologists, forming anatomy-centered scene graphs. We followed the data split of MIMIC-CXR to avoid training and test sets leakage. The chest pathology classification task included 235,721 CXRs with annotations of 33 pathologies (Fig. 4a). A vast majority of CXRs have bounding box annotations of 36 anatomical structures, leading to 8,425,163 boxes in total. We also exploited the anatomy-centered graph-structured annotation of Chest ImaGenome. For chest pathology detection, we first identified connections between pathologies and anatomies. Next, we can assign bounding boxes of anatomies to associated pathologies that were marked positive. A similar strategy was also adopted for region captioning, where connections between sentences from free-text reports and anatomies were extracted using NLP techniques [50]. After this, we had textual captions grounded on anatomies. So the task input would be the box coordinates of anatomies, and the output would be the associated captions.

**Medical-Diff-VQA.** This is a publicly available dataset containing a vast number of question-answer pairs based on CXRs [51]. To construct this dataset, keywords of abnormality and their attributes were first collected. Then, regular expressions were utilized to detect abnormality/disease keywords within the free-text reports of each patient visit in MIMIC-CXR. These identified keywords served as anchor terms to segment the sentences, and nearby text sections were then scanned for the relevant attribute keywords. The accuracy and completeness of the extracted information have been carefully checked by humans and advanced NLP tools. In practice, we leverage the code in an open source repository to generate the datasets [51]. Since open-ended visual question answering is our main focus, we reduced the number of yes/no question-answer pairs by setting the *less\_yes\_no* variable in the code to True. This results in 383,683 normal question-answer pairs, where each pair is associated with one frontal CXR, and 147,269 longitudinal comparisons, where each comparison encompasses two studies, and each study may contain more than one CXR. We used the same data split as in Chest ImaGenome and MIMIC-CXR to avoid training and test information leakage across different datasets. To build a cohort for external validation, we applied the dataset construction code to the free-text reports of IUX-ray [30] to extract 2,883 normal question-answer pairs.

**PMC-VQA.** The PMC-VQA dataset is a large-scale medical visual question-answering resource that contains 226,946 question-answer pairs associated with 149,075 multimodal medical images [52]. PMC-VQA was developed to address the limitations of existing datasets in training high-performing generative-based models for medical visual question answering. The dataset’s questions vary in complexity, from simple identification tasks to more challenging inquiries requiring specialized knowledge.

**PathVQA.** PathVQA is a pioneering medical visual question-answering dataset focused on pathology images, containing 32,795 question-answer pairs derived from 4,998 pathology images [53]. The dataset was created by extracting images and captions from pathology textbooks and digital libraries, using a semi-automated pipeline to generate questions that were then manually verified. Unlike previous medical VQA datasets that primarily used radiology images, PathVQA is unique in its focus on pathology and its emphasis on open-ended questions, making it a more challenging and diverse

resource for medical AI research. The dataset includes various question types, with 49.8% being yes/no questions, 40.9% “what” questions, 6.6% “where” questions, and 1.8% “how” questions.

**VQA-RAD.** VQA-RAD is a pioneering dataset for medical visual question answering, specifically focused on radiology images [54]. The images are sourced from MedPix, an open-access radiology archive of case reports and teaching cases. It covers various question categories, with the majority being yes/no questions (49.8%) and “what” questions (40.9%). Note that we only used the test set from VQA-RAD for external validation, which contains 451 question-answer pairs.

**HAM10000.** This is a bulk collection of multi-source dermatoscopic images of common pigmented skin lesions [55]. The dataset comprises 10,015 image cases and encompasses a diverse collection of significant diagnostic categories within the domain of pigmented lesions. These categories include Actinic keratoses and intraepithelial carcinoma / Bowen’s disease (akiec), basal cell carcinoma (bcc), benign keratosis-like lesions (bkl), dermatofibroma (df), melanoma (mel), melanocytic nevi (nv), and vascular lesions (vasc). For the skin lesion classification task, we used 1,511 images from ISIC 2018 task three as the test set for internal validation [56]. For skin lesion segmentation, we randomly split the dataset into training and test sets. The ratio of the training set to the test set is 9:1. We trained skin classification models on the raw datasets directly without any class balancing skills [57].

**CheXpert.** This is another large public dataset for chest radiograph interpretation, which retrospectively collected the chest radiographic examinations from Stanford Hospital, performed between October 2002 and July 2017 [3]. In our case, we used its test set (500 studies, 668 images) with strong ground truth for externally validating the results of the chest pathology classification task. The test set labels were established through the majority vote of annotations from five radiologists, with three of them being the same as those who annotated the validation set, while the other two were randomly selected. Besides, 200 images in the validation set of CheXpert were also used in the task of chest major organ segmentation.

**IUX-ray.** The dataset contains 7,470 pairs of CXRs and radiology reports [30]. It served as the external validation set for the report generation task. To maintain the consistency of cross-dataset validation, we filtered out reports that do not contain sections of findings and impression simultaneously, resulting in 3,323 studies. Each study has one frontal and one lateral CXRs, associated with one radiology report. Note that images of IUX-ray were also used in the external validation of the open-ended visual question answering task.

**NIH ChestX-ray.** This dataset includes over 100,000 anonymized CXRs of more than 30,000 individuals from the NIH Clinical Center [2]. Apart from image-level pathology labels, NIH ChestX-ray also provides a small number of bounding box annotations. In practice, we incorporated the box annotations (577 boxes) of four common chest pathologies - atelectasis, cardiomegaly, effusion, and pneumothorax - into the external validation set for chest pathology detection.

**MS-CXR.** The dataset offers phrase grounding annotations that are locally aligned by board-certified radiologists, aiming to support research in the domain of complex semantic modeling for biomedical vision-language tasks [58]. Each phrase is associated with at least one bounding box annotated on one CXR. For the region captioning task, we used MS-CXR as the external validation cohort, where box coordinates were passed to the model to generate descriptive text.

## 4.2. Pipeline

As shown in Fig. 7a, MedVersa is composed of three components: the multimodal input coordinator, the large language model based optimizable orchestrator, and a variety of learnable vision modules. In practical usage, MedVersa expects inputs in the form of image-request pairs. Note that the vision

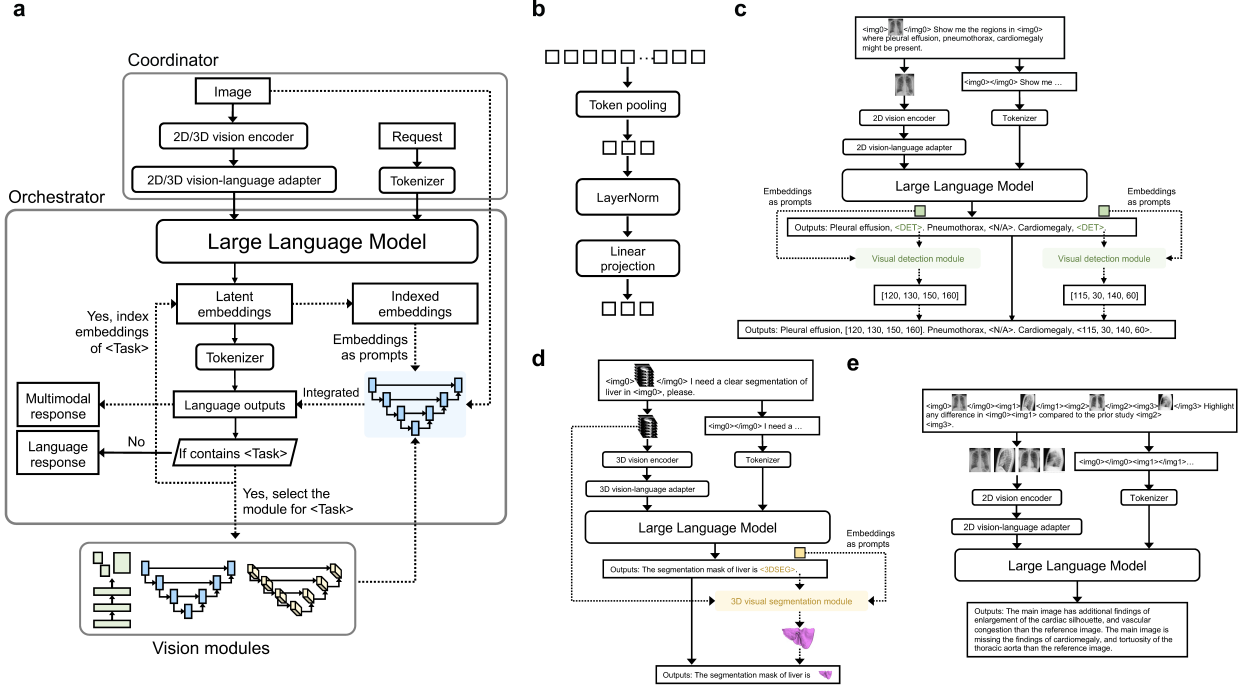


**Figure 7 | Overview of MedVersa.** **a**, Processing workflow of MedVersa. Dashed arrows indicate that the associated procedures are contingent upon the decision regarding the utilization of the vision module. Red arrows represent the operations undertaken when employing the vision module. There are three kinds of <Task> in MedVersa: <DET>, <2DSEG>, and <3DSEG>. **b**, Architecture of the vision-language adapter. **c**, Illustration of the workflow for chest pathology detection. **d**, Illustration of the workflow for abdominal organ segmentation. **e**, Illustration of the workflow for longitudinal study captioning.

input may consist of more than one image, which can be multimodal, multiview or multiperiod (see Fig. 1). MedVersa autonomously decides whether to use a 2D or a 3D vision encoder to process the vision inputs based on an analysis of the input modality. After receiving the processed inputs, the large language model can decide whether to independently perform the task or utilize a set of visual modeling modules for assistance. This dynamic decision-making process ensures that tasks are handled with the appropriate level of expertise and efficiency.

#### 4.3. MedVersa, an orchestrated GMAI system

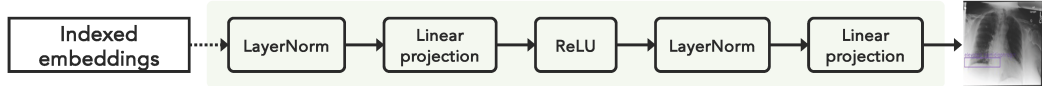
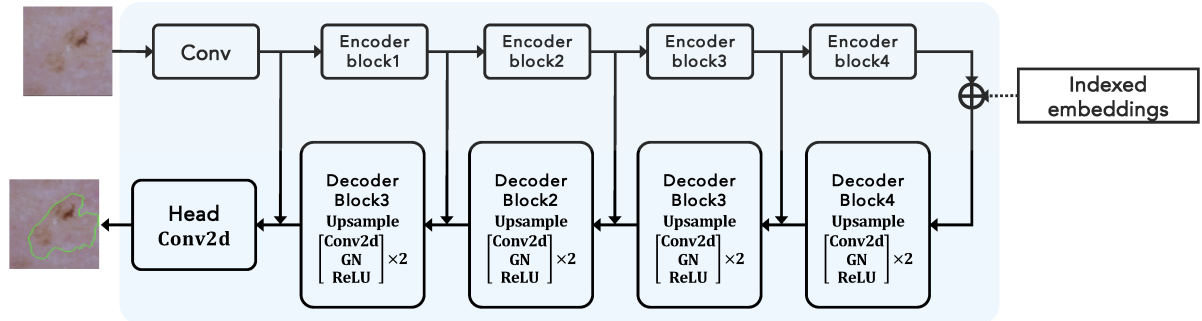
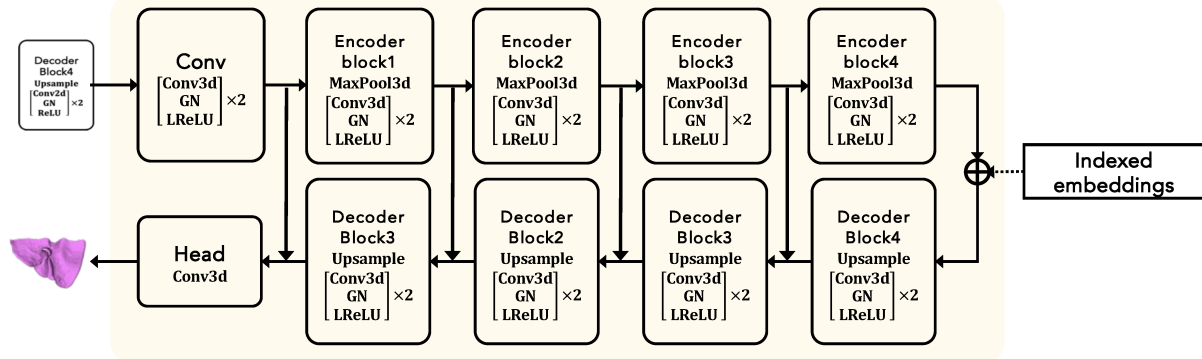
**Multimodal input coordinator.** As Fig. 7a displays, the multimodal input coordinator comprises the general vision encoders, the vision-language adapters, and the tokenizer. We design this architecture by taking inspirations from MiniGPT-4 [59, 60], LLaVA-Med [61], and Med-PaLM M [14] but keep the architecture easy for implementation. The general vision encoders are the primary gate for vision inputs. Specifically, we exploit distinct encoders for 2D and 3D imaging data, respectively. The 2D vision encoder utilizes the transformer architecture [62] to extract visual tokens from the images. For the 3D encoder, we refer to the encoder from the 3D UNet [63]. The extracted visual tokens are concatenated and passed to the adapter to get mapped to the language space. Here, we present an efficient design of the vision-language adapter, which only contains a stack of three layers (see Fig. 7b). The first layer is responsible for reducing the number of visual tokens to control the GPU memory cost, which can be achieved with an adaptive pooling function [64]. Next, the layer normalization

[65] is applied to the pooled visual tokens, followed by a linear projection layer to map the visual representations to the language space. To align with the 2D and 3D vision encoders, we also employ two independent adapters to process the extracted visual tokens accordingly. Meanwhile, the paired request is processed with the Llama tokenizer [66], which is a byte-pair encoding model based on sentencepiece [67]. The request is transformed into a series of textual tokens, which are then contextualized by the following large language model along with the mapped visual tokens. This enables the system to understand and correlate the visual data with the relevant requests.

**Orchestrated modeling.** Unlike prior research that depended exclusively on large language models (LLMs) for task execution, MedVersa leverages the planning capabilities of the large language model to act as an optimizable orchestrator of system operations. Specifically, the orchestrator has to decide whether to carry out the task independently or use a specific vision module for support based on the analysis of visual and linguistic data. This decision-making process can be formulated as:  $llm_{\theta}(I, T) \rightarrow (llm_o, s_{ok})$ .  $I$  and  $T$  denote the extracted visual and textual tokens, respectively.  $llm$  stands for the large language model.  $llm_o$  and  $s_{ok}$  represent the outputs of the language model and the  $k$ th vision module, respectively. For vision-language tasks, MedVersa only adopts the  $llm_o$  as the final language response. For vision-centric tasks, the choice of  $k$  is determined based on the  $llm_o$ . Specifically, the  $llm$  determines the task type and generates the relevant  $\langle Task \rangle$  in the  $llm_o$ . There are three kinds of  $\langle Task \rangle$  included in MedVersa:  $\langle DET \rangle$ ,  $\langle 2DSEG \rangle$ , and  $\langle 3DSEG \rangle$ . The predicted  $\langle Task \rangle$  guides the system in selecting the  $k$ th visual modeling module from the pool, tailored for executing the task described by  $\langle Task \rangle$  (see Fig. 7a for more details). Meanwhile, we index the corresponding latent embeddings of  $\langle Task \rangle$  from the output logits of the  $llm$ . These embeddings gather the information from the input data and help prompt the visual modeling module to complete the desired task. To accomplish this, the indexed latent embeddings can be either passed directly to the visual detection module or integrated with the intermediate features of the visual segmentation modules. We illustrate the orchestration process on three tasks in Fig. 7, including the chest pathology detection (Fig. 7c), the abdominal organ segmentation (Fig. 7d), and the longitudinal study captioning (Fig. 7e).

**Vision modules.** In MedVersa, we have incorporated three modules designed for vision-focused tasks, and these can be readily expanded or replaced if additional or new dedicated modules become necessary. As shown in Fig. 8a, we develop a lightweight visual detection module that can be integrated with the orchestrator. For the visual segmentation modules, we employ 2D [36] and 3D UNets [63] for 2D and 3D image segmentation tasks, respectively (Fig. 8b and 8c). We initialize the encoder of the 2D UNet using the pretrained weights of ResNet-18 [68] on ImageNet [69]. We have attempted several different approaches to incorporate the indexed embeddings from the large language model into the vision modules. Our observation is that the feature concatenation or addition outperforms the more complex operation, such as cross attention [70]. Based on this, we add the indexed embeddings to the intermediate feature maps in segmentation modules, while feeding these embeddings to the detection module directly. Note that all dedicated modules are optimizable and need to be trained with the other parts of MedVersa.

**Model training and testing with meticulous, referring image instructions.** The success of Alpaca, along with recent advancements in large language models [71–74], have underscored the importance of incorporating diverse instructions to consolidate multiple tasks and enhance generalization capabilities during supervised fine-tuning. This compelling evidence prompted us to embrace this concept within MedVersa. We propose referring image instruction tuning, where image identifiers are added to instructions to specify different images. This technique enhances the model’s capability to perform complex comparative analyses, such as the longitudinal study captioning, where we need to assign images to different studies and compare studies instead of images.

**a****Visual detection module****b****2D visual segmentation module****c****3D visual segmentation module**

**Figure 8 | Vision modules.** **a**, Visual detection module. The architecture consists of a sequential neural network that starts with a LayerNorm applied to the hidden size of 4096. This is followed by a linear layer that reduces the dimensionality from 4096 to 256, then a ReLU activation for non-linearity. Another LayerNorm is applied to the 256-dimensional output, followed by a final linear layer that reduces the dimensionality further to 4. **b**, 2D visual segmentation module. The encoder in this module is built on the ResNet-18 architecture with ImageNet-pretrained weights, while the decoder follows the structure of a UNet decoder. Specifically, we replaced batch normalization layers with group normalization, where we set the number of groups to 16. **c**, 3D visual segmentation module. In this module, we adopted the UNet3D architecture. Conv2d and Conv3d stand for the 2D and 3D convolution, respectively. GN denotes the group normalization layer, and LReLU represents the leaky ReLU activation function. We initialized the encoder of the specialist module for 2D segmentation using the pretrained weights of ResNet-18 on ImageNet. The red arrows denote the skip connections.

For example, in Fig. 7e, the exact input to MedVersa for longitudinal study captioning is like: ‘<img0> $v_0$ </img0><img1> $v_1$ </img1><img2> $v_2$ </img2><img3> $v_3$ </img3>’ Highlight any difference in <img0><img1> compared to the prior study <img2><img3>.’  $v_i$  stands for the visual tokens of the  $i$ th input image. We showcase all instructions used in the model training in Table 5. For each task in our study, we asked ChatGPT to generate a maximum of 20 prompts, each adhering to a predefined template. This template consists of the initial instruction for each task, providing a structured starting point for the prompts. After this, we conducted a manual review, carefully sifting through the generated prompts to eliminate any that were similar in nature, ensuring that we retained only the most diverse and distinct prompts for our analysis. During the training and test phases, for a given sample corresponding to a specific task, we choose an instruction at random from the set of instructions linked to the task. Here, we outline the method for creating ground truth labels for various tasks and samples. For vision-language tasks, natural language answers are directly utilized as the target for training the model. In particular, for classification tasks, the model is instructed to produce the names of diagnoses. When dealing with vision-centric tasks, we employ distinct labeling techniques for detection and segmentation. In detection tasks, during each training iteration, we initially select up to nine classes at random and convey their names (together with a randomly chosen instruction) to the model. The model is trained to append either <N/A> or <DET> tags following each class name. <N/A> indicates the absence of the corresponding class in the input image, whereas <DET> signifies its presence. Subsequently, we identify the latent embeddings of <DET> tags and use them in the visual detection module for determining bounding box coordinates. For segmentation tasks, a single class name is randomly chosen from the set, and this name, along with the instruction, is fed into the model. The model is then trained to generate either ‘The segmentation mask of [class name] is <2DSEG>’ or ‘The segmentation mask of [class name] is <3DSEG>,’ depending on whether the task is 2D or 3D segmentation. A similar idea was also adopted in natural image processing [75]. As in detection, the relevant embeddings for <2DSEG> or <3DSEG> are then passed to the appropriate 2D or 3D visual segmentation modules to create the segmentation masks.

**Domain-aware minibatch gradient descent for multimodal multitask training.** Unlike current medical FMs [13–15, 17] that only probed the vision-language capability, MedVersa needs to be trained on both vision-language and vision-centric tasks, which brings challenges to classic minibatch gradient descent optimization [76]. To solve this, we introduce a method called domain-aware minibatch gradient descent. The main idea is to create minibatches using training samples that all come from the same task and imaging type. We first divide the training data into seven groups based on their tasks: image captioning, classification, detection, segmentation, VQA, region captioning, and longitudinal study captioning. After that, we create minibatches for each group by randomly selecting samples that match the same imaging type. This means that each minibatch will have data focused on one specific task and one type of imaging. For example, one minibatch might include only samples for the segmentation task on CT scans, while another might contain only samples for the detection task on CXRs. During each training iteration, we start by randomly picking an imaging type. Then, we select a task associated with this imaging type and randomly sample data for that task. We apply gradient descent separately to each minibatch, allowing the model to better learn and improve its performance for each specific task and imaging type. We also use different loss functions tailored to each task. For example, cross-entropy loss is used for vision-language tasks, while a mix of cross-entropy and regression losses is used for detection. For the segmentation task, we use both focal loss and DICE loss, giving them equal importance.

**Radiologist evaluation.** A structured radiologist evaluation was conducted using a private instance of Argilla (version 1.29). Radiologists reviewed pairs of reports (one AI-generated by MedVersa, one human-generated) alongside corresponding images and clinical information. Reports were randomly shuffled and labeled as “Report A” and “Report B” for blind evaluation. Radiologists judged whether

Report A was better, Report B was better, or both were clinically equivalent. Studies for evaluation were randomly sampled from the test set of MIMIC-CXR.

**User study.** We conducted a reader study to evaluate artificial intelligence assistance in chest radiograph reporting, recruiting ten board-certified radiologists through a specialized medical image annotation company in India. The study utilized randomly selected chest radiographs from the MIMIC-CXR dataset. We developed a custom evaluation platform that integrated several key components: a DICOM viewer for image interpretation, a worklist interface for case management, and a report editing interface where radiologists could modify and finalize their reports. Upon report completion, the platform automatically prompted radiologists to rate their confidence level and the mental demand required for the case using Likert scales. The platform’s integrated timer tracked time spent on each case. The preparation phase included providing participants with a detailed study task protocol and an instructional video, completing a standardized training phase of 25 cases to ensure platform familiarity, and conducting an interactive orientation meeting where we demonstrated platform functionality, reviewed task requirements, and addressed any remaining questions about the study procedures.

For the main evaluation, each radiologist interpreted 75 unique chest radiographs under three different reporting scenarios: (1) starting with a standard negative template, (2) starting with a GPT-4o-generated report draft, or (3) starting with a MedVersa-generated report draft. Cases were randomly and evenly distributed across these three scenarios, with each radiologist reading 25 cases per scenario. For each case, radiologists were tasked with reviewing the chest radiograph and modifying the provided template or draft to produce a clinically accurate final report that would meet the standards of clinical practice. To eliminate potential recall bias and need for washout periods, each radiologist interpreted a case only once, while the same case was interpreted under different scenarios across different radiologists, ensuring balanced distribution of case complexity.

We evaluated three key dimensions of reporting performance: efficiency, radiologist experience, and clinical consistency. Reporting efficiency was measured through the platform’s integrated timer. Radiologist experience was assessed through self-reported confidence levels and mental demand ratings collected immediately after each report completion. For clinical consistency, we compared the “findings” section of each final report against those of the other nine radiologists for the same case, using an adapted version of FineRadScore (using GPT-4o) [31]. We calculated the average number of urgent or emergent discrepancies based on FineRadScore clinical severity categories.

#### 4.4. Implementation details

For the 2D vision encoder in the multimodal input coordinator, we use the base version of Swin Transformer [77] pretrained on ImageNet [69]. This encoder is characterized by its four-stage structure, a window size of seven, a patch size of four, and an initial feature dimension of 128. For the 3D vision encoder, we adopt the encoder architecture from the 3D UNet [63]. For specific tasks like report generation, classification, open-ended VQA, and longitudinal study captioning, the encoder processes the input images through a random cropping technique, where the cropped area ranges from 50% to 100% of the original image. These cropped images are then resized to a standard dimension of 224×224 pixels with three channels. Different augmentation techniques are applied based on the nature of the task. For chest organ and skin lesion segmentation tasks, a random horizontal flip is applied to each image. In the case of abdomen CT scans, a more complex manipulation is performed by flipping each 3D volume over a random axis. To efficiently manage the volume of visual tokens, MedVersa utilizes an adaptive average pooling strategy, standardizing the output length to nine. Additionally, the system implements two distinct linear projectors for 2D and 3D data. Each projector

comprises a fully connected layer, transforming each pooled visual token into a 1D vector of 4,096 elements.

We initialized the LLM-based orchestrator using the model weights of Llama-2-Chat [66]. The training of the orchestrator in MedVersa employs the Low-Rank Adaptation (LoRA) strategy [78] as we found that it outperformed full-parameter training. LoRA utilizes the concept of low-rank matrix decomposition to approximate a large weight matrix in neural network layers. By setting the rank and alpha values of LoRA to 16, the method ensures efficient training while modifying only a fraction of the model parameters. The AdamW optimizer [79], in combination with a cosine learning rate scheduler, is used for optimization. Training parameters are meticulously set, with an initial learning rate of 3e-4 and a minimum of 3e-6, over 500,000 training iterations. The first 3,000 iterations involve a linear warm-up phase, starting with a learning rate of 1e-7. Finally, the training infrastructure comprises 24 NVIDIA A100 GPUs (80G). This setup allows the training stage to be completed within a 72-hour window. Following this round of training, we extended MedVersa’s segmentation functionality by further finetuning the model on additional images and masks. Specifically, we froze the language model and focused on finetuning the segmentation vision module. In this phase, we applied random horizontal flip as the primary data augmentation strategy. We used an initial learning rate of 1e-4 and finetuned the model for 300 epochs, with an input image size of 224×224.

We use F1 score instead of AUC (Area Under the Curve) for evaluating classification tasks because F1 score better captures the model’s performance on both recall and precision. In contrast, AUC summarizes performance across all possible thresholds for classifying an instance as positive. It doesn’t emphasize the model’s performance at the high-precision, high-recall region. In disease classification tasks, it is crucial to have a high F1 score because false negatives (failing to identify a patient with the disease) and false positives (incorrectly diagnosing a healthy patient with the disease) can both have serious consequences. Therefore, the F1 score is used in our experiments as it balances both precision and recall, ensuring that the model correctly identifies a high proportion of true disease cases while minimizing misdiagnoses. In practice, we found a default threshold 0.5 is sufficient. Considering the robustness and generalization to new, unseen data, we use this threshold when computing precision and recall scores.

#### 4.5. Baselines

1. **ClsGen.** This is a differentiable end-to-end method with three parts: a classifier, a generator, and an interpreter [28]. The classifier learns disease features through context modeling and a disease-state aware mechanism. The generator turns the disease information into a medical report. The interpreter then reviews and refines these reports, ensuring they align with the classifier’s findings. We empirically found ClsGen showed more consistent performance compared to popular report generation approaches, such as R2Gen [80] and M2Trans [81]. We trained the model for 50 epochs, with a batch size of 64. The initial learning rate is set to 3e-4 and adjusted to 3e-5 at the 25th epoch. The weight decay is set to 1e-2. The input image size is 336×336, and we only applied random cropping as we did in MedVersa as the main augmentation strategy for report generation. For all other settings we adhered to the original paper [28].
2. **DAM.** This method is particularly relevant for addressing complex classification problems, especially when dealing with imbalanced datasets [33]. We included the DAM supervised method as a baseline for chest pathology classification, which currently is state-of-the-art on the CheXpert dataset [5]. Following the training protocol on CheXpert, we initially trained the DenseNet-121 model [82], pretrained on ImageNet, for one epoch using a batch size of 32, a learning rate of 1e-4, and a weight decay of 1e-5. Subsequently, we finetuned the model for two additional epochs, maintaining the same batch size and weight decay, but with an increased

learning rate of 0.01. The input image size is 224×224. For other settings, we followed the official tutorial.

3. **MAIRA.** This is a specialist large multimodal model for report generation from Microsoft [21]. It adopted the LLaVA-1.5 architecture [83]. MAIRA also benefits from the use of GPT-3.5 for data augmentation, adding 131,558 reports with paraphrased findings and indication sections to the training set. MAIRA produces reports with state-of-the-art quality.
4. **Med-PaLM M.** This is a large generalist biomedical AI system from Google [14]. Med-PaLM M was built by finetuning with biomedical data on top of PaLM-E [84], a generalist multimodal FM trained on non-medical images and text. Here, we compared to its best variant that has 84 billion parameters, which maintains the state-of-the-art in the task of report generation.
5. **PTLM.** It is the state-of-the-art approach on open-ended medical visual question answering [39]. PTLM maps the extracted visual features to a set of learnable tokens, which can directly prompt the language model for parameter-efficient finetuning. We utilized 600 warmup steps with a learning rate of 5e-3 and a cosine learning rate scheduler. The model was trained for 30 epochs with a batch size of 64. The input image size is 224×224. For all other configurations, we followed the settings from the official repository.
6. **EKAID.** EKAID integrates the expert knowledge graphs into representation learning [51]. This is an image-difference model that is sensitive to anatomical structures, allowing it to extract image-difference features that are pertinent to the progression of diseases and interventions. EKAID presents state-of-the-art results in the task of longitudinal study captioning. For implementation, we used a learning rate of 0.01 to train the model for 20 epochs at a batch size of 128. The input image size is 224×224, and random cropping is applied to each input image.
7. **MiniGPT.** This is a new multimodal foundation model that can caption bounding boxes on natural images [60]. Specifically, it accepts box coordinates as inputs and outputs a caption that describes the objects within the box. We therefore finetuned MiniGPT on the region captioning task. We used a cosine learning rate scheduler to train the model with a batch size of 16 and a maximum learning rate of 3e-4. The input image size is 224×224, with random cropping applied to each image.
8. **CRCKD.** This approach aims to bring similar image pairs from the same skin class closer together in both teacher and student models while pushing apart dissimilar image pairs from different skin classes [35]. It is a widely adopted baseline and shows competitive performance for categorizing skin lesions. Note that both CRCKD and MedVersa were trained directly on the raw, imbalanced HAM10000 dataset. The input image size is 224×224. We trained the model for 80 epochs with the batch size and the warm-up epoch set as 64 and 30, respectively. The initial learning rate was set to 1e-4 and decayed by the one-cycle schedule. The temperature is set as 0.07. For other settings, we followed the official code repository.
9. **YOLO.** YOLO is a state-of-the-art, real-time object detection algorithm that is part of the YOLO (You Only Look Once) family [22]. Following its predecessors in providing fast and accurate object detection capabilities, YOLO has been widely used for detecting abnormalities in medical images [85–87]. We trained the model for 100 epochs with an input image size of 224×224. The batch size is 64, and the initial learning rate is 0.01. We set the weight decay to 5e-4 and used the default mosaic augmentation.
10. **nnUNet.** nnUNet is a self-configuring method for deep learning-based biomedical image segmentation [36]. This framework is versatile in handling various medical imaging datasets, employing different configurations and preprocessing steps depending on the dataset characteristics. It adapts the network topologies, such as 2D UNet and 3D UNet, according to the specific requirements of medical segmentation tasks. We adopted nnUNET’s automatically configured networks on the datasets as baseline models for 2D and 3D segmentation. During training, we trained the 2D model for 300 epochs and the 3D model for 500 epochs. The batch size is set as

16. The input size of 2D images is 224×224, while for 3D images it is adjusted to 192×192×64. The initial learning rate is 1e-3 with a polynomial decay scheduler. Extensive data augmentation was applied, including rotation, scaling, elastic deformations, and intensity augmentations.
11. **nnSAM**. The nnSAM architecture integrates the robust and effective feature extraction abilities of Segment Anything Model [38] with the adaptive configuration strengths of nnUNet [37]. This combination maximizes the potential of each model, with SAM providing high-quality feature extraction and nnUNet enabling the system to automatically adjust to the unique demands of each dataset. nnSAM shows state-of-the-art results in the data-efficient segmentation task. In line with the official code repository, we employed the same training parameters and strategies used by nnUNet.
12. **BiomedGPT**. BiomedGPT [29] is a generalist vision-language foundation model for biomedical tasks. We utilized the pretrained weights of BiomedGPT and fine-tuned the model on each task individually, following the protocol outlined in the original paper. For fine-tuning, we employed the AdamW optimizer with an initial learning rate of 3e-4, along with a cosine learning rate scheduler. The weight decay was set to 1e-5, and the training process lasted for 30 epochs. The input image size is 256×256.
13. **MedViT**. MedViT [34] is a CNN-Transformer hybrid model designed for robust and efficient medical image classification. In practice, we used the large version of MedViT. We trained MedViT-L for 100 epochs with a batch size of 128. The input images were resized to 224×224 pixels. We used the AdamW optimizer with an initial learning rate of 0.001, which was decayed by a factor of 0.1 at the 50th and 75th epochs.
14. **3D TransUNet**. 3D TransUNet [88] is an extension of the 2D TransUNet architecture to 3D medical image segmentation. We fixed the input size to 192×192×64, as what we have done to MedVersa, nnUNet, and nnSAM. We used the AdamW optimizer with an initial learning rate of 1e-4 with a cosine learning rate scheduler. The augmentation strategies include random rotation, scaling, flipping, white Gaussian noise, Gaussian blurring, adjusting brightness and contrast, simulation of low resolution, and Gamma transformation.

#### 4.6. Confidence intervals

For the estimation of 95% confidence intervals, non-parametric bootstrap sampling is utilized. This process includes creating 1,000 bootstrap samples from the unseen validation set through random sampling with replacement, with each sample having the same size as the validation set. We then compute the evaluation metric scores for each of these samples. Upon gathering 1,000 scores for the metrics, we organize these scores sequentially. The performance metrics at the 2.5th and 97.5th percentiles are identified and presented as the performance indicators.

#### Data availability

All training and validation data is publicly available, links of which are provided in Table 4.

#### Code availability

Code and models can be accessed via <https://tinyurl.com/fhnv3be4> (passwd: HYZ0214).

#### Author contributions

P.R. and H.-Y.Z. conceived the study. H.-Y.Z. planned and executed the experiments and data analysis. S.A. and S.D. interpreted medical report generation results. J.N.A. designed and executed the user

study, and analyzed its results. H.-Y.Z. and P.R. drafted the manuscript. All authors provided critical feedback and substantially contributed to the revision of the manuscript. All authors read and approved the manuscript.

#### **Competing interests**

P.R. is co-founder of a2z Radiology AI. J.N.A is a part-time employee of a2z Radiology AI. Other authors declare no competing interests.

**Table 4 | Overview of MedInterp.** All datasets included in MedInterp are publicly available. We reported the dataset size after preprocessing. For each dataset, we also denoted the associated task(s) and the stage(s) involved. VQA denotes visual question answering. 1, 2, 3 in the stages column stand for the training, internal validation, and external validation stages, respectively. We followed the guideline in SAM-Med to preprocess the segmentation data [47].

Datasets	Size	Imaging modalities	Tasks	Stages
MIMIC-CXR [4, 48]	216,420 studies	Chest X-ray	Image captioning	1, 2
	235,721 images	Chest X-ray	Image classification	1, 2
Chest ImaGenome [50]	8,425,163 boxes	Chest X-ray	Object detection (anatomical structure)	1, 2
	2,922,665 boxes	Chest X-ray	Object detection (pathology)	1, 2
	2,104,211 captions	Chest X-ray	Region captioning	1, 2
	383,683 QA pairs	Chest X-ray	Open-ended VQA	1, 2
Medical-DiffVQA [51]	147,269 comparisons	Chest X-ray	Longitudinal captioning	1, 2
	2,883 QA pairs	Chest X-ray	Open-ended VQA	3
PMC-VQA [52]	176,946 QA pairs	Mixed	VQA	1
PathVQA [53]	32,795 QA pairs	Histopathology	VQA	1, 2
VQA-RAD [54]	451 QA pairs	Chest X-ray, CT, MRI	VQA	3
HAM10000 [55]	11,526 images	Dermoscopy	Image classification	1, 2
	10,015 masks	Dermoscopy	2D image segmentation	1, 2
CheXpert [3]	668 images	Chest X-ray	Image classification	3
IUX-ray [30]	3,323 studies	Chest X-ray	Image captioning	3
NIH ChestX-ray [2]	577 boxes	Chest X-ray	Object detection	3
MS-CXR [58]	1,448 captions	Chest X-ray	Region captioning	3
AbdomenCT-1K [89]	3,964 masks	CT	3D image segmentation	1, 2
	719,793 masks	Chest X-ray	2D image segmentation	1, 2
CheXmask [90]	600 masks	Chest X-ray	2D image segmentation	2
ACDC [91]	4,976 masks	MR	2D image segmentation	1, 2
AMOS2022 [92]	217,383 masks	CT, MR	2D image segmentation	1, 2
ASC18 [93]	8,855 masks	MR	2D image segmentation	1, 2
ATM2022 [94]	41,604 masks	CT	2D image segmentation	1, 2
AbdomenCT1K [95]	217,155 masks	CT	2D image segmentation	1, 2
BTCV [96]	10,243 masks	CT	2D image segmentation	1, 2
BTCV_Cervix [96]	4,667 masks	CT	2D image segmentation	1, 2
BraTS2013 [97, 98]	118,496 masks	MR	2D image segmentation	1, 2
BraTS2015 [97, 98]	615,336 masks	MR	2D image segmentation	1, 2
BraTS2018 [97, 99, 100]	537,300 masks	MR	2D image segmentation	1, 2
BraTS2019 [97, 99, 100]	629,196 masks	MR	2D image segmentation	1, 2
BraTS2020 [97, 99, 100]	699,956 masks	MR	2D image segmentation	1, 2
BraTS2021 [97, 99, 100]	1,255,832 masks	MR	2D image segmentation	1, 2
BrainTumour [101]	991,171 masks	MR	2D image segmentation	1, 2
Brain_PT [102, 103]	12,698 masks	MR	2D image segmentation	1, 2
CAD_PE [104]	8,307 masks	CT	2D image segmentation	1, 2
CHAOS_Task_4 [105]	3,513 masks	MR	2D image segmentation	1, 2
CMRxMotions [106]	3,312 masks	MR	2D image segmentation	1, 2
COSMOS2022 [107]	2,530 masks	MR	2D image segmentation	1, 2
COVID-19-20 [108]	7,321 masks	CT	2D image segmentation	1, 2
COVID19CTscans [89]	18,880 masks	CT	2D image segmentation	1, 2
CTPelvic1k [109]	551,693 masks	CT	2D image segmentation	1, 2
CTSpine1k_Full [110]	419,191 masks	CT	2D image segmentation	1, 2
CT_ORG [111]	599,292 masks	CT	2D image segmentation	1, 2
CrossMoDA21 [112]	739 masks	MR	2D image segmentation	1, 2
CrossMoDA22 [113]	1,478 masks	MR	2D image segmentation	1, 2
EMIDEC [114]	1,694 masks	MR	2D image segmentation	1, 2
FLARE21 [115]	129,239 masks	CT	2D image segmentation	1, 2
FLARE22 [116]	23,368 masks	CT	2D image segmentation	1, 2
Heart_Seg_MRI [117]	517 masks	MR	2D image segmentation	1, 2
ISLES2016 [118]	1,506 masks	MR	2D image segmentation	1, 2
ISLES2017 [118]	2,022 masks	MR	2D image segmentation	1, 2
ISLES2018 [119, 120]	1,635 masks	CT	2D image segmentation	1, 2
ISLES2022 [121]	13,572 masks	MR	2D image segmentation	1, 2
ISLES_SISSL [122]	15,648 masks	MR	2D image segmentation	1, 2
ISLES_SPES [122]	24,066 masks	MR	2D image segmentation	1, 2
Instance22 [123, 124]	920 masks	CT	2D image segmentation	1, 2
KitS2019 [125]	54,726 masks	CT	2D image segmentation	1, 2
KitS2021 [126]	80,540 masks	CT	2D image segmentation	1, 2
LNDb [127]	1,010 masks	CT	2D image segmentation	1, 2
LUNA16 [128]	367,732 masks	CT	2D image segmentation	1, 2
LongitudinalMultipleSclerosisLesionSegmentation [129]	13,372 masks	MR	2D image segmentation	1, 2
MMWHS [24, 130, 131]	42,682 masks	CT	2D image segmentation	1, 2

MSD_Colon [107]	1,197 masks	CT	2D image segmentation	1, 2
MSD_Heart [107]	1,101 masks	MR	2D image segmentation	1, 2
MSD_HepaticVes [107]	6,576 masks	CT	2D image segmentation	1, 2
MSD_Liver [107]	82,784 masks	CT	2D image segmentation	1, 2
MSD_Lung [107]	2,347 masks	CT	2D image segmentation	1, 2
MSD_Pancreas [107]	10,349 masks	CT	2D image segmentation	1, 2
MSD_Prostate [107]	1,466 masks	MR	2D image segmentation	1, 2
MSD_Spleen [107]	1,008 masks	CT	2D image segmentation	1, 2
PALM19 [132]	1,144 masks	Fundus	2D image segmentation	1, 2
PROMISE12 [133]	776 masks	MR	2D image segmentation	1, 2
Parse22 [131]	48,225 masks	CT	2D image segmentation	1, 2
Promise09 [134]	148 masks	MR	2D image segmentation	1, 2
Prostate_MRI_Segmentation_Dataset [135]	1,865 masks	MR	2D image segmentation	1, 2
StructSeg2019_subtask1 [107]	3,673 masks	CT	2D image segmentation	1, 2
StructSeg2019_subtask2 [107]	4,772 masks	CT	2D image segmentation	1, 2
Totalsegmentator_dataset [136]	5,520,406 masks	CT	2D image segmentation	1, 2
VESSEL2012 [137]	33,784 masks	CT	2D image segmentation	1, 2
VerSe19 [138]	208,016 masks	CT	2D image segmentation	1, 2
VerSe20 [138]	314,067 masks	CT	2D image segmentation	1, 2
WORD [139]	87,346 masks	CT	2D image segmentation	1, 2
autoPET [140]	14,457 masks	CT	2D image segmentation	1, 2
brainMRI [107]	1,441 masks	MR	2D image segmentation	1, 2
Breast_ultrasound_images_dataset [141]	645 masks	Ultrasound	2D image segmentation	1, 2
Cranium [142]	229 masks	CT	2D image segmentation	1, 2
cvc_clinicdb [143]	645 masks	Endoscopy	2D image segmentation	1, 2
Endovis15 [144]	645 masks	Endoscopy	2D image segmentation	1, 2
Gamma [145, 146]	190 masks	Fundus	2D image segmentation	1, 2
Hvsmr_2016 [147]	7,479 masks	MR	2D image segmentation	1, 2
Ichallenge_adam_task2 [148]	270 masks	Fundus	2D image segmentation	1, 2
Kvasir_seg [149]	211 masks	Endoscopy	2D image segmentation	1, 2
Kvasircapsule_seg [150]	55 masks	Endoscopy	2D image segmentation	1, 2
M&Ms-2 [151]	6,782 masks	MR	2D image segmentation	1, 2
PI-CAI [152]	451 masks	MR	2D image segmentation	1, 2
PI-CAI_semi [152]	620 masks	MR	2D image segmentation	1, 2
Ultrasound Nerve Segmentation [107]	2,323 masks	Ultrasound	2D image segmentation	1, 2

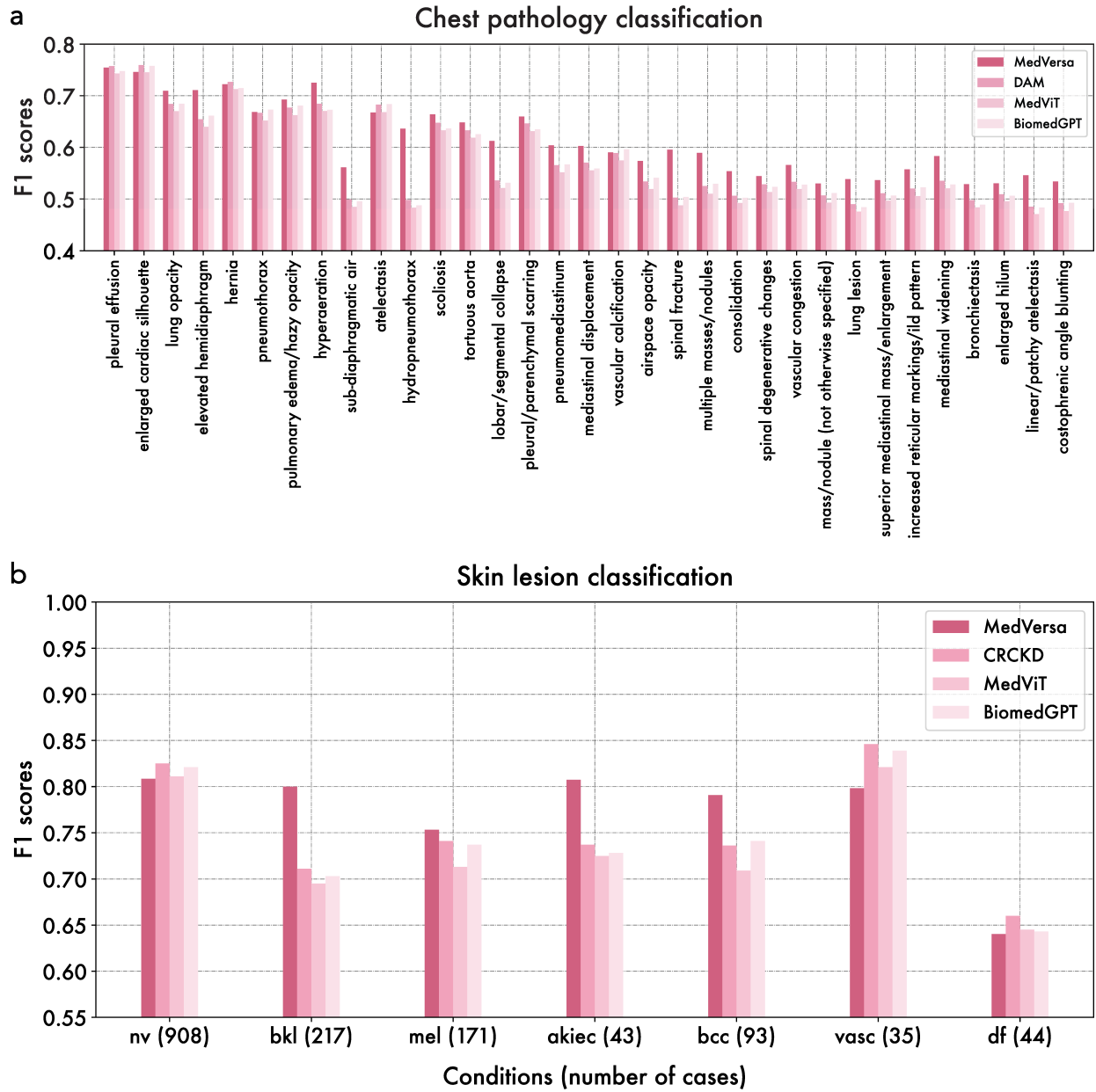


Figure 9 | Per-category results for image classification. **a**, chest pathology classification. **b**, skin lesion classification.

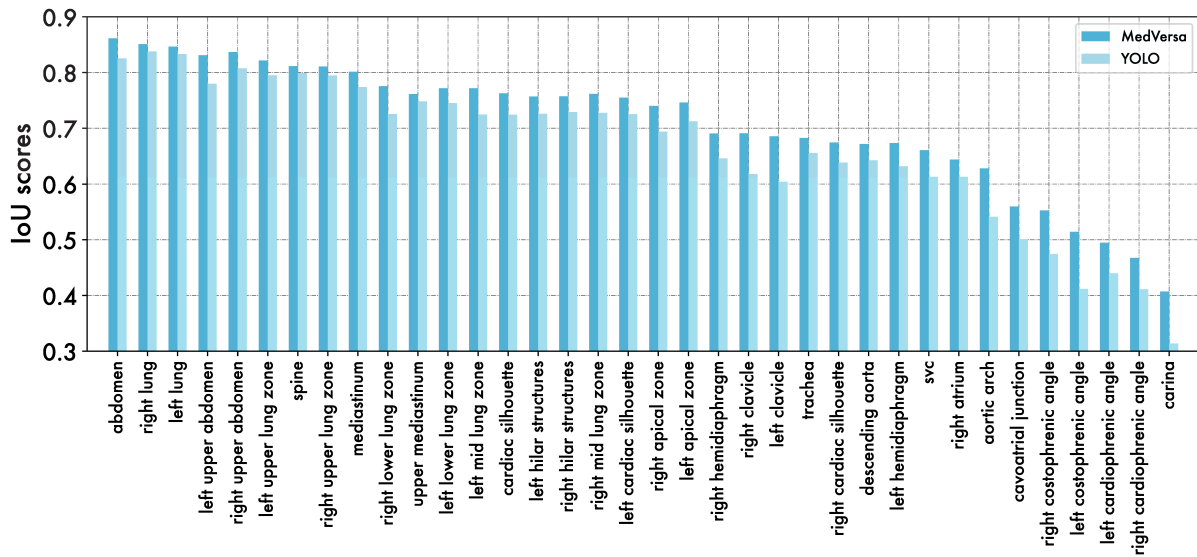
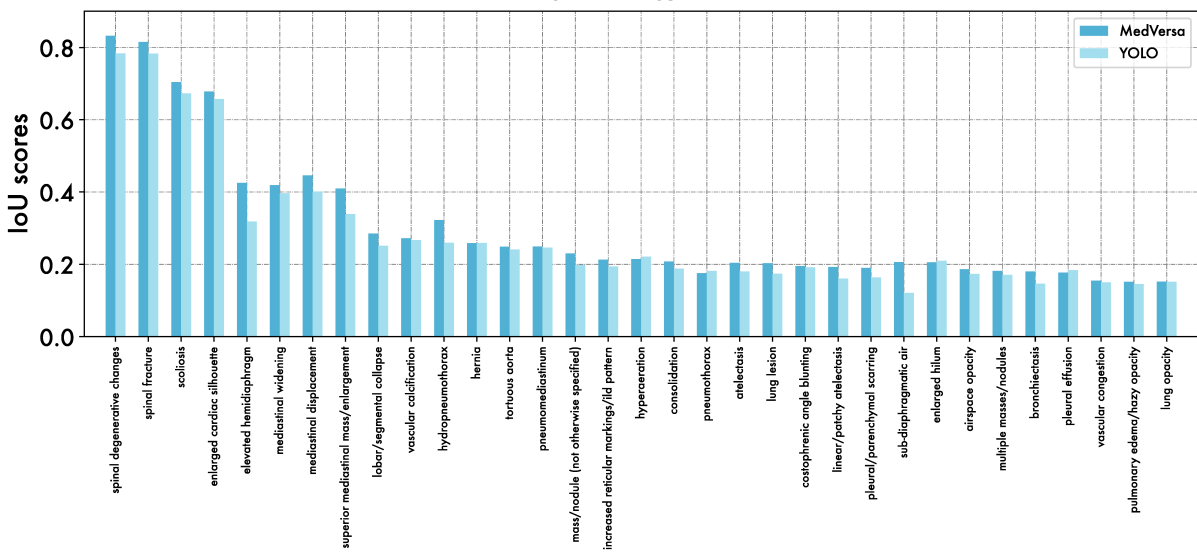
**a****Anatomical structure detection****b****Chest pathology detection**

Figure 10 | Per-category results for object detection. **a**, Anatomical structure detection. **b**, Chest pathology detection.

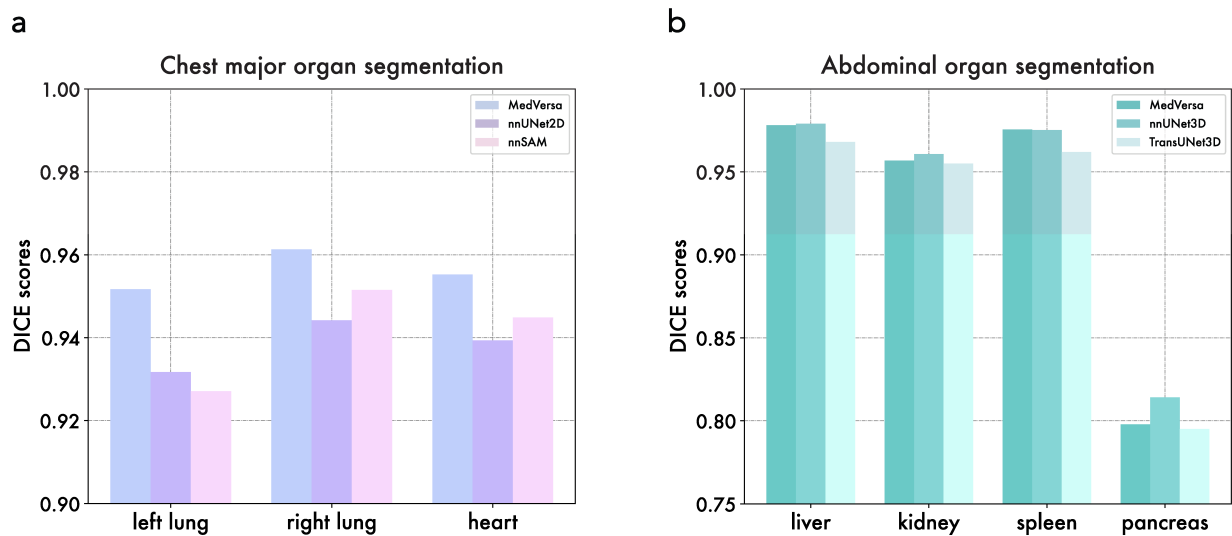


Figure 11 | **Per-category results for image segmentation.** **a**, Chest major organ segmentation (2D). **b**, Abdominal organ segmentation (3D).

**Table 5 | Instructions used by MedVersa in different tasks.**  $_{*}$  is the placeholder for the main image identifier (e.g., <img0>).  $_{*}$ - denotes the placeholder for the abnormalities, bounding box coordinates, reference image identifier, detection, and segmentation targets in binary classification, region captioning, longitudinal captioning, detection, and segmentation tasks, respectively. For each task, we asked ChatGPT to generate at most 20 prompts based on a predefined template (i.e., the first instruction for each task. Then, we manually filtered out similar prompts and kept those diverse ones.

Tasks	Instructions
Image captioning (report generation, findings section)	<ol style="list-style-type: none"> <li>1. Can you detail the findings observed in <math>_{*}</math>?</li> <li>2. Kindly enumerate the findings from <math>_{*}</math>.</li> <li>3. I'd like a breakdown of the findings from <math>_{*}</math>.</li> <li>4. I'd like a section on the findings derived from <math>_{*}</math>.</li> <li>5. Please write a finding section for <math>_{*}</math>.</li> <li>6. Would you please write a finding section for <math>_{*}</math>?</li> <li>7. Please write a section of findings for <math>_{*}</math>.</li> <li>8. Would you please write a section of findings for <math>_{*}</math>?</li> <li>9. How would you characterize the findings from <math>_{*}</math>?</li> <li>10. Please list the discernible findings from <math>_{*}</math>.</li> <li>11. Can you compile a list of all the notable findings present in <math>_{*}</math>?</li> <li>12. Please document any findings you see in <math>_{*}</math>.</li> </ol>
Image captioning (report generation, impression section)	<ol style="list-style-type: none"> <li>1. Can you please provide your overall impression of <math>_{*}</math>?</li> <li>2. What's your main impression from <math>_{*}</math>?</li> <li>3. Please draft a concise impression on <math>_{*}</math>.</li> <li>4. Would you give a comprehensive impression based on <math>_{*}</math>?</li> <li>5. I'm looking for an impression for <math>_{*}</math>.</li> <li>6. Provide your diagnostic impression based on the <math>_{*}</math>.</li> <li>7. Draft an impression for <math>_{*}</math>.</li> <li>8. Would you please write an impression section for <math>_{*}</math>?</li> <li>9. Summarize the impression for <math>_{*}</math>.</li> </ol>
Image captioning (report generation, complete report)	<ol style="list-style-type: none"> <li>1. Can you provide a radiology report for <math>_{*}</math>?</li> <li>2. Please report <math>_{*}</math>.</li> <li>3. Can you provide a report of <math>_{*}</math> with findings and impression?</li> <li>4. Report <math>_{*}</math> with findings and impression.</li> <li>5. Please write a radiology report for <math>_{*}</math>.</li> <li>6. Please generate a radiology report for <math>_{*}</math>.</li> <li>7. Please provide a detailed report for <math>_{*}</math>.</li> <li>8. Can you provide a comprehensive report of <math>_{*}</math>?</li> <li>9. Please write a radiology report for <math>_{*}</math>.</li> <li>10. Can you give a thorough report of <math>_{*}</math>?</li> <li>11. Could you please report <math>_{*}</math>?</li> <li>12. Can you provide a comprehensive report for <math>_{*}</math>?</li> </ol>
Image classification (chest pathology and skin lesion)	<ol style="list-style-type: none"> <li>1. What is the diagnosis for <math>_{*}</math>?</li> <li>2. Based on <math>_{*}</math>, what type of lung disease is suspected?</li> <li>3. Can you identify any abnormality in <math>_{*}</math>?</li> <li>4. What pathology is indicated by <math>_{*}</math>?</li> <li>5. What lung disease is likely present in <math>_{*}</math>?</li> <li>6. What are your conclusions from <math>_{*}</math>?</li> <li>7. What is your interpretation result of <math>_{*}</math>?</li> <li>8. What abnormalities are present in <math>_{*}</math>?</li> <li>9. What is the differential diagnosis for the findings in <math>_{*}</math>?</li> </ol>
Region captioning	<ol style="list-style-type: none"> <li>1. Describe region <math>_{*}</math> in <math>_{*}</math>.</li> <li>2. Detail any abnormalities in <math>_{*}</math> of <math>_{*}</math>.</li> <li>3. Can you characterize the features within <math>_{*}</math> of <math>_{*}</math>?</li> <li>4. Please provide an analysis of the anomalies seen in <math>_{*}</math> within <math>_{*}</math>.</li> <li>5. Describe any pathological findings within <math>_{*}</math> of <math>_{*}</math>.</li> <li>6. Highlight and explain any abnormalities you detect in <math>_{*}</math> of <math>_{*}</math>.</li> <li>7. Identify and describe any abnormality in <math>_{*}</math> of <math>_{*}</math>.</li> <li>8. Could you please describe the region <math>_{*}</math> in <math>_{*}</math>?</li> <li>9. Would you please describe the region <math>_{*}</math> in <math>_{*}</math>?</li> <li>10. Give a description of the region <math>_{*}</math> in <math>_{*}</math>.</li> </ol>
Longitudinal study captioning	<ol style="list-style-type: none"> <li>1. Highlight any difference in <math>_{*}</math> compared to the prior study <math>_{*}</math>.</li> <li>2. Identify any progression in <math>_{*}</math> since the last study <math>_{*}</math>.</li> <li>3. Compare the current study <math>_{*}</math> with the past one <math>_{*}</math>.</li> <li>4. Present any changes in <math>_{*}</math> since the last study <math>_{*}</math>.</li> <li>5. Detail any progression or regression in <math>_{*}</math> in comparison to the older study <math>_{*}</math>.</li> <li>6. Detect changes in <math>_{*}</math> compared to the past study <math>_{*}</math>.</li> <li>7. Compare <math>_{*}</math> with the prior study <math>_{*}</math> and tell me any difference.</li> </ol>

Object detection (anatomical structure and chest pathology)

---

1. Detect any signs of -\*- in   .
2. Highlight the areas that indicate -\*- in   .
3. Show me the regions in    where -\*- might be present.
4. Assess    and mark areas consistent with -\*- findings.
5. Locate and circle any features of -\*- in   .
6. Compare    to typical -\*- patterns and highlight any matches.
7. Detect and display potential symptoms of -\*- within   .
8. Is there any trace of -\*- in   ? Point it out.
9. Help me spot -\*- by illuminating its markers in   .
10. Search for any characteristic signs of -\*- in   .
11. Examine and underscore the presence of -\*- in   .
12. Would you please help me locate -\*- in   ?
13. Could you please help me locate -\*- in   ?
14. Please help me locate -\*- in   ?

---

Image segmentation

1. Segment -\*- in   .
2. Highlight the boundaries of -\*- in   .
3. Isolate and show only -\*- from   .
4. Can you delineate -\*- in   ?
5. Segment -\*- from the given   .
6. I need a clear segmentation of -\*- in   , please.
7. Outline the contours of -\*- in   .
8. Show a clear boundary around -\*- in   .
9. Separate -\*- from the surrounding anatomy in   .
10. Provide a segmented view of -\*- in   .
11. Please identify and segment -\*- from the rest in   .
12. Give me a clear cutout of -\*- in   .
13. Please mask everything except for -\*- in   .
14. Draw a boundary around -\*- in   .
15. Would you please help me segment -\*- in   ?
16. Could you please help me segment -\*- in   ?
17. Please help me segment -\*- in   ?

---

## References

- [1] Pranav Rajpurkar, Jeremy Irvin, Kaylie Zhu, Brandon Yang, Hershel Mehta, Tony Duan, Daisy Ding, Aarti Bagul, Curtis Langlotz, Katie Shpanskaya, Matthew P Lungren, and Andrew Y Ng. CheXNet: Radiologist-level pneumonia detection on chest X-rays with deep learning. *arXiv [cs.CV]*, November 2017.
- [2] Xiaosong Wang, Yifan Peng, Le Lu, Zhiyong Lu, Mohammadhadi Bagheri, and Ronald M Summers. ChestX-Ray8: Hospital-scale chest X-ray database and benchmarks on weakly-supervised classification and localization of common thorax diseases. In *2017 IEEE Conference on Computer Vision and Pattern Recognition (CVPR)*, pages 2097–2106. IEEE, July 2017.
- [3] Jeremy Irvin, Pranav Rajpurkar, Michael Ko, Yifan Yu, Silviana Ciurea-Ilcus, Chris Chute, Henrik Marklund, Behzad Haghgoo, Robyn Ball, Katie Shpanskaya, Jayne Seekins, David A Mong, Safwan S Halabi, Jesse K Sandberg, Ricky Jones, David B Larson, Curtis P Langlotz, Bhavik N Patel, Matthew P Lungren, and Andrew Y Ng. CheXpert: A large chest radiograph dataset with uncertainty labels and expert comparison. *AAAI*, 33(01):590–597, July 2019.
- [4] Alistair E W Johnson, Tom J Pollard, Seth J Berkowitz, Nathaniel R Greenbaum, Matthew P Lungren, Chih-Ying Deng, Roger G Mark, and Steven Horng. MIMIC-CXR, a de-identified publicly available database of chest radiographs with free-text reports. *Sci Data*, 6(1):317, December 2019.
- [5] Ekin Tiu, Ellie Talius, Pujan Patel, Curtis P Langlotz, Andrew Y Ng, and Pranav Rajpurkar. Expert-level detection of pathologies from unannotated chest X-ray images via self-supervised learning. *Nat Biomed Eng*, 6(12):1399–1406, December 2022.
- [6] Yuan Liu, Ayush Jain, Clara Eng, David H Way, Kang Lee, Peggy Bui, Kimberly Kanada, Guilherme de Oliveira Marinho, Jessica Gallegos, Sara Gabriele, Vishakha Gupta, Nalini Singh, Vivek Natarajan, Rainer Hofmann-Wellenhof, Greg S Corrado, Lily H Peng, Dale R Webster, Dennis Ai, Susan J Huang, Yun Liu, R Carter Dunn, and David Coz. A deep learning system for differential diagnosis of skin diseases. *Nat. Med.*, 26(6):900–908, June 2020.
- [7] Andre Esteva, Brett Kuprel, Roberto A Novoa, Justin Ko, Susan M Swetter, Helen M Blau, and Sebastian Thrun. Dermatologist-level classification of skin cancer with deep neural networks. *Nature*, 542(7639):115–118, February 2017.
- [8] Roxana Daneshjou, Kailas Vodrahalli, Roberto A Novoa, Melissa Jenkins, Weixin Liang, Veronica Rotemberg, Justin Ko, Susan M Swetter, Elizabeth E Bailey, Olivier Gevaert, Pritam Mukherjee, Michelle Phung, Kiana Yekrang, Bradley Fong, Rachna Sahasrabudhe, Johan A C Allerup, Utako Okata-Karigane, James Zou, and Albert S Chiou. Disparities in dermatology AI performance on a diverse, curated clinical image set. *Sci Adv*, 8(32):eabq6147, August 2022.
- [9] Geeta Joshi, Aditi Jain, Shalini Reddy Araveeti, Sabina Adhikari, Harshit Garg, and Mukund Bhandari. FDA approved artificial intelligence and machine learning (AI/ML)-enabled medical devices: An updated landscape. *bioRxiv*, December 2022.
- [10] Michael Moor, Oishi Banerjee, Zahra Shakeri Hossein Abad, Harlan M Krumholz, Jure Leskovec, Eric J Topol, and Pranav Rajpurkar. Foundation models for generalist medical artificial intelligence. *Nature*, 616(7956):259–265, April 2023.
- [11] Pranav Rajpurkar and Matthew P Lungren. The current and future state of AI interpretation of medical images. *N. Engl. J. Med.*, 388(21):1981–1990, May 2023.

[12] Rishi Bommasani, Drew A Hudson, Ehsan Adeli, Russ Altman, Simran Arora, Sydney von Arx, Michael S Bernstein, Jeannette Bohg, Antoine Bosselut, Emma Brunskill, Erik Brynjolfsson, Shyamal Buch, Dallas Card, Rodrigo Castellon, Niladri Chatterji, Annie Chen, Kathleen Creel, Jared Quincy Davis, Dora Demszky, Chris Donahue, Moussa Doumbouya, Esin Durmus, Stefano Ermon, John Etchemendy, Kawin Ethayarajh, Li Fei-Fei, Chelsea Finn, Trevor Gale, Lauren Gillespie, Karan Goel, Noah Goodman, Shelby Grossman, Neel Guha, Tatsunori Hashimoto, Peter Henderson, John Hewitt, Daniel E Ho, Jenny Hong, Kyle Hsu, Jing Huang, Thomas Icard, Saahil Jain, Dan Jurafsky, Pratyusha Kalluri, Siddharth Karamcheti, Geoff Keeling, Fereshte Khani, Omar Khattab, Pang Wei Koh, Mark Krass, Ranjay Krishna, Rohith Kuditipudi, Ananya Kumar, Faisal Ladhak, Mina Lee, Tony Lee, Jure Leskovec, Isabelle Levent, Xiang Lisa Li, Xuechen Li, Tengyu Ma, Ali Malik, Christopher D Manning, Suvir Mirchandani, Eric Mitchell, Zanele Munyikwa, Suraj Nair, Avanika Narayan, Deepak Narayanan, Ben Newman, Allen Nie, Juan Carlos Niebles, Hamed Nilforoshan, Julian Nyarko, Giray Ogut, Laurel Orr, Isabel Papadimitriou, Joon Sung Park, Chris Piech, Eva Portelance, Christopher Potts, Aditi Raghunathan, Rob Reich, Hongyu Ren, Frieda Rong, Yusuf Roohani, Camilo Ruiz, Jack Ryan, Christopher Ré, Dorsa Sadigh, Shiori Sagawa, Keshav Santhanam, Andy Shih, Krishnan Srinivasan, Alex Tamkin, Rohan Taori, Armin W Thomas, Florian Tramèr, Rose E Wang, William Wang, Bohan Wu, Jiajun Wu, Yuhuai Wu, Sang Michael Xie, Michihiro Yasunaga, Jiaxuan You, Matei Zaharia, Michael Zhang, Tianyi Zhang, Xikun Zhang, Yuhui Zhang, Lucia Zheng, Kaitlyn Zhou, and Percy Liang. On the opportunities and risks of foundation models. *arXiv [cs.LG]*, August 2021.

[13] Michael Moor, Qian Huang, Shirley Wu, Michihiro Yasunaga, Cyril Zakka, Yash Dalmia, Eduardo Pontes Reis, Pranav Rajpurkar, and Jure Leskovec. Med-flamingo: a multimodal medical few-shot learner. *arXiv [cs.CV]*, July 2023.

[14] Tao Tu, Shekoofeh Azizi, Danny Driess, Mike Schaeckermann, Mohamed Amin, Pi-Chuan Chang, Andrew Carroll, Chuck Lau, Ryutaro Tanno, Ira Ktena, Basil Mustafa, Aakanksha Chowdhery, Yun Liu, Simon Kornblith, David Fleet, Philip Mansfield, Sushant Prakash, Renee Wong, Sunny Virmani, Christopher Semturs, S Sara Mahdavi, Bradley Green, Ewa Dominowska, Blaise Aguera y Arcas, Joelle Barral, Dale Webster, Greg S Corrado, Yossi Matias, Karan Singhal, Pete Florence, Alan Karthikesalingam, and Vivek Natarajan. Towards generalist biomedical AI. *arXiv [cs.CL]*, July 2023.

[15] Chaoyi Wu, Xiaoman Zhang, Ya Zhang, Yanfeng Wang, and Weidi Xie. Towards generalist foundation model for radiology by leveraging web-scale 2D&3D medical data. *arXiv [cs.CV]*, August 2023.

[16] Ming Y Lu, Bowen Chen, Drew F K Williamson, Richard J Chen, Kenji Ikamura, Georg Gerber, Ivy Liang, Long Phi Le, Tong Ding, Anil V Parwani, and Faisal Mahmood. A foundational multimodal vision language AI assistant for human pathology. *arXiv [cs.CV]*, December 2023.

[17] Zhi Huang, Federico Bianchi, Mert Yuksekgonul, Thomas J Montine, and James Zou. A visual-language foundation model for pathology image analysis using medical twitter. *Nat. Med.*, 29(9):2307–2316, August 2023.

[18] Ting Chen, Saurabh Saxena, Lala Li, Tsung-Yi Lin, David J Fleet, and Geoffrey Hinton. A unified sequence interface for vision tasks. *arXiv [cs.CV]*, pages 31333–31346, June 2022.

[19] Wenhui Wang, Zhe Chen, Xiaokang Chen, Jiannan Wu, Xizhou Zhu, Gang Zeng, Ping Luo, Tong Lu, Jie Zhou, Yu Qiao, and Jifeng Dai. VisionLLM: Large language model is also an open-ended decoder for vision-centric tasks. *arXiv [cs.CV]*, May 2023.

[20] Haotian Zhang, Pengchuan Zhang, Xiaowei Hu, Yen-Chun Chen, Liunian Harold Li, Xiyang Dai, Lijuan Wang, Lu Yuan, Jenq-Neng Hwang, and Jianfeng Gao. GLIPv2: Unifying localization and vision-language understanding. *arXiv [cs.CV]*, pages 36067–36080, June 2022.

[21] Stephanie L Hyland, Shruthi Bannur, Kenza Bouzid, Daniel C Castro, Mercy Ranjit, Anton Schwaighofer, Fernando Pérez-García, Valentina Salvatelli, Shaury Srivastav, Anja Thieme, Noel Codella, Matthew P Lungren, Maria Teodora Wetscherek, Ozan Oktay, and Javier Alvarez-Valle. MAIRA-1: A specialised large multimodal model for radiology report generation. *arXiv [cs.CL]*, November 2023.

[22] G Jocher, K Nishimura, T Mineeva, and R Vilariño. yolov5. *Code repository*, 2020.

[23] Kishore Papineni, Salim Roukos, Todd Ward, and Wei-Jing Zhu. Bleu: a method for automatic evaluation of machine translation. In Pierre Isabelle, Eugene Charniak, and Dekang Lin, editors, *Proceedings of the 40th Annual Meeting of the Association for Computational Linguistics*, pages 311–318, Philadelphia, Pennsylvania, USA, July 2002. Association for Computational Linguistics.

[24] Tianyi Zhang, Varsha Kishore, Felix Wu, Kilian Q Weinberger, and Yoav Artzi. BERTScore: Evaluating text generation with BERT. *arXiv [cs.CL]*, April 2019.

[25] Akshay Smit, Saahil Jain, Pranav Rajpurkar, Anuj Pareek, Andrew Y Ng, and Matthew P Lungren. CheXbert: Combining automatic labelers and expert annotations for accurate radiology report labeling using BERT. *arXiv [cs.CL]*, April 2020.

[26] Saahil Jain, Ashwin Agrawal, Adriel Saporta, Steven Q H Truong, Du Nguyen Duong, Tan Bui, Pierre Chambon, Yuhao Zhang, Matthew P Lungren, Andrew Y Ng, Curtis P Langlotz, and Pranav Rajpurkar. RadGraph: Extracting clinical entities and relations from radiology reports. *arXiv [cs.CL]*, June 2021.

[27] Feiyang Yu, Mark Endo, Rayan Krishnan, Ian Pan, Andy Tsai, Eduardo Pontes Reis, Eduardo Kaiser Ururahy Nunes Fonseca, Henrique Min Ho Lee, Zahra Shakeri Hossein Abad, Andrew Y Ng, Curtis P Langlotz, Vasantha Kumar Venugopal, and Pranav Rajpurkar. Evaluating progress in automatic chest X-ray radiology report generation. *Patterns (N Y)*, 4(9):100802, September 2023.

[28] Hoang T N Nguyen, Dong Nie, Taivanbat Badamdorj, Yujie Liu, Yingying Zhu, Jason Truong, and Li Cheng. Automated generation of accurate & fluent medical X-ray reports. *arXiv [cs.CL]*, August 2021.

[29] Kai Zhang, Rong Zhou, Eashan Adhikarla, Zhiling Yan, Yixin Liu, Jun Yu, Zhengliang Liu, Xun Chen, Brian D Davison, Hui Ren, Jing Huang, Chen Chen, Yuyin Zhou, Sunyang Fu, Wei Liu, Tianming Liu, Xiang Li, Yong Chen, Lifang He, James Zou, Quanzheng Li, Hongfang Liu, and Lichao Sun. A generalist vision-language foundation model for diverse biomedical tasks. *Nat. Med.*, pages 1–13, August 2024.

[30] Dina Demner-Fushman, Marc D Kohli, Marc B Rosenman, Sonya E Shooshan, Laritza Rodriguez, Sameer Antani, George R Thoma, and Clement J McDonald. Preparing a collection of radiology examinations for distribution and retrieval. *J. Am. Med. Inform. Assoc.*, 23(2):304–310, March 2016.

[31] Alyssa Huang, Oishi Banerjee, Kay Wu, Eduardo Pontes Reis, and Pranav Rajpurkar. FineRadScore: A radiology report line-by-line evaluation technique generating corrections with severity scores. *arXiv [cs.CL]*, May 2024.

[32] Weike Zhao, Chaoyi Wu, Xiaoman Zhang, Ya Zhang, Yanfeng Wang, and Weidi Xie. RaTEScore: A metric for radiology report generation. *arXiv [cs.CL]*, June 2024.

[33] Zhuoning Yuan, Yan Yan, Milan Sonka, and Tianbao Yang. Large-scale robust deep AUC maximization: A new surrogate loss and empirical studies on medical image classification. In *2021 IEEE/CVF International Conference on Computer Vision (ICCV)*, pages 3040–3049. IEEE, October 2021.

[34] Omid Nejati Manzari, Hamid Ahmadabadi, Hossein Kashiani, Shahriar B Shokouhi, and Ahmad Ayatollahi. MedViT: A robust vision transformer for generalized medical image classification. *arXiv [cs.CV]*, February 2023.

[35] Xiaohan Xing, Yuenan Hou, Hang Li, Yixuan Yuan, Hongsheng Li, and Max Q-H Meng. Categorical relation-preserving contrastive knowledge distillation for medical image classification. In *Medical Image Computing and Computer Assisted Intervention – MICCAI 2021*, pages 163–173. Springer International Publishing, 2021.

[36] Fabian Isensee, Paul F Jaeger, Simon A A Kohl, Jens Petersen, and Klaus H Maier-Hein. nnUNet: a self-configuring method for deep learning-based biomedical image segmentation. *Nat. Methods*, 18(2):203–211, February 2021.

[37] Yunxiang Li, Bowen Jing, Zihan Li, Jing Wang, and You Zhang. nnSAM: Plug-and-play segment anything model improves nnUNet performance. *arXiv [cs.CV]*, September 2023.

[38] Alexander Kirillov, Eric Mintun, Nikhila Ravi, Hanzi Mao, Chloe Rolland, Laura Gustafson, Tete Xiao, Spencer Whitehead, Alexander C Berg, Wan-Yen Lo, Piotr Dollár, and Ross Girshick. Segment anything. *arXiv [cs.CV]*, April 2023.

[39] Tom van Sonsbeek, Mohammad Mahdi Derakhshani, Ivona Najdenkoska, Cees G M Snoek, and Marcel Worring. Open-ended medical visual question answering through prefix tuning of language models. *arXiv [cs.CV]*, March 2023.

[40] Shanshan Han, Qifan Zhang, Yuhang Yao, Weizhao Jin, Zhaozhuo Xu, and Chaoyang He. LLM multi-agent systems: Challenges and open problems. *arXiv [cs.MA]*, February 2024.

[41] Qingyun Wu, Gagan Bansal, Jieyu Zhang, Yiran Wu, Beibin Li, Erkang Zhu, Li Jiang, Xiaoyun Zhang, Shaokun Zhang, Jiale Liu, Ahmed Hassan Awadallah, Ryen W White, Doug Burger, and Chi Wang. AutoGen: Enabling next-gen LLM applications via multi-agent conversation. *arXiv [cs.AI]*, August 2023.

[42] Yilun Du, Shuang Li, Antonio Torralba, Joshua B Tenenbaum, and Igor Mordatch. Improving factuality and reasoning in language models through multiagent debate. *arXiv [cs.CL]*, May 2023.

[43] Tian Liang, Zhiwei He, Wenxiang Jiao, Xing Wang, Rui Wang, Yujiu Yang, Zhaopeng Tu, and Shuming Shi. Encouraging divergent thinking in large language models through multi-agent debate. *arXiv [cs.CL]*, May 2023.

[44] Zijun Liu, Yanzhe Zhang, Peng Li, Yang Liu, and Diyi Yang. Dynamic LLM-agent network: An LLM-agent collaboration framework with agent team optimization. *arXiv [cs.CL]*, October 2023.

[45] Chaojie Wang, Yanchen Deng, Zhiyi Lyu, Liang Zeng, Jujie He, Shuicheng Yan, and Bo An. Q\*: Improving multi-step reasoning for LLMs with deliberative planning. *arXiv [cs.AI]*, June 2024.

[46] Guanzhi Wang, Yuqi Xie, Yunfan Jiang, Ajay Mandlekar, Chaowei Xiao, Yuke Zhu, Linxi Fan, and Anima Anandkumar. Voyager: An open-ended embodied agent with large language models. *arXiv [cs.AI]*, May 2023.

[47] Junlong Cheng, Jin Ye, Zhongying Deng, Jianpin Chen, Tianbin Li, Haoyu Wang, Yanzhou Su, Ziyan Huang, Jilong Chen, Lei Jiang, Hui Sun, Junjun He, Shaoting Zhang, Min Zhu, and Yu Qiao. SAM-Med2D. *arXiv [cs.CV]*, August 2023.

[48] Alistair Johnson, Matt Lungren, Yifan Peng, Zhiyong Lu, Roger Mark, Seth Berkowitz, and Steven Horng. MIMIC-CXR-JPG - chest radiographs with structured labels, November 2019.

[49] Mark Endo, Rayan Krishnan, Viswesh Krishna, Andrew Y Ng, and Pranav Rajpurkar. Retrieval-based chest X-ray report generation using a pre-trained contrastive language-image model. In Subhrajit Roy, Stephen Pfohl, Emma Rocheteau, Girmaw Abebe Tadesse, Luis Oala, Fabian Falck, Yuyin Zhou, Liyue Shen, Ghada Zamzmi, Purity Mugambi, Ayah Zirikly, Matthew B A McDermott, and Emily Alsentzer, editors, *Proceedings of Machine Learning for Health*, volume 158 of *Proceedings of Machine Learning Research*, pages 209–219. PMLR, December 2021.

[50] Joy T Wu, Nkechinyere N Agu, Ismini Lourentzou, Arjun Sharma, Joseph A Paguio, Jasper S Yao, Edward C Dee, William Mitchell, Satyananda Kashyap, Andrea Giovannini, Leo A Celi, and Mehdi Moradi. Chest ImaGenome dataset for clinical reasoning. *arXiv [cs.CV]*, July 2021.

[51] Xinyue Hu, Lin Gu, Qiyuan An, Mengliang Zhang, Liangchen Liu, Kazuma Kobayashi, Tatsuya Harada, Ronald M Summers, and Yingying Zhu. Expert knowledge-aware image difference graph representation learning for difference-aware medical visual question answering. In *Proceedings of the 29th ACM SIGKDD Conference on Knowledge Discovery and Data Mining*, KDD '23, pages 4156–4165, New York, NY, USA, August 2023. Association for Computing Machinery.

[52] Xiaoman Zhang, Chaoyi Wu, Ziheng Zhao, Weixiong Lin, Ya Zhang, Yanfeng Wang, and Weidi Xie. PMC-VQA: Visual instruction tuning for medical visual question answering. *arXiv [cs.CV]*, May 2023.

[53] Xuehai He, Yichen Zhang, Luntian Mou, Eric Xing, and Pengtao Xie. PathVQA: 30000+ questions for medical visual question answering. *arXiv [cs.CL]*, March 2020.

[54] Jason J Lau, Soumya Gayen, Asma Ben Abacha, and Dina Demner-Fushman. A dataset of clinically generated visual questions and answers about radiology images. *Sci. Data*, 5(1):180251, November 2018.

[55] Philipp Tschandl, Cliff Rosendahl, and Harald Kittler. The HAM10000 dataset, a large collection of multi-source dermatoscopic images of common pigmented skin lesions. *Sci Data*, 5:180161, August 2018.

[56] Noel Codella, Veronica Rotemberg, Philipp Tschandl, M Emre Celebi, Stephen Dusza, David Gutman, Brian Helba, Aadi Kalloo, Konstantinos Liopyris, Michael Marchetti, Harald Kittler, and Allan Halpern. Skin lesion analysis toward melanoma detection 2018: A challenge hosted by the international skin imaging collaboration (ISIC). *arXiv [cs.CV]*, February 2019.

[57] Talha Mahboob Alam, Kamran Shaukat, Waseem Ahmad Khan, Ibrahim A Hameed, Latifah Abd Almuqren, Muhammad Ahsan Raza, Memoona Aslam, and Suhuai Luo. An efficient deep learning-based skin cancer classifier for an imbalanced dataset. *Diagnostics (Basel)*, 12(9), August 2022.

[58] Benedikt Boecking, Naoto Usuyama, Shruthi Bannur, Daniel Coelho de Castro, Anton Schwaighofer, Stephanie Hyland, Maria Teodora Wetscherek, Tristan Naumann, Aditya Nori, Javier Alvarez Valle, Hoifung Poon, and Ozan Oktay. MS-CXR: Making the most of text semantics to improve biomedical vision-language processing, May 2022.

[59] Deyao Zhu, Jun Chen, Xiaoqian Shen, Xiang Li, and Mohamed Elhoseiny. MiniGPT-4: Enhancing vision-language understanding with advanced large language models. *arXiv [cs.CV]*, April 2023.

[60] Jun Chen, Deyao Zhu, Xiaoqian Shen, Xiang Li, Zechun Liu, Pengchuan Zhang, Raghuraman Krishnamoorthi, Vikas Chandra, Yunyang Xiong, and Mohamed Elhoseiny. MiniGPT-v2: large language model as a unified interface for vision-language multi-task learning. *arXiv [cs.CV]*, October 2023.

[61] Chunyuan Li, Cliff Wong, Sheng Zhang, Naoto Usuyama, Haotian Liu, Jianwei Yang, Tristan Naumann, Hoifung Poon, and Jianfeng Gao. LLaVA-med: Training a large language-and-vision assistant for biomedicine in one day. *arXiv [cs.CV]*, June 2023.

[62] Ashish Vaswani, Noam Shazeer, Niki Parmar, Jakob Uszkoreit, Llion Jones, Aidan N Gomez, Łukasz Kaiser, and Illia Polosukhin. Attention is all you need. *Adv. Neural Inf. Process. Syst.*, 30, 2017.

[63] 'Ozg'un Çiçek, Ahmed Abdulkadir, Soeren S Lienkamp, Thomas Brox, and Olaf Ronneberger. 3D U-net: Learning dense volumetric segmentation from sparse annotation. In *Medical Image Computing and Computer-Assisted Intervention – MICCAI 2016*, pages 424–432. Springer International Publishing, 2016.

[64] Kaiming He, Xiangyu Zhang, Shaoqing Ren, and Jian Sun. Spatial pyramid pooling in deep convolutional networks for visual recognition. *IEEE Trans. Pattern Anal. Mach. Intell.*, 37(9):1904–1916, September 2015.

[65] Jimmy Lei Ba, Jamie Ryan Kiros, and Geoffrey E Hinton. Layer normalization. *arXiv [stat.ML]*, July 2016.

[66] Hugo Touvron, Louis Martin, Kevin Stone, Peter Albert, Amjad Almahairi, Yasmine Babaei, Nikolay Bashlykov, Soumya Batra, Prajjwal Bhargava, Shruti Bhosale, Dan Bikell, Lukas Blecher, Cristian Canton Ferrer, Moya Chen, Guillem Cucurull, David Esiobu, Jude Fernandes, Jeremy Fu, Wenyin Fu, Brian Fuller, Cynthia Gao, Vedanuj Goswami, Naman Goyal, Anthony Hartshorn, Saghar Hosseini, Rui Hou, Hakan Inan, Marcin Kardas, Viktor Kerkez, Madian Khabsa, Isabel Kloumann, Artem Korenev, Punit Singh Koura, Marie-Anne Lachaux, Thibaut Lavril, Jenya Lee, Diana Liskovich, Yinghai Lu, Yuning Mao, Xavier Martinet, Todor Mihaylov, Pushkar Mishra, Igor Molybog, Yixin Nie, Andrew Poulton, Jeremy Reizenstein, Rashi Rungta, Kalyan Saladi, Alan Schelten, Ruan Silva, Eric Michael Smith, Ranjan Subramanian, Xiaoqing Ellen Tan, Binh Tang, Ross Taylor, Adina Williams, Jian Xiang Kuan, Puxin Xu, Zheng Yan, Iliyan Zarov, Yuchen Zhang, Angela Fan, Melanie Kambadur, Sharan Narang, Aurelien Rodriguez, Robert Stojnic, Sergey Edunov, and Thomas Scialom. Llama 2: Open foundation and fine-tuned chat models. *arXiv [cs.CL]*, July 2023.

[67] Taku Kudo and John Richardson. SentencePiece: A simple and language independent subword tokenizer and detokenizer for neural text processing. *arXiv [cs.CL]*, August 2018.

[68] Kaiming He, Xiangyu Zhang, Shaoqing Ren, and Jian Sun. Deep residual learning for image recognition. *arXiv [cs.CV]*, pages 770–778, December 2015.

[69] Jia Deng, Wei Dong, Richard Socher, Li-Jia Li, Kai Li, and Li Fei-Fei. ImageNet: A large-scale hierarchical image database. In *2009 IEEE Conference on Computer Vision and Pattern Recognition*, pages 248–255. IEEE, June 2009.

[70] Andrew Jaegle, Felix Gimeno, Andy Brock, Oriol Vinyals, Andrew Zisserman, and Joao Carreira. Perceiver: General perception with iterative attention. In Marina Meila and Tong Zhang, editors, *Proceedings of the 38th International Conference on Machine Learning*, volume 139 of *Proceedings of Machine Learning Research*, pages 4651–4664. PMLR, 2021.

[71] Rohan Taori, Ishaan Gulrajani, Tianyi Zhang, Yann Dubois, Xuechen Li, Carlos Guestrin, Percy Liang, and Tatsunori B Hashimoto. Stanford alpaca: An instruction-following llama model, 2023.

[72] Jason Wei, Maarten Bosma, Vincent Y Zhao, Kelvin Guu, Adams Wei Yu, Brian Lester, Nan Du, Andrew M Dai, and Quoc V Le. Finetuned language models are zero-shot learners. *arXiv [cs.CL]*, September 2021.

[73] Hyung Won Chung, Le Hou, Shayne Longpre, Barret Zoph, Yi Tay, William Fedus, Yunxuan Li, Xuezhi Wang, Mostafa Dehghani, Siddhartha Brahma, Albert Webson, Shixiang Shane Gu, Zhuyun Dai, Mirac Suzgun, Xinyun Chen, Aakanksha Chowdhery, Alex Castro-Ros, Marie Pellat, Kevin Robinson, Dasha Valter, Sharan Narang, Gaurav Mishra, Adams Yu, Vincent Zhao, Yanping Huang, Andrew Dai, Hongkun Yu, Slav Petrov, Ed H Chi, Jeff Dean, Jacob Devlin, Adam Roberts, Denny Zhou, Quoc V Le, and Jason Wei. Scaling instruction-finetuned language models. *arXiv [cs.LG]*, October 2022.

[74] Karan Singhal, Shekoofeh Azizi, Tao Tu, S Sara Mahdavi, Jason Wei, Hyung Won Chung, Nathan Scales, Ajay Tanwani, Heather Cole-Lewis, Stephen Pfohl, Perry Payne, Martin Seneviratne, Paul Gamble, Chris Kelly, Abubakr Babiker, Nathanael Schärlí, Aakanksha Chowdhery, Philip Mansfield, Dina Demner-Fushman, Blaise Agüera Y Arcas, Dale Webster, Greg S Corrado, Yossi Matias, Katherine Chou, Juraj Gottweis, Nenad Tomasev, Yun Liu, Alvin Rajkomar, Joelle Barral, Christopher Semturs, Alan Karthikesalingam, and Vivek Natarajan. Large language models encode clinical knowledge. *Nature*, 620(7972):172–180, August 2023.

[75] Xin Lai, Zhuotao Tian, Yukang Chen, Yanwei Li, Yuhui Yuan, Shu Liu, and Jiaya Jia. LISA: Reasoning segmentation via large language model. *ArXiv*, abs/2308.00692, August 2023.

[76] Geoffrey Hinton, Sh Srivastava, and Kevin Swersky. Neural networks for machine learning lecture 6a overview of mini-batch gradient descent. <http://www.cs.toronto.edu/~hinton/coursera/lecture6/lec6.pdf>, 2012. Accessed: 2024-1-22.

[77] Ze Liu, Yutong Lin, Yue Cao, Han Hu, Yixuan Wei, Zheng Zhang, Stephen Lin, and Baining Guo. Swin transformer: Hierarchical vision transformer using shifted windows. In *2021 IEEE/CVF International Conference on Computer Vision (ICCV)*, pages 9992–10002. IEEE, October 2021.

[78] Edward J Hu, Yelong Shen, Phillip Wallis, Zeyuan Allen-Zhu, Yuanzhi Li, Shean Wang, Lu Wang, and Weizhu Chen. LoRA: Low-rank adaptation of large language models. *arXiv [cs.CL]*, June 2021.

[79] Ilya Loshchilov and Frank Hutter. Decoupled weight decay regularization. *arXiv [cs.LG]*, November 2017.

[80] Zhihong Chen, Yan Song, Tsung-Hui Chang, and Xiang Wan. Generating radiology reports via memory-driven transformer. *arXiv [cs.CL]*, October 2020.

[81] Yasuhide Miura, Yuhao Zhang, Emily Bao Tsai, Curtis P Langlotz, and Dan Jurafsky. Improving factual completeness and consistency of image-to-text radiology report generation. *arXiv [cs.CL]*, October 2020.

[82] Gao Huang, Zhuang Liu, Laurens Van Der Maaten, and Kilian Q Weinberger. Densely connected convolutional networks. In *2017 IEEE Conference on Computer Vision and Pattern Recognition (CVPR)*, pages 2261–2269. IEEE, July 2017.

[83] Haotian Liu, Chunyuan Li, Yuheng Li, and Yong Jae Lee. Improved baselines with visual instruction tuning. *arXiv [cs.CV]*, October 2023.

[84] Danny Driess, Fei Xia, Mehdi S M Sajjadi, Corey Lynch, Aakanksha Chowdhery, Brian Ichter, Ayzaan Wahid, Jonathan Tompson, Quan Vuong, Tianhe Yu, Wenlong Huang, Yevgen Chebotar, Pierre Sermanet, Daniel Duckworth, Sergey Levine, Vincent Vanhoucke, Karol Hausman, Marc Toussaint, Klaus Greff, Andy Zeng, Igor Mordatch, and Pete Florence. PaLM-E: An embodied multimodal language model. *arXiv [cs.LG]*, March 2023.

[85] Aqsa Mohiyuddin, Asma Basharat, Usman Ghani, Veselý Peter, Sidra Abbas, Osama Bin Naeem, and Muhammad Rizwan. Breast tumor detection and classification in mammogram images using modified YOLOv5 network. *Comput. Math. Methods Med.*, 2022:1359019, January 2022.

[86] Jingjing Wan, Bolun Chen, and Yongtao Yu. Polyp detection from colorectum images by using attentive YOLOv5. *Diagnostics (Basel)*, 11(12), December 2021.

[87] Yu Luo, Yifan Zhang, Xize Sun, Hengwei Dai, and Xiaohui Chen. Intelligent solutions in chest abnormality detection based on YOLOv5 and ResNet50. *J. Healthc. Eng.*, 2021:2267635, October 2021.

[88] Jieneng Chen, Jieru Mei, Xianhang Li, Yongyi Lu, Qihang Yu, Qingyue Wei, Xiangde Luo, Yutong Xie, Ehsan Adeli, Yan Wang, Matthew Lungren, Lei Xing, Le Lu, Alan Yuille, and Yuyin Zhou. 3D TransUNet: Advancing medical image segmentation through vision transformers. *arXiv [cs.CV]*, October 2023.

[89] Jun Ma, Yixin Wang, Xingle An, Cheng Ge, Ziqi Yu, Jianan Chen, Qiongjie Zhu, Guoqiang Dong, Jian He, Zhiqiang He, Tianjia Cao, Yuntao Zhu, Ziwei Nie, and Xiaoping Yang. Toward data-efficient learning: A benchmark for COVID-19 CT lung and infection segmentation. *Medical Physics*, 48(3):1197–1210, March 2021.

[90] Nicolás Gaggion, Candelaria Mosquera, Lucas Mansilla, Julia Mariel Saidman, Martina Aineseder, Diego H Milone, and Enzo Ferrante. Chexmask: a large-scale dataset of anatomical segmentation masks for multi-center chest x-ray images. *Scientific Data*, 11(1):511, 2024.

[91] Olivier Bernard, Alain Lalande, Clement Zotti, Frederick Cervenansky, Xin Yang, Pheng-Ann Heng, Irem Cetin, Karim Lekadir, Oscar Camara, Miguel Angel Gonzalez Ballester, Gerard Sanroma, Sandy Napel, Steffen Petersen, Georgios Tziritas, Elias Grinias, Mahendra Khened, Varghese Alex Kollerathu, Ganapathy Krishnamurthi, Marc-Michel Rohe, Xavier Pennec, Maxime Sermesant, Fabian Isensee, Paul Jager, Klaus H Maier-Hein, Peter M Full, Ivo Wolf, Sandy Engelhardt, Christian F Baumgartner, Lisa M Koch, Jelmer M Wolterink, Ivana Isgum, Yeonggul Jang, Yoonmi Hong, Jay Patravali, Shubham Jain, Olivier Humbert, and Pierre-Marc Jodoin. Deep learning techniques for automatic MRI cardiac multi-structures segmentation and diagnosis: Is the problem solved? *IEEE Trans. Med. Imaging*, 37(11):2514–2525, November 2018.

[92] Yuanfeng Ji, Haotian Bai, Jie Yang, Chongjian Ge, Ye Zhu, Ruimao Zhang, Zhen Li, Lingyan Zhang, Wanling Ma, Xiang Wan, and Ping Luo. AMOS: A large-scale abdominal multi-organ benchmark for versatile medical image segmentation. *arXiv [eess.IV]*, June 2022.

[93] Zhaohan Xiong, Qing Xia, Zhiqiang Hu, Ning Huang, Cheng Bian, Yefeng Zheng, Sulaiman Vesal, Nishant Ravikumar, Andreas Maier, Xin Yang, Pheng-Ann Heng, Dong Ni, Caizi Li, Qianqian Tong, Weixin Si, Elodie Puybareau, Younes Khoudli, Thierry Géraud, Chen Chen, Wenjia Bai, Daniel Rueckert, Lingchao Xu, Xiahai Zhuang, Xinzhe Luo, Shuman Jia, Maxime Sermesant, Yashu Liu, Kuanquan Wang, Davide Borra, Alessandro Masci, Cristiana Corsi, Coen de Vente, Mitko Veta, Rashed Karim, Chandrakanth Jayachandran Preetha, Sandy Engelhardt, Menyun Qiao, Yuanyuan Wang, Qian Tao, Marta Nuñez-Garcia, Oscar Camara, Nicolo Savioli, Pablo Lamata, and Jichao Zhao. A global benchmark of algorithms for segmenting the left atrium from late gadolinium-enhanced cardiac magnetic resonance imaging. *Med. Image Anal.*, 67(101832):101832, January 2021.

[94] Minghui Zhang, Yangqian Wu, Hanxiao Zhang, Yulei Qin, Hao Zheng, Wen Tang, Corey Arnold, Chenhao Pei, Pengxin Yu, Yang Nan, Guang Yang, Simon Walsh, Dominic C Marshall, Matthieu Komorowski, Puyang Wang, Dazhou Guo, Dakai Jin, Ya'nan Wu, Shuiqing Zhao, Runsheng Chang, Boyu Zhang, Xing Lu, Abdul Qayyum, Moona Mazher, Qi Su, Yonghuang Wu, Ying'ao Liu, Yufei Zhu, Jiancheng Yang, Ashkan Pakzad, Bojidar Rangelov, Raul San Jose Estepar, Carlos Cano Espinosa, Jiayuan Sun, Guang-Zhong Yang, and Yun Gu. Multi-site, multi-domain airway tree modeling. *Med. Image Anal.*, 90(102957):102957, December 2023.

[95] Jun Ma, Yao Zhang, Song Gu, Cheng Zhu, Cheng Ge, Yichi Zhang, Xingle An, Congcong Wang, Qiyuan Wang, Xin Liu, Shucheng Cao, Qi Zhang, Shangqing Liu, Yunpeng Wang, Yuhui Li, Jian He, and Xiaoping Yang. AbdomenCT-1K: Is abdominal organ segmentation a solved problem? *IEEE Trans. Pattern Anal. Mach. Intell.*, 44(10):6695–6714, October 2022.

[96] B Landman, Z Xu, J Igelsias, M Styner, T Langerak, and others. Miccai multi-atlas labeling beyond the cranial vault–workshop and challenge. 2015.

[97] Bjoern H Menze, Andras Jakab, Stefan Bauer, Jayashree Kalpathy-Cramer, Keyvan Farahani, Justin Kirby, Yuliya Burren, Nicole Porz, Johannes Slotboom, Roland Wiest, Levente Lanczi, Elizabeth Gerstner, Marc-André Weber, Tal Arbel, Brian B Avants, Nicholas Ayache, Patricia Buendia, D Louis Collins, Nicolas Cordier, Jason J Corso, Antonio Criminisi, Tilak Das, Hervé Delingette, Çağatay Demiralp, Christopher R Durst, Michel Dojat, Senan Doyle, Joana Festa, Florence Forbes, Ezequiel Geremia, Ben Glocker, Polina Golland, Xiaotao Guo, Andac Hamamci, Khan M Iftekharuddin, Raj Jena, Nigel M John, Ender Konukoglu, Danial Lashkari, José Antoniό Mariz, Raphael Meier, Sérgio Pereira, Doina Precup, Stephen J Price, Tammy Riklin Raviv, Syed M S Reza, Michael Ryan, Duygu Sarikaya, Lawrence Schwartz, Hoo-Chang Shin, Jamie Shotton, Carlos A Silva, Nuno Sousa, Nagesh K Subbanna, Gabor Szekely, Thomas J Taylor, Owen M Thomas, Nicholas J Tustison, Gozde Unal, Flor Vasseur, Max Wintermark, Dong Hye Ye, Liang Zhao, Binsheng Zhao, Darko Zikic, Marcel Prastawa, Mauricio Reyes, and Koen Van Leemput. The multimodal brain tumor image segmentation benchmark (BRATS). *IEEE Trans. Med. Imaging*, 34(10):1993–2024, October 2015.

[98] Michael Kistler, Serena Bonaretti, Marcel Pfahrer, Roman Niklaus, and Philippe Büchler. The virtual skeleton database: an open access repository for biomedical research and collaboration. *J. Med. Internet Res.*, 15(11):e245, November 2013.

[99] Spyridon Bakas, Hamed Akbari, Aristeidis Sotiras, Michel Bilello, Martin Rozycki, Justin S Kirby, John B Freymann, Keyvan Farahani, and Christos Davatzikos. Advancing the cancer

genome atlas glioma MRI collections with expert segmentation labels and radiomic features. *Sci. Data*, 4(1):170117, September 2017.

[100] Spyridon Bakas, Mauricio Reyes, Andras Jakab, Stefan Bauer, Markus Rempfler, Alessandro Crimi, Russell Takeshi Shinohara, Christoph Berger, Sung Min Ha, Martin Rozycki, Marcel Prastawa, Esther Alberts, Jana Lipkova, John Freymann, Justin Kirby, Michel Bilello, Hassan Fathallah-Shaykh, Roland Wiest, Jan Kirschke, Benedikt Wiestler, Rivka Colen, Aikaterini Kotrotsou, Pamela Lamontagne, Daniel Marcus, Mikhail Milchenko, Arash Nazeri, Marc-Andre Weber, Abhishek Mahajan, Ujjwal Baid, Elizabeth Gerstner, Dongjin Kwon, Gagan Acharya, Manu Agarwal, Mahbubul Alam, Alberto Albiol, Antonio Albiol, Francisco J Albiol, Varghese Alex, Nigel Allinson, Pedro H A Amorim, Abhijit Amrutkar, Ganesh Anand, Simon Andermatt, Tal Arbel, Pablo Arbelaez, Aaron Avery, Muneeza Azmat, Pranjal B., W Bai, Subhashis Banerjee, Bill Barth, Thomas Batchelder, Kayhan Batmanghelich, Enzo Battistella, Andrew Beers, Mikhail Belyaev, Martin Bendszus, Eze Benson, Jose Bernal, Halandur Nagaraja Bharath, George Biros, Sotirios Bisdas, James Brown, Mariano Cabezas, Shilei Cao, Jorge M Cardoso, Eric N Carver, Adrià Casamitjana, Laura Silvana Castillo, Marcel Catà, Philippe Cattin, Albert Cerigues, Vini-cius S Chagas, Siddhartha Chandra, Yi-Ju Chang, Shiyu Chang, Ken Chang, Joseph Chazalon, Shengcong Chen, Wei Chen, Jefferson W Chen, Zhaolin Chen, Kun Cheng, Ahana Roy Choudhury, Roger Chylla, Albert Clérigues, Steven Colleman, Ramiro German Rodriguez Colmeiro, Marc Combalia, Anthony Costa, Xiaomeng Cui, Zhenzhen Dai, Lutao Dai, Laura Alexandra Daza, Eric Deutsch, Changxing Ding, Chao Dong, Shidu Dong, Wojciech Dudzik, Zach Eaton-Rosen, Gary Egan, Guilherme Escudero, Théo Estienne, Richard Everson, Jonathan Fabrizio, Yong Fan, Longwei Fang, Xue Feng, Enzo Ferrante, Lucas Fidon, Martin Fischer, Andrew P French, Naomi Fridman, Huan Fu, David Fuentes, Yaozong Gao, Evan Gates, David Gering, Amir Gholami, Willi Gierke, Ben Glocker, Mingming Gong, Sandra González-Villá, T Grosges, Yuanfang Guan, Sheng Guo, Sudeep Gupta, Woo-Sup Han, Il Song Han, Konstantin Harmuth, Huiguang He, Aura Hernández-Sabaté, Evelyn Herrmann, Naveen Himthani, Winston Hsu, Cheyu Hsu, Xiaojun Hu, Xiaobin Hu, Yan Hu, Yifan Hu, Rui Hua, Teng-Yi Huang, Weilin Huang, Sabine Van Huffel, Quan Huo, Vivek Hy, Khan M Iftekharuddin, Fabian Isensee, Mobarakol Islam, Aaron S Jackson, Sachin R Jambawalikar, Andrew Jesson, Weijian Jian, Peter Jin, V Jeya Maria Jose, Alain Jungo, B Kainz, Konstantinos Kamnitsas, Po-Yu Kao, Ayush Karnawat, Thomas Kellermeyer, Adel Kermi, Kurt Keutzer, Mohamed Tarek Khadir, Mahendra Khened, Philipp Kickingederer, Geena Kim, Nik King, Haley Knapp, Urs peter Knecht, Lisa Kohli, Deren Kong, Xiangmao Kong, Simon Koppers, Avinash Kori, Ganapathy Krishnamurthi, Egor Krivov, Piyush Kumar, Kaisar Kushibar, Dmitrii Lachinov, Tryphon Lambrou, Joon Lee, Chengan Lee, Yuehchou Lee, M Lee, Szidonia Lefkovits, Laszlo Lefkovits, James Levitt, Tengfei Li, Hongwei Li, Wenqi Li, Hongyang Li, Xiaochuan Li, Yuexiang Li, Heng Li, Zhenye Li, Xiaoyu Li, Zeju Li, Xiaogang Li, Wenqi Li, Zheng-Shen Lin, Fengming Lin, Pietro Lio, Chang Liu, Boqiang Liu, Xiang Liu, Mingyuan Liu, Ju Liu, Luyan Liu, Xavier Llado, Marc Moreno Lopez, Pablo Ribalta Lorenzo, Zhentai Lu, Lin Luo, Zhigang Luo, Jun Ma, Kai Ma, Thomas Mackie, Anant Madabushi, Issam Mahmoudi, Klaus H Maier-Hein, Pradipta Maji, C P Mammen, Andreas Mang, B S Manjunath, Michal Marcinkiewicz, S McDonagh, Stephen McKenna, Richard McKinley, Miriam Mehl, Sachin Mehta, Raghav Mehta, Raphael Meier, Christoph Meinel, Dorit Merhof, Craig Meyer, Robert Miller, Sushmita Mitra, Aliasgar Moiyadi, David Molina-Garcia, Miguel A B Monteiro, Grzegorz Mrukwa, Andriy Myronenko, Jakub Nalepa, Thuyen Ngo, Dong Nie, Holly Ning, Chen Niu, Nicholas K Nuechterlein, Eric Oermann, Arlindo Oliveira, Diego D C Oliveira, Arnau Oliver, Alexander F I Osman, Yu-Nian Ou, Sebastien Ourselin, Nikos Paragios, Moo Sung Park, Brad Paschke, J Gregory Pauloski, Kamlesh Pawar, Nick Pawlowski, Linmin Pei, Suting Peng, Silvio M Pereira, Julian Perez-Beteta, Victor M Perez-Garcia, Simon Pezold, Bao Pham,

Ashish Phophalia, Gemma Piella, G N Pillai, Marie Piraud, Maxim Pisov, Anmol Popli, Michael P Pound, Reza Pourreza, Prateek Prasanna, Vesna Prkovska, Tony P Pridmore, Santi Puch, Élodie Puybareau, Buyue Qian, Xu Qiao, Martin Rajchl, Swapnil Rane, Michael Rebsamen, Hongliang Ren, Xuhua Ren, Karthik Revanuru, Mina Rezaei, Oliver Rippel, Luis Carlos Rivera, Charlotte Robert, Bruce Rosen, Daniel Rueckert, Mohammed Safwan, Mostafa Salem, Joaquim Salvi, Irina Sanchez, Irina Sánchez, Heitor M Santos, Emmett Sartor, Dawid Schellingerhout, Klaudius Scheufele, Matthew R Scott, Artur A Scussel, Sara Sedlar, Juan Pablo Serrano-Rubio, N Jon Shah, Nameetha Shah, Mazhar Shaikh, B Uma Shankar, Zeina Shboul, Haipeng Shen, Dinggang Shen, Linlin Shen, Haocheng Shen, Varun Shenoy, Feng Shi, Hyung Eun Shin, Hai Shu, Diana Sima, M Sinclair, Orjan Smedby, James M Snyder, Mohammadreza Soltaninejad, Guidong Song, Mehul Soni, Jean Stawiaski, Shashank Subramanian, Li Sun, Roger Sun, Jiawei Sun, Kay Sun, Yu Sun, Guoxia Sun, Shuang Sun, Yannick R Suter, Laszlo Szilagyi, Sanjay Talbar, Dacheng Tao, Dacheng Tao, Zhongzhao Teng, Siddhesh Thakur, Meenakshi H Thakur, Sameer Tharakan, Pallavi Tiwari, Guillaume Tochon, Tuan Tran, Yuhsiang M Tsai, Kuan-Lun Tseng, Tran Anh Tuan, Vadim Turlapov, Nicholas Tustison, Maria Vakalopoulou, Sergi Valverde, Rami Vanguri, Evgeny Vasiliev, Jonathan Ventura, Luis Vera, Tom Vercauteren, C A Verrastro, Lasitha Vidyaratne, Veronica Vilaplana, Ajeet Vivekanandan, Guotai Wang, Qian Wang, Chiatsue J Wang, Weichung Wang, Duo Wang, Ruixuan Wang, Yuanyuan Wang, Chunliang Wang, Guotai Wang, Ning Wen, Xin Wen, Leon Weninger, Wolfgang Wick, Shaocheng Wu, Qiang Wu, Yihong Wu, Yong Xia, Yanwu Xu, Xiaowen Xu, Peiyuan Xu, Tsai-Ling Yang, Xiaoping Yang, Hao-Yu Yang, Junlin Yang, Haojin Yang, Guang Yang, Hongdou Yao, Xujiong Ye, Changchang Yin, Brett Young-Moxon, Jinhua Yu, Xiangyu Yue, Songtao Zhang, Angela Zhang, Kun Zhang, Xuejie Zhang, Lichi Zhang, Xiaoyue Zhang, Yazhuo Zhang, Lei Zhang, Jianguo Zhang, Xiang Zhang, Tianhao Zhang, Sicheng Zhao, Yu Zhao, Xiaomei Zhao, Liang Zhao, Yefeng Zheng, Liming Zhong, Chenhong Zhou, Xiaobing Zhou, Fan Zhou, Hongtu Zhu, Jin Zhu, Ying Zhuge, Weiwei Zong, Jayashree Kalpathy-Cramer, Keyvan Farahani, Christos Davatzikos, Koen van Leemput, and Bjoern Menze. Identifying the best machine learning algorithms for brain tumor segmentation, progression assessment, and overall survival prediction in the BRATS challenge. *arXiv [cs.CV]*, November 2018.

- [101] Msoud Nickparvar. Brain tumor MRI dataset. <https://www.kaggle.com/dsv/2645886>, 2021.
- [102] Ilya Nelkenbaum, Galia Tsarfaty, Nahum Kiryati, Eli Konen, and Arnaldo Mayer. Automatic segmentation of white matter tracts using multiple brain MRI sequences. In *2020 IEEE 17th International Symposium on Biomedical Imaging (ISBI)*, pages 368–371. IEEE, April 2020.
- [103] Itzik Avital, Ilya Nelkenbaum, Galia Tsarfaty, Eli Konen, Nahum Kiryati, and Arnaldo Mayer. Neural segmentation of seeding ROIs (sROIs) for pre-surgical brain tractography. *IEEE Trans. Med. Imaging*, 39(5):1655–1667, May 2020.
- [104] Germán González, Daniel Jimenez-Carretero, Sara Rodríguez-López, Carlos Cano-Espinosa, Miguel Cazorla, Tanya Agarwal, Vinit Agarwal, Nima Tajbakhsh, Michael B Gotway, Jianming Liang, Mojtaba Masoudi, Noushin Eftekhari, Mahdi Saadatmand, Hamid-Reza Pourreza, Patricia Fraga-Rivas, Eduardo Fraile, Frank J Rybicki, Ara Kassarjian, Raúl San José Estépar, and Maria J Ledesma-Carbayo. Computer aided detection for pulmonary embolism challenge (CAD-PE). *arXiv [eess.IV]*, March 2020.
- [105] A Emre Kavur, N Sinem Gezer, Mustafa Barış, Sinem Aslan, Pierre-Henri Conze, Vladimir Groza, Duc Duy Pham, Soumick Chatterjee, Philipp Ernst, Savaş Özkan, Bora Baydar, Dmitry Lachinov, Shuo Han, Josef Pauli, Fabian Isensee, Matthias Perkonigg, Rachana Sathish, Ronnie

Rajan, Debdoot Sheet, Gurbandurdy Dovletov, Oliver Speck, Andreas Nürnberger, Klaus H Maier-Hein, Gözde Bozdağı Akar, Gözde Ünal, Oğuz Dicle, and M Alper Selver. CHAOS challenge - combined (CT-MR) healthy abdominal organ segmentation. *Med. Image Anal.*, 69 (101950):101950, April 2021.

[106] Shuo Wang, Chen Qin, Chengyan Wang, Kang Wang, Haoran Wang, Chen Chen, Cheng Ouyang, Xutong Kuang, Chengliang Dai, Yuanhan Mo, Zhang Shi, Chenchen Dai, Xinrong Chen, He Wang, and Wenjia Bai. The extreme cardiac MRI analysis challenge under respiratory motion (CMRxMotion). *arXiv [eess.IV]*, October 2022.

[107] Michela Antonelli, Annika Reinke, Spyridon Bakas, Keyvan Farahani, Annette Kopp-Schneider, Bennett A Landman, Geert Litjens, Bjoern Menze, Olaf Ronneberger, Ronald M Summers, Bram van Ginneken, Michel Bilello, Patrick Bilic, Patrick F Christ, Richard K G Do, Marc J Gollub, Stephan H Heckers, Henkjan Huisman, William R Jarnagin, Maureen K McHugo, Sandy Napel, Jennifer S Golia Pernicka, Kawal Rhode, Catalina Tobon-Gomez, Eugene Vorontsov, James A Meakin, Sebastien Ourselin, Manuel Wiesenfarth, Pablo Arbeláez, Byeonguk Bae, Sihong Chen, Laura Daza, Jianjiang Feng, Baochun He, Fabian Isensee, Yuanfeng Ji, Fucang Jia, Ildoo Kim, Klaus Maier-Hein, Dorit Merhof, Akshay Pai, Beomhee Park, Mathias Perslev, Ramin Rezaifar, Oliver Rippel, Ignacio Sarasua, Wei Shen, Jaemin Son, Christian Wachinger, Liansheng Wang, Yan Wang, Yingda Xia, Daguang Xu, Zhanwei Xu, Yefeng Zheng, Amber L Simpson, Lena Maier-Hein, and M Jorge Cardoso. The medical segmentation decathlon. *Nat. Commun.*, 13 (1):4128, July 2022.

[108] Holger R Roth, Ziyue Xu, Carlos Tor-Díez, Ramon Sanchez Jacob, Jonathan Zember, Jose Molto, Wenqi Li, Sheng Xu, Baris Turkbey, Evrim Turkbey, Dong Yang, Ahmed Harouni, Nicola Rieke, Shishuai Hu, Fabian Isensee, Claire Tang, Qinji Yu, Jan Söltter, Tong Zheng, Vitali Liauchuk, Ziqi Zhou, Jan Hendrik Moltz, Bruno Oliveira, Yong Xia, Klaus H Maier-Hein, Qikai Li, Andreas Husch, Luyang Zhang, Vassili Kovalev, Li Kang, Alessa Hering, João L Vilaça, Mona Flores, Daguang Xu, Bradford Wood, and Marius George Linguraru. Rapid artificial intelligence solutions in a pandemic-the COVID-19-20 lung CT lesion segmentation challenge. *Med. Image Anal.*, 82(102605):102605, November 2022.

[109] Pengbo Liu, Hu Han, Yuanqi Du, Heqin Zhu, Yinhao Li, Feng Gu, Honghu Xiao, Jun Li, Chunpeng Zhao, Li Xiao, Xinbao Wu, and S Kevin Zhou. Deep learning to segment pelvic bones: Large-scale CT datasets and baseline models. *arXiv [cs.CV]*, December 2020.

[110] Yang Deng, Ce Wang, Yuan Hui, Qian Li, Jun Li, Shiwei Luo, Mengke Sun, Quan Quan, Shuxin Yang, You Hao, Pengbo Liu, Honghu Xiao, Chunpeng Zhao, Xinbao Wu, and S Kevin Zhou. CTSpine1K: A large-scale dataset for spinal vertebrae segmentation in computed tomography. *arXiv [eess.IV]*, May 2021.

[111] Blaine Rister, Darvin Yi, Kaushik Shivakumar, Tomomi Nobashi, and Daniel L Rubin. CT-ORG, a new dataset for multiple organ segmentation in computed tomography. *Sci. Data*, 7(1):381, November 2020.

[112] Reuben Dorent, Aaron Kujawa, Marina Ivory, Spyridon Bakas, Nicola Rieke, Samuel Joutard, Ben Glocker, Jorge Cardoso, Marc Modat, Kayhan Batmanghelich, Arseniy Belkov, Maria Baldeon Calisto, Jae Won Choi, Benoit M Dawant, Hexin Dong, Sergio Escalera, Yubo Fan, Lasse Hansen, Mattias P Heinrich, Smriti Joshi, Victoriya Kashtanova, Hyeon Gyu Kim, Satoshi Kondo, Christian N Kruse, Susana K Lai-Yuen, Hao Li, Han Liu, Buntheng Ly, Ipek Oguz, Hyungseob Shin, Boris Shirokikh, Zixian Su, Guotai Wang, Jianghao Wu, Yanwu Xu,

Kai Yao, Li Zhang, Sebastien Ourselin, Jonathan Shapey, and Tom Vercauteren. CrossMoDA 2021 challenge: Benchmark of cross-modality domain adaptation techniques for vestibular schwannoma and cochlea segmentation. *arXiv [eess.IV]*, January 2022.

[113] Nadya Shusharina, Thomas Bortfeld, Carlos Cardenas, Brian De, Kevin Diao, Soleil Hernandez, Yufei Liu, Sean Maroongroge, Jonas Söderberg, and Moaaz Soliman. Cross-modality brain structures image segmentation for the radiotherapy target definition and plan optimization. In *Segmentation, Classification, and Registration of Multi-modality Medical Imaging Data*, Lecture notes in computer science, pages 3–15. Springer International Publishing, Cham, 2021.

[114] Alain Lalande, Zhihao Chen, Thibaut Pommier, Thomas Decourselle, Abdul Qayyum, Michel Salomon, Dominique Ginhac, Youssef Skandarani, Arnaud Boucher, Khawla Brahim, Marleen de Bruijne, Robin Camarasa, Teresa M Correia, Xue Feng, Kibrom B Girum, Anja Hennemuth, Markus Huellebrand, Raabid Hussain, Matthias Ivantsits, Jun Ma, Craig Meyer, Rishabh Sharma, Jixi Shi, Nikolaos V Tsekos, Marta Varela, Xiyue Wang, Sen Yang, Hannu Zhang, Yichi Zhang, Yuncheng Zhou, Xiahai Zhuang, Raphael Couturier, and Fabrice Meriaudeau. Deep learning methods for automatic evaluation of delayed enhancement-MRI. the results of the EMIDEC challenge. *Med. Image Anal.*, 79(102428):102428, July 2022.

[115] Jun Ma, Yao Zhang, Song Gu, Xingle An, Zhihe Wang, Cheng Ge, Congcong Wang, Fan Zhang, Yu Wang, Yinan Xu, Shuiping Gou, Franz Thaler, Christian Payer, Darko Štern, Edward G A Henderson, Dónal M McSweeney, Andrew Green, Price Jackson, Lachlan McIntosh, Quoc-Cuong Nguyen, Abdul Qayyum, Pierre-Henri Conze, Ziyan Huang, Ziqi Zhou, Deng-Ping Fan, Huan Xiong, Guoqiang Dong, Qiongjie Zhu, Jian He, and Xiaoping Yang. Fast and low-GPU-memory abdomen CT organ segmentation: The FLARE challenge. *Med. Image Anal.*, 82(102616):102616, November 2022.

[116] Jun Ma, Yao Zhang, Song Gu, Cheng Ge, Shihao Ma, Adamo Young, Cheng Zhu, Kangkang Meng, Xin Yang, Ziyan Huang, Fan Zhang, Wentao Liu, Yuanke Pan, Shoujin Huang, Jiacheng Wang, Mingze Sun, Weixin Xu, Dengqiang Jia, Jae Won Choi, Natália Alves, Bram de Wilde, Gregor Koehler, Yajun Wu, Manuel Wiesenfarth, Qiongjie Zhu, Guoqiang Dong, Jian He, the FLARE Challenge Consortium, and Bo Wang. Unleashing the strengths of unlabeled data in pan-cancer abdominal organ quantification: The FLARE22 challenge. *arXiv [eess.IV]*, August 2023.

[117] Catalina Tobon-Gomez, Arjan Geers, Jochen Peters, Juergen Weese, Karen Pinto, Rashed Karim, Tobias Schaeffter, Reza Razavi, and Kawaal Rhode. Benchmark for algorithms segmenting the left atrium from 3D CT and MRI datasets. *IEEE Trans. Med. Imaging*, 34(7):1460–1473, February 2015.

[118] Stefan Winzeck, Arsany Hakim, Richard McKinley, José A A D S R Pinto, Victor Alves, Carlos Silva, Maxim Pisov, Egor Krivov, Mikhail Belyaev, Miguel Monteiro, Arlindo Oliveira, Youngwon Choi, Myunghee Cho Paik, Yongchan Kwon, Hanbyul Lee, Beom Joon Kim, Joong-Ho Won, Mobarakol Islam, Hongliang Ren, David Robben, Paul Suetens, Enhao Gong, Yilin Niu, Junshen Xu, John M Pauly, Christian Lucas, Mattias P Heinrich, Luis C Rivera, Laura S Castillo, Laura A Daza, Andrew L Beers, Pablo Arbelaezs, Oskar Maier, Ken Chang, James M Brown, Jayashree Kalpathy-Cramer, Greg Zaharchuk, Roland Wiest, and Mauricio Reyes. ISLES 2016 and 2017-benchmarking ischemic stroke lesion outcome prediction based on multispectral MRI. *Front. Neurol.*, 9:679, September 2018.

[119] Arsany Hakim, Søren Christensen, Stefan Winzeck, Maarten G Lansberg, Mark W Parsons, Christian Lucas, David Robben, Roland Wiest, Mauricio Reyes, and Greg Zaharchuk. Predicting

infarct core from computed tomography perfusion in acute ischemia with machine learning: Lessons from the ISLES challenge. *Stroke*, 52(7):2328–2337, July 2021.

[120] Carlo W Cereda, Søren Christensen, Bruce C V Campbell, Nishant K Mishra, Michael Mlynash, Christopher Levi, Matus Straka, Max Wintermark, Roland Bammer, Gregory W Albers, Mark W Parsons, and Maarten G Lansberg. A benchmarking tool to evaluate computer tomography perfusion infarct core predictions against a DWI standard. *J. Cereb. Blood Flow Metab.*, 36(10):1780–1789, October 2016.

[121] Moritz R Hernandez Petzsche, Ezequiel de la Rosa, Uta Hanning, Roland Wiest, Waldo Valenzuela, Mauricio Reyes, Maria Meyer, Sook-Lei Liew, Florian Kofler, Ivan Ezhov, David Robben, Alexandre Hutton, Tassilo Friedrich, Teresa Zarth, Johannes Bürkle, The Anh Baran, Björn Menze, Gabriel Broocks, Lukas Meyer, Claus Zimmer, Tobias Boeckh-Behrens, Maria Berndt, Benno Ikenberg, Benedikt Wiestler, and Jan S Kirschke. ISLES 2022: A multi-center magnetic resonance imaging stroke lesion segmentation dataset. *Sci. Data*, 9(1):762, December 2022.

[122] Oskar Maier, Bjoern H Menze, Janina von der Gablentz, Levin 'Hani, Matthias P Heinrich, Matthias Liebrand, Stefan Winzeck, Abdul Basit, Paul Bentley, Liang Chen, Daan Christiaens, Francis Dutil, Karl Egger, Chaolu Feng, Ben Glocker, Michael G'otz, Tom Haeck, Hanna-Leena Halme, Mohammad Havaei, Khan M Iftekharuddin, Pierre-Marc Jodoin, Konstantinos Kamnitsas, Elias Kellner, Antti Korvenoja, Hugo Larochelle, Christian Ledig, Jia-Hong Lee, Frederik Maes, Qaiser Mahmood, Klaus H Maier-Hein, Richard McKinley, John Muschelli, Chris Pal, Linmin Pei, Janaki Raman Rangarajan, Syed M S Reza, David Robben, Daniel Rueckert, Eero Salli, Paul Suetens, Ching-Wei Wang, Matthias Wilms, Jan S Kirschke, Ulrike M Kr Amer, Thomas F M'unte, Peter Schramm, Roland Wiest, Heinz Handels, and Mauricio Reyes. ISLES 2015 - a public evaluation benchmark for ischemic stroke lesion segmentation from multispectral MRI. *Med. Image Anal.*, 35:250–269, January 2017.

[123] Xiangyu Li, Gongning Luo, Wei Wang, Kuanquan Wang, Yue Gao, and Shuo Li. Hematoma expansion context guided intracranial hemorrhage segmentation and uncertainty estimation. *IEEE J. Biomed. Health Inform.*, 26(3):1140–1151, March 2022.

[124] Xiangyu Li, Gongning Luo, Kuanquan Wang, Hongyu Wang, Jun Liu, Xinjie Liang, Jie Jiang, Zhenghao Song, Chunyue Zheng, Haokai Chi, Mingwang Xu, Yingte He, Xinghua Ma, Jingwen Guo, Yifan Liu, Chuanpu Li, Zeli Chen, Md Mahfuzur Rahman Siddiquee, Andriy Myronenko, Antoine P Sanner, Anirban Mukhopadhyay, Ahmed E Othman, Xingyu Zhao, Weiping Liu, Jinhuang Zhang, Xiangyuan Ma, Qinghui Liu, Bradley J MacIntosh, Wei Liang, Moona Mazher, Abdul Qayyum, Valeria Abramova, Xavier Lladó, and Shuo Li. The state-of-the-art 3D anisotropic intracranial hemorrhage segmentation on non-contrast head CT: The INSTANCE challenge. *arXiv [eess.IV]*, January 2023.

[125] Nicholas Heller, Niranjan Sathianathan, Arveen Kalapara, Edward Walczak, Keenan Moore, Heather Kaluzniak, Joel Rosenberg, Paul Blake, Zachary Rengel, Makinna Oestreich, Joshua Dean, Michael Tradewell, Aneri Shah, Resha Tejpaul, Zachary Edgerton, Matthew Peterson, Shanaeabbas Raza, Subodh Regmi, Nikolaos Papanikopoulos, and Christopher Weight. The KiTS19 challenge data: 300 kidney tumor cases with clinical context, CT semantic segmentations, and surgical outcomes. *arXiv [q-bio.QM]*, March 2019.

[126] Zhongchen Zhao, Huai Chen, and Lisheng Wang. A coarse-to-fine framework for the 2021 kidney and kidney tumor segmentation challenge. In *Lecture Notes in Computer Science*, Lecture notes in computer science, pages 53–58. Springer International Publishing, Cham, 2022.

[127] João Pedrosa, Guilherme Aresta, Carlos Ferreira, Márcio Rodrigues, Patrícia Leitão, André Silva Carvalho, João Rebelo, Eduardo Negrão, Isabel Ramos, António Cunha, and Aurélio Campilho. LNDb: A lung nodule database on computed tomography. *arXiv [eess.IV]*, November 2019.

[128] Arnaud Arindra Adiyoso Setio, Alberto Traverso, Thomas de Bel, Moira S N Berens, Cas van den Bogaard, Piergiorgio Cerello, Hao Chen, Qi Dou, Maria Evelina Fantacci, Bram Geurts, Robbert van der Gugten, Pheng Ann Heng, Bart Jansen, Michael M J de Kaste, Valentin Kotov, Jack Yu-Hung Lin, Jeroen T M C Manders, Alexander Sónora-Mengana, Juan Carlos García-Naranjo, Evgenia Papavasileiou, Mathias Prokop, Marco Saletta, Cornelia M Schaefer-Prokop, Ernst T Scholten, Luuk Scholten, Miranda M Snoeren, Ernesto Lopez Torres, Jef Vandemeulebroucke, Nicole Walasek, Guido C A Zuidhof, Bram van Ginneken, and Colin Jacobs. Validation, comparison, and combination of algorithms for automatic detection of pulmonary nodules in computed tomography images: The LUNA16 challenge. *Med. Image Anal.*, 42:1–13, December 2017.

[129] Aaron Carass, Snehashis Roy, Amod Jog, Jennifer L Cuzzocreo, Elizabeth Magrath, Adrian Gherman, Julia Button, James Nguyen, Ferran Prados, Carole H Sudre, Manuel Jorge Cardoso, Niamh Cawley, Olga Ciccarelli, Claudia A M Wheeler-Kingshott, Sébastien Ourselin, Laurence Catanese, Hrishikesh Deshpande, Pierre Maurel, Olivier Commowick, Christian Barillot, Xavier Tomas-Fernandez, Simon K Warfield, Suthirth Vaidya, Abhijith Chunduru, Ramanathan Muthuganapathy, Ganapathy Krishnamurthi, Andrew Jesson, Tal Arbel, Oskar Maier, Heinz Handels, Leonardo O Iheme, Devrim Unay, Saurabh Jain, Diana M Sima, Dirk Smeets, Mohsen Ghafoorian, Bram Platel, Ariel Birenbaum, Hayit Greenspan, Pierre-Louis Bazin, Peter A Calabresi, Ciprian M Crainiceanu, Lotta M Ellingsen, Daniel S Reich, Jerry L Prince, and Dzung L Pham. Longitudinal multiple sclerosis lesion segmentation: Resource and challenge. *Neuroimage*, 148:77–102, March 2017.

[130] Xiahai Zhuang and Juan Shen. Multi-scale patch and multi-modality atlases for whole heart segmentation of MRI. *Med. Image Anal.*, 31:77–87, July 2016.

[131] Gongning Luo, Kuanquan Wang, Jun Liu, Shuo Li, Xinjie Liang, Xiangyu Li, Shaowei Gan, Wei Wang, Suyu Dong, Wenyi Wang, Pengxin Yu, Enyou Liu, Hongrong Wei, Na Wang, Jia Guo, Huiqi Li, Zhao Zhang, Ziwei Zhao, Na Gao, Nan An, Ashkan Pakzad, Bojidar Rangelov, Jiaqi Dou, Song Tian, Zeyu Liu, Yi Wang, Ampatishan Sivalingam, Kumaradevan Punithakumar, Zhaowen Qiu, and Xin Gao. Efficient automatic segmentation for multi-level pulmonary arteries: The PARSE challenge. *arXiv [eess.IV]*, April 2023.

[132] Huihui Fang, Fei Li, Junde Wu, Huazhu Fu, Xu Sun, José Ignacio Orlando, Hrvoje Bogunović, Xiulan Zhang, and Yanwu Xu. Open fundus photograph dataset with pathologic myopia recognition and anatomical structure annotation. *Sci. Data*, 11(1):99, January 2024.

[133] Geert Litjens, Robert Toth, Wendy van de Ven, Caroline Hoeks, Sjoerd Kerkstra, Bram van Ginneken, Graham Vincent, Gwenaël Guillard, Neil Birbeck, Jindang Zhang, Robin Strand, Filip Malmberg, Yangming Ou, Christos Davatzikos, Matthias Kirschner, Florian Jung, Jing Yuan, Wu Qiu, Qinquan Gao, Philip Eddie Edwards, Bianca Maan, Ferdinand van der Heijden, Soumya Ghose, Jhimli Mitra, Jason Dowling, Dean Barratt, Henkjan Huisman, and Anant Madabhushi. Evaluation of prostate segmentation algorithms for MRI: the PROMISE12 challenge. *Med. Image Anal.*, 18(2):359–373, February 2014.

[134] A Bharatha, M Hirose, N Hata, S K Warfield, M Ferrant, K H Zou, E Suarez-Santana, J Ruiz-Alzola, A D’Amico, R A Cormack, R Kikinis, F A Jolesz, and C M Tempany. Evaluation of

three-dimensional finite element-based deformable registration of pre- and intraoperative prostate imaging. *Med. Phys.*, 28(12):2551–2560, December 2001.

[135] Quande Liu, Qi Dou, Lequan Yu, and Pheng Ann Heng. MS-net: Multi-site network for improving prostate segmentation with heterogeneous MRI data. *IEEE Trans. Med. Imaging*, 39(9):2713–2724, September 2020.

[136] Jakob Wasserthal, Hanns-Christian Breit, Manfred T Meyer, Maurice Pradella, Daniel Hinck, Alexander W Sauter, Tobias Heye, Daniel T Boll, Joshy Cyriac, Shan Yang, Michael Bach, and Martin Segeroth. TotalSegmentator: Robust segmentation of 104 anatomic structures in CT images. *Radiol. Artif. Intell.*, 5(5):e230024, September 2023.

[137] Rina D Rudyanto, Sjoerd Kerkstra, Eva M van Rikxoort, Catalin Fetita, Pierre-Yves Brillet, Christophe Lefevre, Wenzhe Xue, Xiangjun Zhu, Jianming Liang, Ilkay Öksüz, Devrim Ünay, Kamuran Kadipaşaoğlu, Raúl San José Estépar, James C Ross, George R Washko, Juan-Carlos Prieto, Marcela Hernández Hoyos, Maciej Orkisz, Hans Meine, Markus Hüllebrand, Christina Stöcker, Fernando Lopez Mir, Valery Naranjo, Eliseo Villanueva, Marius Staring, Changyan Xiao, Berend C Stoel, Anna Fabijanska, Erik Smistad, Anne C Elster, Frank Lindseth, Amir Hossein Foruzan, Ryan Kiros, Karteek Popuri, Dana Cobzas, Daniel Jimenez-Carretero, Andres Santos, Maria J Ledesma-Carbayo, Michael Helmberger, Martin Urschler, Michael Pienn, Dennis G H Bosboom, Arantza Campo, Mathias Prokop, Pim A de Jong, Carlos Ortiz-de Solorzano, Arrate Muñoz-Barrutia, and Bram van Ginneken. Comparing algorithms for automated vessel segmentation in computed tomography scans of the lung: the VESSEL12 study. *Med. Image Anal.*, 18(7):1217–1232, October 2014.

[138] Anjany Sekuboyina, Malek E Husseini, Amirhossein Bayat, Maximilian Löffler, Hans Liebl, Hongwei Li, Giles Tetteh, Jan Kukačka, Christian Payer, Darko Štern, Martin Urschler, Maodong Chen, Dalong Cheng, Nikolas Lessmann, Yujin Hu, Tianfu Wang, Dong Yang, Daguang Xu, Felix Ambellan, Tamaz Amiranashvili, Moritz Ehlke, Hans Lamecker, Sebastian Lehnert, Marilia Lirio, Nicolás Pérez de Olaguer, Heiko Ramm, Manish Sahu, Alexander Tack, Stefan Zachow, Tao Jiang, Xinjun Ma, Christoph Angerman, Xin Wang, Kevin Brown, Alexandre Kirszenberg, Élodie Puybareau, Di Chen, Yiwei Bai, Brandon H Rapazzo, Timyoas Yeah, Amber Zhang, Shangliang Xu, Feng Hou, Zhiqiang He, Chan Zeng, Zheng Xiangshang, Xu Liming, Tucker J Netherton, Raymond P Mumme, Laurence E Court, Zixun Huang, Chenhang He, Li-Wen Wang, Sai Ho Ling, Lê Duy Huýnh, Nicolas Boutry, Roman Jakubicek, Jiri Chmelik, Supriti Mulay, Mohanasankar Sivaprakasam, Johannes C Paetzold, Suprosanna Shit, Ivan Ezhov, Benedikt Wiestler, Ben Glocker, Alexander Valentinitzsch, Markus Rempfler, Björn H Menze, and Jan S Kirschke. VerSe: A vertebrae labelling and segmentation benchmark for multi-detector CT images. *Med. Image Anal.*, 73(102166):102166, October 2021.

[139] Xiangde Luo, Wenjun Liao, Jianghong Xiao, Jieneng Chen, Tao Song, Xiaofan Zhang, Kang Li, Dimitris N Metaxas, Guotai Wang, and Shaoting Zhang. WORD: A large scale dataset, benchmark and clinical applicable study for abdominal organ segmentation from CT image. *Med. Image Anal.*, 82(102642):102642, November 2022.

[140] Sergios Gatidis, Tobias Hepp, Marcel Früh, Christian La Fougère, Konstantin Nikolaou, Christina Pfannenberg, Bernhard Schölkopf, Thomas Küstner, Clemens Cyran, and Daniel Rubin. A whole-body FDG-PET/CT dataset with manually annotated tumor lesions. *Sci. Data*, 9(1):601, October 2022.

[141] Walid Al-Dhabyani, Mohammed Gomaa, Hussien Khaled, and Aly Fahmy. Dataset of breast ultrasound images. *Data Brief*, 28(104863):104863, February 2020.

[142] Murtadha D Hssayeni, Muayad S Croock, Aymen D Salman, Hassan Falah Al-khafaji, Zakaria A Yahya, and Behnaz Ghoraani. Intracranial hemorrhage segmentation using a deep convolutional model. *Data (Basel)*, 5(1):14, February 2020.

[143] Jorge Bernal, F Javier Sánchez, Gloria Fernández-Esparrach, Debora Gil, Cristina Rodríguez, and Fernando Vilariño. WM-DOVA maps for accurate polyp highlighting in colonoscopy: Validation vs. saliency maps from physicians. *Computerized Medical Imaging and Graphics*, 43: 99–111, July 2015.

[144] Jorge Bernal, Nima Tajkbaksh, Francisco Javier Sanchez, Bogdan J Matuszewski, Hao Chen, Lequan Yu, Quentin Angermann, Olivier Romain, Bjorn Rustad, Ilangko Balasingham, Konstantin Pogorelov, Sungbin Choi, Quentin Debard, Lena Maier-Hein, Stefanie Speidel, Danail Stoyanov, Patrick Brando, Henry Cordova, Cristina Sanchez-Montes, Suryakanth R Gurudu, Gloria Fernandez-Esparrach, Xavier Dray, Jianming Liang, and Aymeric Histace. Comparative validation of polyp detection methods in video colonoscopy: Results from the MICCAI 2015 endoscopic vision challenge. *IEEE Trans. Med. Imaging*, 36(6):1231–1249, June 2017.

[145] Huazhu Fu, Jun Cheng, Yanwu Xu, Damon Wing Kee Wong, Jiang Liu, and Xiaochun Cao. Joint optic disc and cup segmentation based on multi-label deep network and polar transformation. *arXiv [cs.CV]*, January 2018.

[146] Huazhu Fu, Fei Li, Xu Sun, Xingxing Cao, Jingan Liao, Jose Ignacio Orlando, Xing Tao, Yuexiang Li, Shihao Zhang, Mingkui Tan, Chenglang Yuan, Cheng Bian, Ruitao Xie, Jiongcheng Li, Xiaomeng Li, Jing Wang, Le Geng, Panming Li, Huaying Hao, Jiang Liu, Yan Kong, Yongyong Ren, Hrvoje Bogunovic, Xiulan Zhang, and Yanwu Xu. AGE challenge: Angle closure glaucoma evaluation in anterior segment optical coherence tomography. *arXiv [cs.CV]*, May 2020.

[147] Danielle F Pace, Adrian V Dalca, Tal Geva, Andrew J Powell, Mehdi H Moghari, and Polina Golland. Interactive whole-heart segmentation in congenital heart disease. *Med. Image Comput. Comput. Assist. Interv.*, 9351:80–88, October 2015.

[148] Huihui Fang, Fei Li, Huazhu Fu, Xu Sun, Xingxing Cao, Fengbin Lin, Jaemin Son, Sunho Kim, Gwenole Quellec, Sarah Matta, Sharath M Shankaranarayana, Yi-Ting Chen, Chuen-Heng Wang, Nisarg A Shah, Chia-Yen Lee, Chih-Chung Hsu, Hai Xie, Baiying Lei, Ujjwal Baid, Shubham Innani, Kang Dang, Wenxiu Shi, Ravi Kamble, Nitin Singhal, Ching-Wei Wang, Shih-Chang Lo, José Ignacio Orlando, Hrvoje Bogunović, Xiulan Zhang, Yanwu Xu, and iChallenge-AMD study group. ADAM challenge: Detecting age-related macular degeneration from fundus images. *arXiv [eess.IV]*, February 2022.

[149] Debesh Jha, Pia H Smedsrød, Michael A Riegler, Pål Halvorsen, Thomas de Lange, Dag Johansen, and Håvard D Johansen. Kvasir-SEG: A segmented polyp dataset. In *MultiMedia Modeling*, Lecture notes in computer science, pages 451–462. Springer International Publishing, Cham, 2020.

[150] Debesh Jha, Nikhil Kumar Tomar, Sharib Ali, Michael A Riegler, Håvard D Johansen, Dag Johansen, Thomas de Lange, and Pål Halvorsen. NanoNet: Real-time polyp segmentation in video capsule endoscopy and colonoscopy. *arXiv [eess.IV]*, April 2021.

[151] Victor M Campello, Polyxeni Gkontra, Cristian Izquierdo, Carlos Martin-Isla, Alireza Sojoudi, Peter M Full, Klaus Maier-Hein, Yao Zhang, Zhiqiang He, Jun Ma, Mario Parreno, Alberto Albiol, Fanwei Kong, Shawn C Shadden, Jorge Corral Acero, Vaanathi Sundaresan, Mina Saber, Mustafa Elattar, Hongwei Li, Bjoern Menze, Firas Khader, Christoph Haarburger, Cian M

Scannell, Mitko Veta, Adam Carscadden, Kumaradevan Punithakumar, Xiao Liu, Sotirios A Tsaftaris, Xiaoqiong Huang, Xin Yang, Lei Li, Xiahai Zhuang, David Vilades, Martin L Descalzo, Andrea Guala, Lucia La Mura, Matthias G Friedrich, Ria Garg, Julie Lebel, Filipe Henriques, Mahir Karakas, Ersin Cavus, Steffen E Petersen, Sergio Escalera, Santi Segui, Jose F Rodriguez-Palomares, and Karim Lekadir. Multi-centre, multi-vendor and multi-disease cardiac segmentation: The M&Ms challenge. *IEEE Trans. Med. Imaging*, 40(12):3543–3554, December 2021.

[152] Anindo Saha, Joeran S Bosma, Jasper J Twilt, Bram van Ginneken, Anders Bjartell, Anwar R Padhani, David Bonekamp, Geert Villeirs, Georg Salomon, Gianluca Giannarini, Jayashree Kalpathy-Cramer, Jelle Barentsz, Klaus H Maier-Hein, Mirabela Rusu, Olivier Rouvière, Roderick van den Bergh, Valeria Panebianco, Veeru Kasivisvanathan, Nancy A Obuchowski, Derya Yakar, Mattijs Elschot, Jeroen Veltman, Jurgen J Fütterer, Maarten de Rooij, Henkjan Huisman, and PI-CAI consortium. Artificial intelligence and radiologists in prostate cancer detection on MRI (PI-CAI): an international, paired, non-inferiority, confirmatory study. *Lancet Oncol.*, 25(7):879–887, July 2024.